Millisecond Oscillations During Thermonuclear X-ray Bursts

by

Michael Patrick Muno

B.A. Physics and Astronomy
University of California, Berkeley, 1997

Submitted to the Department of Physics
in partial fulfillment of the requirements for the degree of

Doctor of Philosophy

at the

MASSACHUSETTS INSTITUTE OF TECHNOLOGY

May 2002

Author . . . .
Department of Physics
May 10, 2002

Certified by . . . .
Deepto Chakrabarty
Assistant Professor of Physics
Thesis Supervisor

Certified by . . . .
Ronald A. Remillard
Principal Research Scientist, Center for Space Research
Thesis Co-Supervisor

Accepted by . . . .
Thomas J. Greytak
Professor of Physics
Associate Department Head for Education

Millisecond Oscillations During Thermonuclear X-ray Bursts

by

Michael Patrick Muno

Submitted to the Department of Physics
on May 10, 2002, in partial fulfillment of the
requirements for the degree of
Doctor of Philosophy

Abstract

I analyze 68 oscillation trains detected in a search of 159 thermonuclear bursts from eight neutron star X-ray binaries observed with the *Rossi X-ray Timing Explorer*. I use all data that were public as of September 2001. The frequencies of the oscillations are uniformly distributed between 270–620 Hz, and are nearly constant for a given source. They typically have fractional rms amplitudes of 5%. During a burst, the frequencies of the oscillations generally drift upward by $\sim$4 Hz to stable limiting values. Neither the amplitudes of the oscillations nor the evolution of their frequencies are simply related to the time scales and energetics of the bursts.

If the frequency drift is accounted for with smooth functions, the oscillations are coherent in 70% of the bursts, and their asymptotic frequencies are stable to a few parts in 1000. This suggests that the asymptotic frequencies are determined by the spin of the neutron star. However, residual dispersion in the frequencies from 4U 1636−536 is uncorrelated with the known orbit of the system, so some mechanism other than the orbital motion of the neutron star must cause them to vary.

Models for the oscillations suggest that they originate from patterns in the stellar surface brightness that drift in the direction opposite the rotation of the neutron star, yielding oscillation frequencies lower than that of the spin. The patterns produce oscillations that are very sinusoidal — harmonic components have amplitudes that are less than 5–10% of those of the main signals. This suggests that the patterns are very symmetric.

The types of bursts that exhibit oscillations are correlated with the pulsation frequency. In particular, oscillations between 500–650 Hz occur almost exclusively in bursts that exhibit photospheric radius expansion, while oscillations with frequencies of 250–400 Hz are slightly more likely to occur in bursts without radius expansion. This appears to be because (*i*) oscillations from all of the sources are observed only when the persistent accretion rate is relatively high ($\sim 0.1\dot{M}_{\rm Edd}$), while (*ii*) in $\sim$ 300 Hz sources radius expansion occurs at lower $\dot{M}$, yet in $\sim$ 600 Hz sources it occurs at higher $\dot{M}$.

Thesis Supervisor: Deepto Chakrabarty
Title: Assistant Professor of Physics

Thesis Co-Supervisor: Ronald A. Remillard
Title: Principal Research Scientist, Center for Space Research

Acknowledgments

I am very thankful for the friends and collaborators that I have had throughout my stay at MIT. To start, I sincerely thank Ron Remillard, who has served as my advisor and mentor. He worked tirelessly to see that the work I produced was accurate, free from my own bias as to what I wanted to see from the data, and clear of artifacts introduced by my analysis. Most of all, he encouraged me to be meticulous to a level that was not required of me in the past. I have become a much more accurate and careful scientist thanks to him. Even now, I am glad that he still encourages me to keep looking forward.

Deepto Chakrabarty has aided me greatly, through his insightful suggestions on how to approach problems, by his concern that I express myself more clearly and concisely, and of course by providing me the opportunity to work on the database of bursts that forms the basis of this thesis. Ed Morgan started me on my first projects with *RXTE*. He has had quite a knack for finding interesting projects for me to work on, and for pointing me toward the interesting things in the mass of data that I accumulated. He has also always been available and helpful in solving the daily problems that I have encountered in my research. Dimitrios Psaltis has been helpful continually in providing suggestions that have made my work clearer, to myself therefore hopefully to others. He has also encouraged me on many occasions, when I had nearly lost interest in my thesis topic. Lars Bildsten has always offered me clear and insightful explanations of astrophysics, starting when I was an undergraduate at Berkeley, without which I might have fallen into a bottomless pit of phenomenology long ago.

I am of course also grateful to the undergrads, grads, and post-docs with whom I have collaborated for these years. Don Smith, Bob Shirey, and Chris Becker all helped to get me started in my research, providing not only valuable advice, but tools and techniques that I have used continually since. Derek Fox helped and encouraged me in my study of burst oscillations, and in writing proposals for new instruments. Feryal Özel and Duncan Galloway have been great help in sorting out the meaning of many of my results, and in ensuring that they were presented clearly. I owe special thanks to Pavlin Savov, who found most of the X-ray bursts in the first place.

I am also thankful to the *RXTE* ASM/EDS group, who have supported me as a graduate student. Hale Bradt gave me the opportunity to work with this group, Al Levine provided thorough consideration and sound advice on problems of all sorts, and Doug Alan saved much of my time by solving messy computer problems (I still use purify, and recommend it for debugging code).

The astrophysics graduate students at MIT have been a great source of sympathy and amusement. I would like to thank in particular Eric Pfahl, Jon Miller, Glen Monnelly, Adrienne Juett, John Fregeau, and Mike Stage, for serious conversations and aimless diversions in various proportions.

Finally, I owe a lot to my parents and sister, who have supported me greatly from afar for many years. And of course, Thandi Drakes is the best thing I have found at MIT, and has made my life here in the last two years infinitely more pleasurable.

Contents

List of Figures

List of Tables

Chapter 1

Introduction

1.1 X-ray Binary Systems

X-ray binaries contain the compact remnant of a supernova explosion — a neutron star or black hole — that is accreting matter from a more ordinary stellar companion (see White et al., 1995, for a review). They were identified as a class through much concerted effort during the two decades that followed the advent of X-ray astronomy in the 1960's. Most of the known X-ray binaries are in the galactic plane and the Large and Small Magellenic Clouds, although luminous examples are increasingly being observed in other nearby galaxies. Optical observations have revealed that their counterparts, when they can be identified, are relatively ordinary stars of all spectral types. However, the distances derived for the sources, usually several kpc, indicate that they emit more than 10^{37} erg s^{-1} in X-rays from regions only tens of kilometers across. This energy output — one thousand times the luminosity of the sun — can only be provided by the release of potential energy as matter falls into the deep gravitational well of a compact object. Whereas the fusion of hydrogen into iron releases approximately 8 MeV per nucleon, the gravitational potential energy in a single proton falling onto a compact object is

$$\Delta E = \frac{GMm_p}{R} = 140 \frac{M}{M_\odot} \frac{R}{10^6 \mathrm{cm}} \ \mathrm{MeV}. \tag{1.1}$$

Since $R \sim 10^6$ cm is roughly the radius of a neutron star or of the event horizon of a 3 $M_\odot$ black hole, matter being accreted at a rate of only 10^{-9} $M_\odot$ yr^{-1} can power the brightest X-ray binaries. Orbital modulations in the X-ray and optical emission from many of these systems confirm that the binary companions are the source of the matter being accreted by the compact object.

A standard picture of an X-ray binary is illustrated in Figure 1-1. The orbital periods of these systems range from 11 minutes to about a year. The period is in turn determined by the nature of the mass donor, which can be anything from a > 20 $M_\odot$ O supergiant to a < 0.1 $M_\odot$white dwarf. Matter is donated by the companion star either through its stellar wind, or because the gravitational force of the compact object is as strong as that the donor at its surface. If the material has significant angular momentum about the binary center of mass, it forms a disk about the central compact object. Orbits in the disk are approximately Keplerian, but friction causes matter to transfer its angular momentum to the outer disk and fall toward the compact object. Optical, ultraviolet, and X-ray emission are generated because the disk is also heated by the friction (see Frank et al., 1995). The

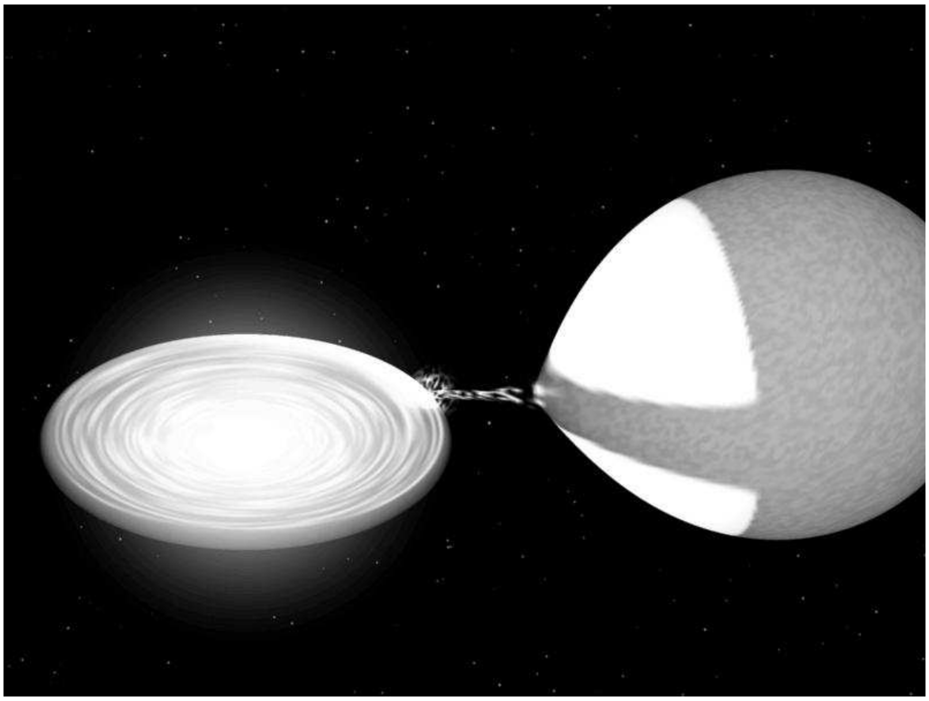

Figure 1-1 An illustration of an X-ray binary. The system illustrated contains a 0.9 $M_\odot$ star orbiting a 1.4 $M_\odot$ compact object, and would have an orbital period of 9 hours. The figure is adapted from the program *binsim* written by R. Hynes (`http://www.astro.soton.ac.uk/~rih/`).

presence of accretion disks is well-established in many systems through observations of their thermal X-ray spectra (Makishima et al., 1986), and optical and X-ray emission lines that are Doppler-broadened by orbital motion in the disk (e.g., Orosz et al., 1994; Miller et al., 2002).

The resulting X-ray emission originates from plasma with temperatures as hot as 10^7 K, which is difficult to attain in terrestrial laboratories. The amount of knowledge that can be gained from these systems is illustrated by some outstanding questions about how the X-ray emission is generated. For instance, thermal emission that often dominates the spectrum probably originates from an optically thick accretion disk. However, the source of the friction in the disk that powers the emission is not yet certain, but probably is due to magnetic turbulence (Balbus & Hawley, 1992). More perplexing are the non-thermal spectra that appear as a power law in flux as a function of energy (Grove et al., 1998). These spectra are thought to be produced by inverse-Compton scattering of photons to higher energies by a population of relativistic electrons. The origin of these electrons are uncertain, but it has alternately been proposed that they are produced by a radiative instability in the disk (Shapiro et al., 1976), by matter streaming onto the compact object on radial trajectories (Chakrabarti & Titarchuk, 1995), by magnetic flares above the disk (di Matteo et al., 1999), or by a shock at the base of an outflow from the disk (Markoff et al., 2001). Combinations of numerical simulations and observations of X-ray binaries are providing means of exploring a wide range of physics, such as the electronic transitions of highly ionized atoms, particle acceleration in shocks, the dynamics of magnetized plasma, and the behavior of matter and radiation that are tightly coupled.

The astrophysical phenomena associated with X-ray binaries have analogs in other accreting systems, such as active galactic nuclei, young stellar objects, and accreting white dwarfs. First, X-ray binaries exhibit dramatic changes in the X-ray spectrum from their inner accretion disks, which are thought to be related to the variety of spectral energy distributions observed from different classes of active galaxies. X-ray binaries also produce transient cosmic jets of matter that may be formed similarly to the jets and outflows that are observed from active galaxies and young stellar objects. X-ray binaries present a distinct advantage in studying these phenomena because of their compact size, which leads to variability in the energy output on short time scales. The characteristic time scales for matter to flow from the companion star through the accretion disk in an X-ray binary ranges is on order a few days, while instabilities in the inner accretion disk can form on time scales as short as a few seconds. Moreover, the production of jets from X-ray binaries has been linked to changes in the spectrum of the X-ray emission on these time scales, providing the first tantalizing clues as to how jets are launched (Mirabel & Rodríguez, 1999). Comparable phenomena would take years to observe from young stellar objects and centuries from active galactic nuclei.

X-ray binaries are also important as laboratories to study general relativity, since the high-energy emission originates from within tens of gravitational radii from the compact object. The orbital period at the inner accretion disk is shorter than a millisecond around a 1 $M_{\odot}$ compact object, which sets the shortest time scale at which significant variability has been observed (van der Klis, 2000). Nearly periodic variability in the X-ray emission on time scales as short as a millisecond has been interpreted as matter orbiting near the innermost stable orbit about the compact object (see Section 1.3.1). It may also be possible to infer the presence of an event horizon about a black hole. For instance, the luminosities of X-ray binaries thought to contain black holes appear to be systematically lower that those containing neutron stars when the rate of mass accretion is extremely low. This has been attributed to the lack of a hard surface to emit residual thermal and bulk kinetic energy in the black hole systems (Garcia et al., 2001).

In fact, X-ray binaries are the only objects in which one can find clear evidence for the black holes that are expected to be produced in the deaths of massive ($> 10\ M_{\odot}$) stars. Black hole candidates are identified by measuring the velocity of the companion star in the binary orbit through Doppler shifts of spectral absorption lines. The velocity provides a lower limit on the mass of the compact object in the binary. Since the theoretical maximum mass of a neutron star is 3 $M_{\odot}$, any compact object more massive than this is assumed to be a black hole. To date, 14 stellar-mass black holes have been identified in X-ray binaries in this manner (Orosz et al., 2002, and `http://www.astro.uu.nl/~orosz/`).

Systems containing neutron stars also contribute significantly to our understanding of the remnants of massive stars. The first neutron stars identified were isolated pulsars near the centers of supernova remnants such as the Crab nebula. The pulsations, which are observed from radio to gamma-ray energies, are thought to be produced by electrons trapped in a strong magnetic field mis-aligned with the rotational axis of the neutron star. The strengths of the magnetic fields, $B \sim 10^{12}$ G, is estimated by observing the spin periods of the pulsars slow, and assuming that rotational energy is converted to radiation by a dipole magnetic field in a vacuum. However, the spectrum of radiation from a pulsar does not resemble that expected from a magnetic dipole, so this approximation is crude at best.

Strongly-magnetized neutron stars in X-ray binaries are observed as X-ray pulsars that are powered by accretion onto their magnetic poles. These binaries also contain short-lived, massive stars, which suggests that the neutron stars are young, similar to the radio pulsars.

There are about 90 X-ray binaries containing high-mass companions that are cataloged in our galaxy, and about 20 each in the LMC and SMC. Of these high-mass X-ray binaries, at least 71 contain X-ray pulsars. The magnetic fields in accreting pulsars can be estimated directly from the energies of cyclotron lines in the X-ray spectrum. They tend to be on order 10^{12} G, similar to those inferred from isolated neutron stars (White et al., 1995).

As neutron stars age and their rotation slows, they fade away as pulsars, so that the 1000 strongly-magnetized pulsars observed in our galaxy are only a small fraction of the 10^8 neutron stars that have been produced by the evolution of massive stars throughout our galaxy's history. The exceptions to this trend are a class of millisecond radio pulsars. Many of them are observed in globular clusters, which suggests that they are old. They spin-down slowly, which implies the pulsars have weak magnetic fields, $B \sim 10^9$ G. Most importantly, the majority of them occur in binaries. For this reason, it is thought that these pulsars are spun-up by accretion as part of an X-ray binary, causing them to be re-born (Bhattacharya, 1995).

Recently, the X-ray binary progenitors of these systems have been discovered. Millisecond X-ray pulsars have been detected in two X-ray binaries with long-lived, low-mass companions (low-mass X-ray binaries, or LMXBs) (Wijnands & van der Klis, 1998; Markwardt & Swank, 2002). There are about 150 LMXBs known in our galaxy, and only a few each in the LMC and SMC. The two accreting millisecond X-ray pulsars belong to sub-class of 65 LMXBs that have been observed to exhibit X-ray bursts (see Figure 1-2, and Lewin et al., 1993, for a review). The bursts occur when accreted material that has spread over the neutron star surface ignites unstably and creates a thermonuclear explosion. The fact that the bursts occur at all implies that the magnetic fields around these neutron stars do not greatly affect the dynamics of the accretion flow. If the fields are much stronger than 10^9 G, material would be channeled onto the magnetic poles, and the local accretion rate would be too high for unstable burning to occur (Joss & Li, 1980). Since these LMXBs contain an accreting, weakly-magnetized neutron star, they have long been the natural candidates for the progenitors of the recycled radio pulsars. Now, in addition to the two X-ray pulsars, coherent millisecond pulsations have also been observed during X-ray bursts from ten LMXBs, further cementing the connection between LMXBs and millisecond radio pulsars (see Strohmayer, 2001, for a review).

The physics of the bursts themselves is quite interesting. Models of unstable nuclear burning on the surface of a neutron star reproduce the observed rise times (seconds), durations (minutes), recurrence times (hours), and total energies of the bursts ($10^{39} - 10^{40}$ erg). As matter is accreted onto the surface of the neutron star, it forms a layer about 10 m thick (see Figure 1-3). Matter at the bottom of the accreted column is compressed and heated hydrostatically, so that any hydrogen present begins to burn stably into helium via the carbon-nitrogen-oxygen (CNO) process. After several hours, the temperature becomes high enough that helium can ignite via the triple-α process. At these temperatures and pressures, helium burning is extremely unstable, and spreads over the star in a matter of seconds. This results in a burst of X-rays lasting tens to hundreds of seconds that is up to a thousand times brighter than the persistent emission between the bursts. These thermonuclear bursts allow one to study how both stable and unstable fusion reactions proceed and propagate around a neutron star's surface, and how X-rays diffuse through the stellar atmosphere.

The bursts also illuminate the surface of the neutron star, which, judging from the X-ray spectra of these systems, is usually outshone by emission from the accretion disk and boundary layer between the disk and the star. Signals observed during the bursts, such as

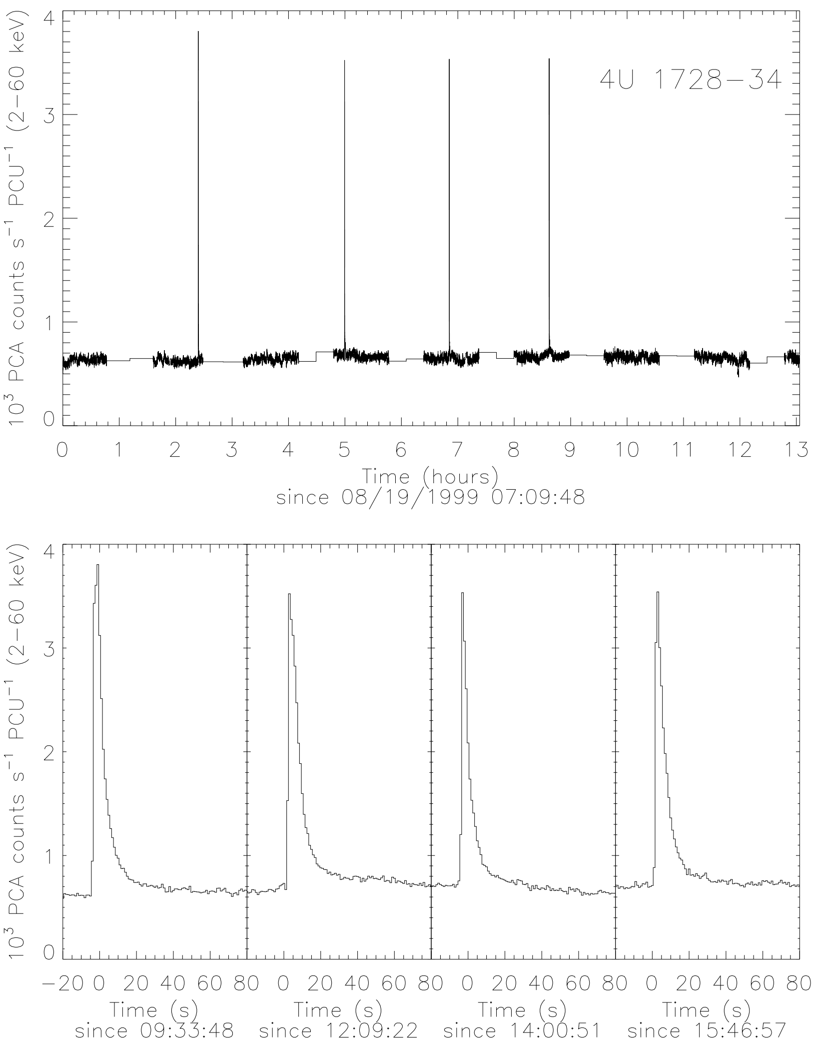

Figure 1-2 X-ray flux from 4U 1728−34 during a 13-hour observation with the Proportional Counter Array aboard the *Rossi X-ray Timing Explorer* (*Top panel*). Four bursts are clearly seen, which are expanded in the *bottom panels*.

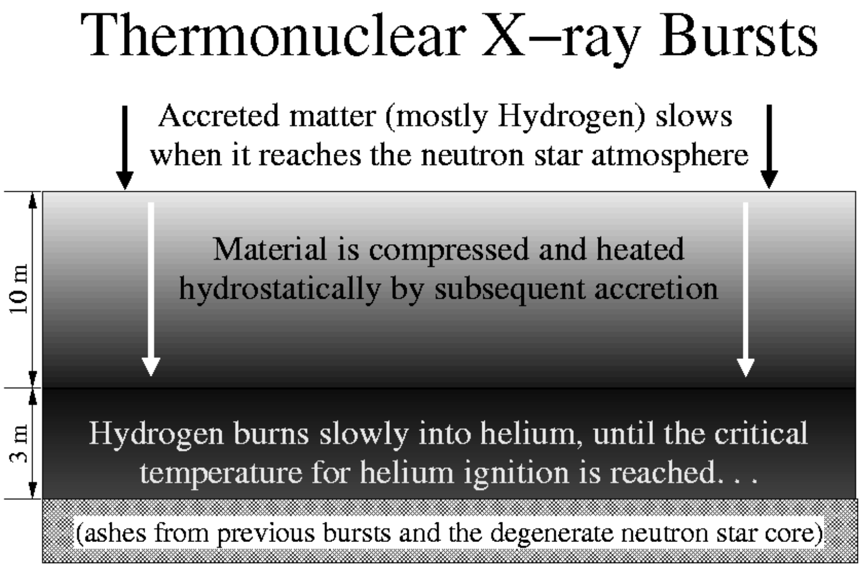

Figure 1-3 A schematic of the surface layers of an accreting neutron star.

spectral lines of a known rest energy, could allow one to measure the gravitational red-shift at the stellar surface. This would provide a measurement of the ratio of the mass and radius of the neutron star M/R, which depends sensitively upon the equation of state of nuclear matter within the star (Lattimer & Prakash, 2001). The equation of state otherwise can not be studied at these temperatures and densities in the laboratory.

This thesis explores the transient millisecond pulsations observed during X-ray bursts from weakly-magnetized neutron stars. This study encompasses a broad range of astrophysics, from the link between LMXBs and millisecond radio pulsars, the structure of the layers of accreted material on the neutron star, the process of nuclear burning on the surface, and the general relativistic signatures that should be produced by signals from the surface of a neutron star. These topics are outlined below.

1.2 The *Rossi X-ray Timing Explorer*

The *Rossi X-ray Timing Explorer* (*RXTE*; Bradt et al., 1993) is a major tool for studying X-ray variability from many classes of sources and on many time scales. One of its particular strengths is its capability to record large numbers of photons with microsecond time resolution, which led to the discovery of several new phenomena. The focus of this work, millisecond oscillations during thermonuclear X-ray bursts, were discovered in 1996 (Strohmayer et al., 1996) with *RXTE*.

RXTE carries three instruments that observe X-rays (1–200 keV) from celestial sources (Figure 1-4). Two instruments are dedicated to observations of individual sources: the High Energy X-ray Timing Experiment (HEXTE; Rothschild et al., 1998) and the Proportional Counter Array (PCA; Jahoda et al., 1996). The PCA and HEXTE are pointed simultaneously at sources within their 1° fields of view, in observations that last from 20 minutes to several days. The third instrument on *RXTE* is the All-Sky Monitor (ASM; Levine et al., 1996), which records the X-ray intensity of sources over most of the sky several times a day.

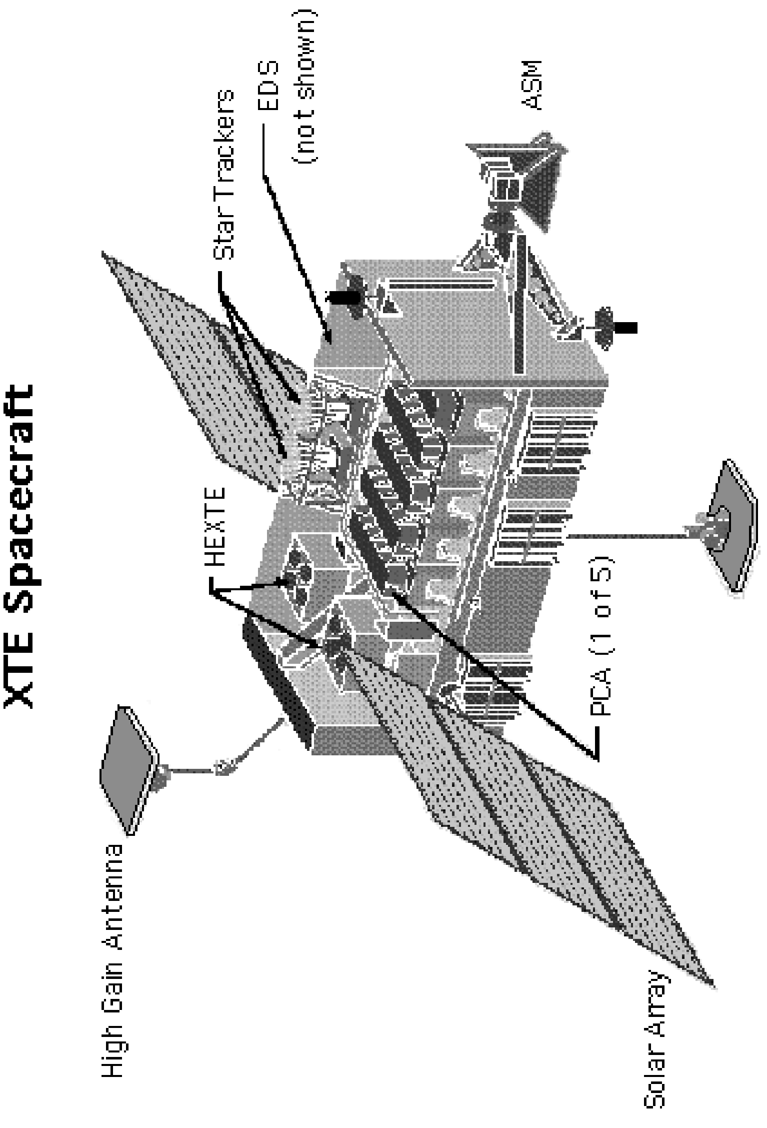

Figure 1-4 The layout of instruments aboard *RXTE*.

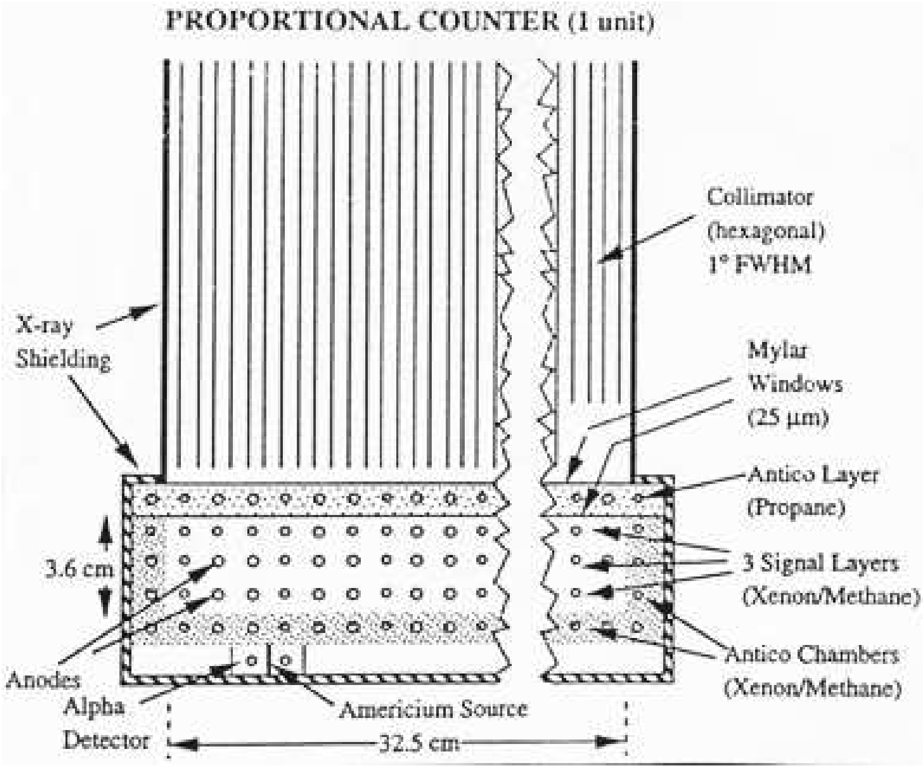

Figure 1-5 A schematic of one of the five detectors that comprise the PCA.

The PCA is composed of five gas-filled proportional counter units (PCUs) that have an area of 6000 cm^2. They are sensitive between 2.5–60 keV, and are capable of recording the arrival times of X-rays to microsecond time resolution, and their energies with an accuracy of 15%. The HEXTE has eight scintillation counters with an area of 1600 cm^2 between 15–200 keV, and is also capable of μs time resolution and moderate energy resolution. The PCA is the main instrument used for this thesis, since X-ray bursts exhibit thermal spectra with temperatures less than 3 keV and therefore are most easily detected in the PCA bandpass. For this reason, it is worth discussing the instrument in some detail.

A schematic of one of the PCUs is displayed in Figure 1-5. Each PCU contains two gas-filled chambers. The chamber directly behind the mylar entry window contains propane, and serves as an anti-coincidence detector to reject particles entering the front of the detector. The inner xenon layer serves as the X-ray detector. Both chambers are traversed by anodes held at high positive voltage with respect to the outer casing of the detector. A photon that enters the chamber ionizes an atom of the gas, releasing an electron that ionizes further atoms. The resulting cloud of electrons is accelerated by the electric field toward the nearest anode, causing them to ionize yet more atoms of the gas. The total number of electrons produced is proportional to the energy of the original photon. The cloud of electrons quickly reaches the anode, and is read out by the electronics on board as a voltage. The voltage is interpreted by a pulse-height analyzer, which assigns an energy channel to the event. This whole process takes less than a microsecond, so the time at which a photon arrives at the detector can be recorded with high accuracy.

All of the events from the five PCUs are then sent to a set of six event analyzers (EAs) that are part of the Experiment Data System (EDS). The EDS reduces the bandwidth needed to transmit the data to earth by encoding the information in one of several pre-defined modes. The two Standard modes always operate, and record (*i*) the number of photons from each PCU with 0.125 s time resolution, and (*ii*) 16 s integrations of the energy spectrum with 128 channels of resolution. The observer may specify data modes for the four remaining EAs, while conforming to the overall telemetry limits imposed on the mission (about 40 kbit s^{-1} are available to the PCA). The most commonly used modes (*i*) telemeter event-by-event information with a fixed number of bits to encode time and energy information (Event and GoodXenon modes), (*ii*) telemeter the number of photons received in time and energy bins (Binned modes, of which the Standard modes are examples), or (*iii*) simply record whether or not a photon was received in a given energy range during a time interval (Singe-bit modes). It is also possible to request modes that only record when a X-ray intensity threshold is exceeded, because the memory buffers for modes with high time and energy resolution will often get over-written if a source gets bright suddenly. These Burst-catcher modes are used extensively to study X-ray bursts, in order to increase the time or spectral resolution during the bursts without exceeding the telemetry limits.

The particular advantages that the PCA provides over previous detectors are its large collecting area and high time resolution. These features allow for the efficient detection and characterization of time-varying signals in relatively short observations. Observations with the PCA have provided the discoveries of the two accreting millisecond X-ray pulsars, the ten burst oscillations sources, and the 20 sources of kHz QPOs — all of the phenomena that are crux of this thesis.

The third instrument is the ASM, which consists of three position-sensitive proportional counters with coded apertures. It samples the X-ray intensity of bright sources (> few mCrab) several times a day in three energy channels between 1–12 keV. The ASM rotates on its own pedestal, and covers most of the sky each day in a series of 90 s snapshots. The ASM archive provides unprecedented detail about the time variability of persistent X-ray sources on time scales of hours to years. The ASM is also responsible for the discovery of ~ 20 transient X-ray sources in its first six years of operation.

Since most X-ray binaries are quite variable, *RXTE* was designed to respond rapidly to transient phenomena. The observing program for the satellite can be adjusted in as little as 30 minutes to accommodate unanticipated opportunities, ranging from X-ray novae discovered with the ASM to gamma-ray bursts. This flexibility also allows for complex observing schedules that mix monitoring programs of active galactic nuclei and X-ray pulsars with longer observations of a wide variety of targets. This is advantageous, because the large effective areas of the PCA and HEXTE make short observations scientifically valuable. After the first six years of its mission, the database of PCA and HEXTE observations contains hundreds of hour-long samples of each of the brightest LMXBs, totaling a few million seconds of exposure time apiece. This has enabled studies of these sources over a range of accretion rates and on many different time scales (e.g. van der Klis, 2000; Muno et al., 2002). This thesis summarizes the sample of bursts and oscillations detected with the PCA from four transient and four persistent LMXBs.

1.3 Oscillations During Thermonuclear Bursts

Burst oscillations have now been detected from ten weakly-magnetized LMXBs (Table 1.1 and references therein). The oscillations last for only a few seconds, and their frequencies are distributed evenly between 270–620 Hz (see Figure 1-6).[1]

It has long been expected that oscillations at the stellar spin frequency should occur during thermonuclear bursts, since the burning probably begins at a definite point on the neutron star (e.g., Bildsten, 1995; Strohmayer et al., 1996). At the start of a burst, any hot regions will rotate into and out of the observer's line-of-sight, producing an oscillation with a fractional amplitude that decreases rapidly as the burning front engulfs the surface of the neutron star. As predicted, the flux at the start of a burst is often highly modulated, while the fractional amplitudes decrease rapidly as the burning region appears to grow to cover the entire neutron star (Strohmayer et al., 1997a, but see below).

The stability of the oscillations also supports the conjecture that they result from brightness patterns on the stellar surface. On short time scales, the oscillations are highly coherent towards the ends of bursts (Strohmayer et al., 1996; Strohmayer & Markwardt, 1999). The frequencies are also remarkably constant, to a few parts in 1000, in bursts separated by several years (Strohmayer et al., 1998; Muno et al., 2000). A coherent pulsation was even observed for 600 s during an hour-long "super burst" from 4U 1636−536, at the same frequency as the short-lived burst oscillations. The frequency of the oscillation increased slightly with time, in a manner consistent with Doppler shifts from the known orbital period of the binary (Strohmayer & Markwardt, 2002). The spin of a neutron star is the only frequency that is expected to be this stable. The fact that these signals originate from a neutron star's surface raises the possibility of measuring the physical parameters of the LMXB — the mass, radius, and spin of the neutron star, and the mass of the companion.

However, a closer examination of these burst oscillations suggests that complex physics must underly the formation of any bright regions on the neutron star (see Figure 1-7 and Psaltis, 2001, for a discussion). First, the oscillations persist for longer than is expected, far into the decay of the burst (e.g., Smith et al., 1997). The fuel over the entire surface of the neutron star is expected to have ignited by the time the flux from the burst has peaked, leaving no observable brightness anisotropies (e.g. Fryxell & Woosley, 1982). Second, while the spin of a neutron star must be constant during the course of a burst, the frequencies of the oscillations are usually observed to increase and saturate at some maximum frequency (Strohmayer et al., 1997b). It is these "asymptotic" frequencies that appear stable in bursts separated by several years. The frequency drifts are thought to originate from one of several mechanisms that might carry brightness patterns in the opposite direction from the spin of the neutron star in the rotating frame, resulting in frequencies slightly lower than those of the stellar spins in the observer's non-rotating frame (Strohmayer et al., 1997b; Cumming & Bildsten, 2000; Spitkovsky et al., 2002; Heyl, 2002).

First, Strohmayer et al. (1997b) suggested that the oscillations originate from hot regions on a burning layer that decouples from the neutron star. They suggest that the release of nuclear energy when the burning commences causes the layer to expand by ~ 10 m, while conservation of angular momentum causes it to slow as it expands. The oscillations must only be observed when the burning layer begins to contract, which causes them to increase in frequency as the layer re-couples to the neutron star. However, recent calculations suggest that the expansion of a rigidly rotating burning layer would only create a frequency drift

[1]Note that 400 Hz oscillations have been observed during a burst from the millisecond X-ray pulsar SAX J1808.4-3658 as well, using the Wide Field Camera aboard *BeppoSAX* (in't Zand et al., 2001). These observations were not sensitive enough to detect some of the detailed behavior that is characteristic of burst oscillations, which is outlined below, so the pulsations conceivably could result from an independent mechanism.

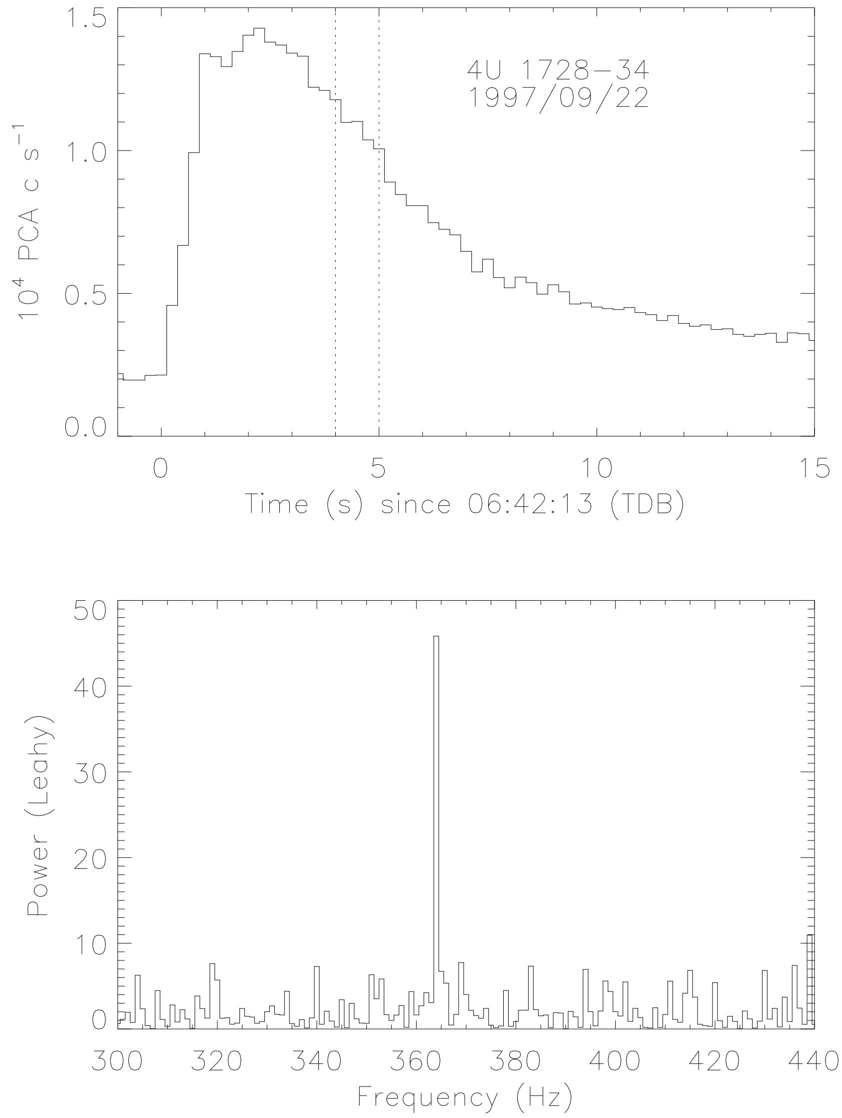

Figure 1-6 *Top panel*: The X-ray intensity (2–60 keV) as a function of time from a burst from 4U 1728−34 observed with the *RXTE* PCA. *Bottom Panel*: A Fourier power spectrum of the X-ray flux during the interval indicated by the dotted lines (4–5 s). It demonstrates that there is an oscillation near 363 Hz. The power has been normalized so that Poisson noise has a mean value of 2.

Table 1.1. Sources of Burst Oscillations

Source	$\nu_{\rm burst}$ (Hz)	Ref.
4U 1608−522	620	[1]
SAX J1750−2900[a]	600	[2]
MXB 1743−29	589	[3]
4U 1636−536	581	[4]
MXB 1659−298	567	[5]
Aql X-1	549	[6]
KS 1731−260	524	[7]
4U 1728−34	363	[8]
4U 1702−429	329	[9]
4U 1916−053	270	[10]

[a]Oscillations from this source were discovered as this thesis was being written, so are not included in the rest of this thesis.

References. — [1] Chakrabarty, priv. comm.; [2] Kaaret et al. (2002); [3] Strohmayer et al. (1997b); [4] Zhang et al. (1997); [5] Wijnands et al. (2001); [6] Zhang et al. (1998) ; [7] Smith et al. (1997) ; [8] Strohmayer et al. (1996); [9] Strohmayer & Markwardt (1999); [10] Galloway et al. (2001)

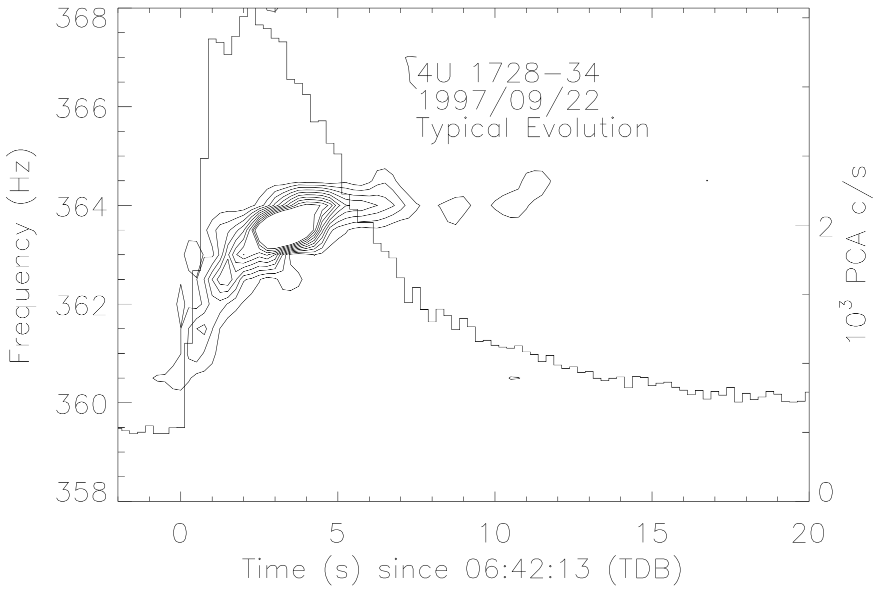

Figure 1-7 The same burst as in Figure 1-6, demonstrating that the oscillation evolves by nearly 3 Hz. The oscillation is illustrated with a dynamic power spectrum, in which we plot contours of power as a function of time and frequency. The PCA count rate showing the burst profile is also plotted referenced to the right axis.

of $\Delta\nu/\nu \approx 5 \times 10^{-3}$, which is significantly smaller than the 1.5% frequency drifts observed (compare Cumming & Bildsten, 2000; Cumming et al., 2002).

Alternatively, Spitkovsky et al. (2002) pointed out that vortices could form in a geostrophic flow driven by the combination of the Coriolis force and a pressure gradient between the equator and the poles. The pressure gradient could form if equator ignites first due to the higher column density of fuel where the surface gravity is low, then cools more quickly than the poles during the tail of the burst. The Coriolis force would then convert motion toward the equator into a zonal flow moving opposite the rotation of the star. Vortices could form due to zonal shear, similar to weather systems on Earth and Jupiter. They would have to appear as light or dark regions on the neutron star to produce oscillations. The frequency drift in this model is attributed to the slowing of the geostrophic flow as the temperature gradient decreases.

Finally, Heyl (2002) has proposed that the burst could excite global oscillation modes that propagate as density waves on the neutron star ocean. The velocity with which these waves travel is extremely sensitive to the vertical density and temperature structure, as well as to the surface composition, and thus could change during the burst. Indeed, in all these models, the mechanisms producing the pulsations depend strongly on the properties of the neutron stars, and thus potentially offer a powerful probe of the physical conditions in their outer layers. Therefore, it is important to determine which, if any, of these mechanisms produces the burst oscillations.

A detailed study of the properties of the frequency evolution provides one means of distinguishing between the models. Information may also be obtained from the amplitudes and pulse profiles of the oscillations, which are determined largely by the size and location of the brightness pattern. Each model outlined above forms patterns that should have very different properties. Hot regions due to anisotropic burning (Strohmayer et al., 1997b) will form wherever burning preferentially ignites, but should have varying sizes. Hydrodynamical instabilities (Spitkovsky et al., 2002) will probably form at intermediate latitudes and cover rather small areas. Global oscillation modes (Heyl, 2002) will likely be symmetric. The amplitudes and harmonic content of the oscillations therefore may determine which mechanism is responsible for them.

The amplitudes and profiles of the oscillations could also reveal the mass and radius of the neutron star. The propagation of photons from the surface of a rapidly rotating neutron star is affected by general relativity, time delays, and Doppler shifts (Miller & Lamb, 1998; Braje et al., 2000; Weinberg et al., 2001; Nath et al., 2002). In particular, strong gravitational lensing by the neutron star allows a bright region on its surface to be seen for a large fraction of the rotational period. This places a limit on the largest possible amplitude of the oscillations, so that high-amplitude oscillations would rule out very compact stars (see Nath et al., 2002). On the other hand, Doppler and time delay effects cause the pulse profiles to be more asymmetric and narrowly-peaked, which increases the amplitudes and the harmonic content of the oscillations (Weinberg et al., 2001; Braje et al., 2000). The unambiguous detection of rotational effects in the light curve would provide a measurement of the surface velocity — and therefore the mass to radius ratio — of the neutron star.

Finally, several anomalies have been observed in the frequency evolution of the oscillations that are not addressed by current models. The coherence of the oscillations is cast into some doubt by the detection of a sudden 1/4 cycle phase shift in one oscillation out of seven studied by Strohmayer (2001). A bright region on a neutron star would have to suddenly change its longitude by 90° in order to produce such a phase jump. Moreover, in a handful of bursts there are episodes of drifts to lower frequencies in the tails of the bursts ("spin-down"; see Strohmayer, 1999; Miller, 2000; Muno et al., 2000) and strong detections of signals at second frequencies within a few Hz of the primary signal (Miller, 2000; Galloway et al., 2001). A census of these anomalies is needed to determine their importance in developing models for the oscillations.

1.3.1 Kilohertz Quasi-Periodic Oscillations

The models and interpretations of burst oscillations also carry important ramifications for our understanding of other millisecond signals that are observed during the persistent X-ray emission between bursts (see Figure 1-8). These signals occur between 200–1200 Hz in Fourier power spectra of the persistent emission from twenty LMXBs, but are not strictly coherent, with $Q \sim 3-100$ (van der Klis, 2000). They are therefore referred to as kilohertz quasi-periodic oscillations (kHz QPOs). These kHz QPOs may reflect the relativistic motions of transient features orbiting near the inner edge of the accretion disk (Strohmayer et al., 1996; Miller et al., 1998; Stella & Vietri, 1999). The QPOs sometimes appear in pairs, separated by a frequency difference $\Delta\nu_{\rm kHz}$ that varies only by 40% as the frequencies of the peaks increase by more than a factor of 2 (Strohmayer et al., 1996; van der Klis et al., 1997). Moreover, in the sources that also exhibit burst oscillations, their frequency is related to the difference frequency by $\nu_{\rm burst} \approx m \times \Delta\nu_{\rm kHz}$, where $m = 1$ when $\nu_{\rm burst} \approx 300$ Hz and $m = 2$ when $\nu_{\rm burst} \approx 600$ Hz. These facts have been interpreted according to beat-frequency models that identify $\Delta\nu_{\rm kHz}$ as the spin frequency of the neutron star, $\nu_{\rm spin}$ (Strohmayer et al., 1996; Miller et al., 1998; Osherovich & Titarchuk, 1999). If $\Delta\nu_{\rm kHz} = \nu_{\rm spin}$, then two bright

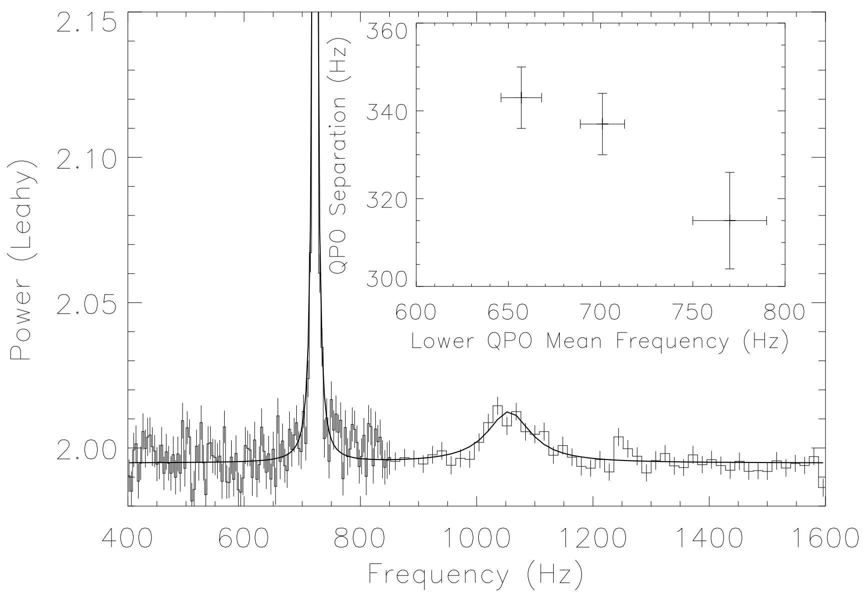

Figure 1-8 Twin kHz QPOs observed in the persistent emission between bursts from 4U 1702−429. The power has been normalized so that Poisson noise has a mean value of 2. *Inset*: The frequency difference between the QPOs varies much less than the frequencies of the QPOs themselves, and is nearly the same as the 329 Hz burst oscillations. Taken from Markwardt et al. (1999).

regions must be present on neutron stars with $\nu_{\rm burst} \approx 600$ Hz, in order for the strongest signal to be produced at $2 \times \nu_{\rm spin}$. The detection of a half-frequency signal at 290 Hz in a combined sample of bursts from 4U 1636−536 has strengthened the suggestion that $\nu_{\rm burst}$ is indeed $2 \times \nu_{\rm spin}$ in this source (Miller, 1999). However, the putative signal at $\nu_{\rm spin}$ may only be present in a single burst, and has not been detected in searches of independent samples of bursts (Strohmayer, 2001), nor in oscillations observed for 600 s during an hour-long "superburst" from this same source (Strohmayer & Markwardt, 2002).

It is particularly important to determine whether $\nu_{\rm burst} = 2 \times \nu_{\rm spin}$ in the subset of sources with 600 Hz oscillations, because it implies that $\Delta\nu_{\rm kHz} \approx \nu_{\rm spin} \approx 300$ Hz in all 20 of these LMXBs. Millisecond spin periods would support the suggestion that these neutron star LMXBs are the progenitors of recycled millisecond radio pulsars (Alpar et al., 1982). However, a limit of ∼300 Hz to the spin frequency would also imply that some mechanism limits the frequencies to which these stars can be spun-up by accretion. A correlation between the surface magnetic field strength and X-ray luminosity could limit the torque that the accretion disk exerts on the neutron star (White & Zhang, 1997). Gravitational radiation from a quadrupole moment in the mass distribution of the neutron star could also limit the spin period (Bildsten, 1998).

1.4 The Diversity of Type I X-ray Bursts

While Type I X-ray bursts have been observed from more than 60 low-mass X-ray binary systems (LMXBs; see Lewin et al. 1993 for a review, and Liu et al. 2001), oscillations have only been observed from 10 sources. Even in sources where the burst pulsations are seen, not all bursts show them, which suggests that the creation of brightness patterns on the stellar surface requires special conditions. These conditions may be inferred from the properties of the bursts that produce oscillations, and could constrain the mechanism responsible for the oscillations (Cumming & Bildsten, 2000).

Detailed models predict variations in the frequency, strength, and time scales of bursts from a single source due to changes in the composition of the burning material. This is in turn determined by the metallicity of the matter accreted onto the neutron star, the amount of hydrogen burned during the time between bursts, and the amount of fuel left-over from the previous burst (Fujimoto et al., 1981; Ayasli & Joss, 1982; Fushiki & Lamb, 1987; Fujimoto et al., 1987; Bildsten, 1997). In addition, variations from source to source are expected because of differences in the core temperatures of the neutron stars and the average accretion rate onto the surface (Ayasli & Joss, 1982; Fushiki & Lamb, 1987).

The theoretical models that are most readily compared to observations are those that predict how burst properties in an individual system should change as the accretion rate onto the neutron star varies. The model of Fujimoto et al. (1981) is illustrative in this regard. They predict that X-ray bursts should occur in three regimes depending on the accretion rate ($\dot{M}$), which they label Cases 1, 2, and 3. I denote these regimes in units of the critical accretion rate above which the energy released exceeds the Eddington luminosity, $\dot{M}_{\rm Edd}$ (Frank et al., 1995, pg. 84). At the lowest accretion rates ($< 0.01\dot{M}_{\rm Edd}$, Case 3), the temperature in the burning layer is too low for stable hydrogen burning; the hydrogen ignites unstably, in turn triggering helium burning, which produces a type I X-ray burst in a hydrogen-rich environment. At higher accretion rates ($0.01 <\dot{M}_{\rm Edd} < 0.1$, Case 2), hydrogen burns stably into helium as quickly as material is accreted onto the neutron star. A pure helium layer develops at the base of the accreted material, and heats steadily until a rapid and intense helium burst is triggered. At higher accretion rates ($0.1 <\dot{M}_{\rm Edd}< 1$, Case 1), material is accreted faster than it can be consumed by hydrogen burning (which is limited by the rate of β-decays in the CNO cycle), so that the helium again ignites unstably in the H-rich environment (see Bildsten 1998 for dependences of these accretion rates on the metallicities). At the highest accretion rates ($>\dot{M}_{\rm Edd}$), stable helium burning becomes important on the surface of the neutron star, which depletes the primary fuel reserves and causes bursts to occur less frequently.

Hanawa & Fujimoto (1982) point out that the luminosities of neutron star LMXBs that have been observed to burst imply accretion rates from $\sim 0.01 - 0.1\ \dot{M}_{\rm Edd}$, so that an individual source that varies in luminosity should exhibit changes in its bursting behavior between Case 2 and Case 1. This has been difficult to test. The accretion rate varies on time scales of weeks to months (Muno et al., 2002), much longer than the average observation. Of the ~ 60 bursting LMXBs, the majority of sources either exhibit few bursts, or several bursts are seen in a single luminosity state (Lewin et al., 1993).

Only about ten sources have been observed to burst over a range of luminosities, and these have produced some perplexing results. For instance, as the accretion rate increases, the column of material above the burning layer builds more quickly, and thus the time required to reach the critical temperature for unstable helium burning decreases. This is consistent with the increase in burst rate with persistent flux observed in 4U 1728−34 (Basinska et al., 1984) and 4U 1820−30 (Clark et al., 1977). At the highest accretion rates, steady helium burning reduces the amount of fuel for X-ray bursts. This causes bursts to occur less often, as seen in EXO 0748−676 (Gottwald et al., 1986) and 4U 1705−44 (Langmeier et al., 1987), or not at all, as observed in 4U 1820−30 (Clark et al., 1977) and

GX 3+1 (Makishima et al., 1983). However, no correlation was found between persistent flux and burst recurrence times in Ser X-1 (Sztajno et al., 1983), 4U 1735−44 (Lewin et al., 1980; van Paradijs et al., 1988b), and 4U 1636−536 (Lewin et al., 1987). This suggests either that an additional mechanism contributes to the frequency of bursts, or that the persistent flux is not a good measure of the accretion rate in these sources.

The change in the composition of the burning layer as the accretion rate increases should affect the properties of the bursts. Helium burning occurs via the triple-α process, which is moderated by the strong nuclear force and proceeds very quickly at the temperatures and densities of the burning layer. Hydrogen burning proceeds more slowly, because it is limited by a β-decay that is moderated by the weak force. Therefore, faster, more intense bursts characteristic of a helium-rich burning layer should occur at relatively low accretion rates (Case 2), while hydrogen-rich bursts with slower rise and decay times should occur at higher rates (Case 1). Surprisingly, most sources behave in the opposite manner. The decay time scales of bursts from 4U 1608−52 (Murakami et al., 1980), 4U 1636−536 (Lewin et al., 1987), and 4U 1705−44 (Langmeier et al., 1987) have all been reported to *decrease* as the apparent $\dot{M}$ increases from 0.01–0.1 $\dot{M}_{\rm Edd}$. A survey of ten LMXBs by van Paradijs et al. (1988a) also revealed a global decrease in burst duration with increasing flux. This is precisely opposite the trend that would be expected from a shift from Case 2 and Case 1 of Fujimoto et al. (1981). The origin of this discrepancy is uncertain. It appears that we do not understand either how the composition of the burning layer varies with the accretion rate, or how the accretion rate on the surface varies with the amount of persistent X-ray flux (see Bildsten 2000 for a recent discussion). Further observations are clearly warranted.

1.5 Organization of this Thesis

This thesis can be roughly divided into two parts. In the first part of this thesis, I investigate the phenomenology of burst oscillations in order to (*i*) constrain the models thought to be responsible for the oscillations, (*ii*) determine whether the velocities of the neutron stars in their binariy orbits can be measured from teh burst oscillations, (*iii*) explore the relationship between $\nu_{\rm spin}$ and $\nu_{\rm burst}$, which is important for understanding the star's rotational history, and (*iv*) establish whether the oscillations can be used to constrain the mass and radius of the neutron star. My sample for this study consists of 68 oscillation trains that have been observed with *RXTE* from 8 different sources.

In Chapter 2, I use Fourier timing techniques to identify and characterize this sample. I then determine over what frequency range burst oscillations are observed to drift, and how often anomalies such as spin-down episodes and simultaneous signals at two frequencies are observed. These observations provide a qualitative test of our expectations for the properties of burst oscillations.

In Chapter 3, I explore how stable the oscillations are. I examine the frequency evolution of our sample of burst oscillations using a "phase connection" method often applied to pulsar timing studies (Manchester & Taylor, 1977; Deeter et al., 1981). Using this method, I determine whether the frequency evolution is consistent with smooth models (i.e. low-order polynomials and exponentials), or equivalently, how often sudden phase or frequency jumps are observed. I then examine how stable the maximum observed frequencies are for a given source in bursts separated by up to five years. The stability of the oscillations provides information on how the velocity of the brightness patterns is determined. If the oscillations are stable enough, it also may be possible to measure the velocity of the neutron star in its binary orbit. This would constrain the mass of the two binary components, which is important in determining the evolutionary history of the LMXB.

In Chapter 4, I search for connections between the evolution of the frequencies and amplitudes of the oscillations and the spectra and time scales of the underlying bursts. If the frequencies and amplitudes of the oscillations are related to the energy released from the burning layer, clear correlations may be evident. This could distinguish between the several mechanisms that have been proposed to explain the oscillations.

In Chapter 5, I examine the profiles of the oscillations in order to constrain the properties of the surface brightness patterns thought to be responsible for them. I quantify the shape of the profiles by measuring the amplitudes of their Fourier components. Then, I present theoretical predictions of the signal that an observer would see from one or two bright regions on the surface of a rapidly rotating neutron star. I explore a range of parameters relevant to the burst oscillations, and explicitly take into account the response of the *RXTE* PCA detector to allow a direct comparison with the data (compare Miller & Lamb, 1998; Braje et al., 2000; Weinberg et al., 2001). I place quantitative constraints on the number, location, and size of bright regions on the neutron star surface by comparing the theoretical calculations to observations. This restricts which mechanisms could be responsible for the oscillations. It also lays the groundwork for determining how $\nu_{\rm spin}$ and $\nu_{\rm burst}$ are related, and for constraining the mass and radius of the neutron star. Details of the physics included in the models are provided in Appendix A.

The second part of this thesis (Chapters 6 and 7) has two goals: (*i*) to establish how the burst behavior varies with the apparent accretion rate onto the neutron star, and (*ii*) to determine in which bursts or at what accretion rates the oscillations appear. It is possible that some physical property can be found, such as the metallicity of the burning layer, that determines whether or not oscillations are observed. In Chapter 6, I examine one source, KS 1731−260, in detail as a case study. In Chapter 7, I briefly examine the properties of bursts that exhibit oscillations in nine sources from which they have been observed.

1.5.1 Notes on the Text

Sections of this introduction were adapted from the papers "Nearly Coherent Oscillations in Type I X-Ray Bursts from KS 1731−260" by Michael P. Muno, Derek W. Fox, Edward H. Morgan, and Lars Bildsten (*The Astrophysical Journal*, volume, 542, pages 1016–1033, 2000), "The Frequency Stability of Millisecond Oscillations during Thermonuclear X-Ray Bursts" by Michael P. Muno, Duncan K. Galloway, Deepto Chakrabarty, and Dimitrios Psaltis (submitted to *The Astrophysical Journal*), and "The Amplitudes and Harmonic Content of Millisecond Oscillations During Thermonuclear X-ray Bursts" by Michael P. Muno, Feryal Özel, and Deepto Chakrabarty (submitted to *The Astrophysical Journal*). These papers, along with "Millisecond Oscillations and Photospheric Radius Expansion in Thermonuclear X-Ray Bursts" by Michael P. Muno, Deepto Chakrabarty, Duncan K. Galloway, and Pavlin Savov (*The Astrophysical Journal*, volume 553, pages L157–L160, 2001) also have been adapted for the text of the following chapters. The sources are indicated at the start of each chapter.

In addition, "Nearly Coherent Oscillations in Type I X-Ray Bursts from KS 1731−260" was included in its entirety in the Ph.D. thesis of Derek W. Fox (MIT, 2000). The portions used in Chapter 6 of the current work are those for which I carried out the data analysis and wrote the text.

Finally, portions of "The Amplitudes and Harmonic Content of Millisecond Oscillations

During Thermonuclear X-ray Bursts" are included in the Ph.D. thesis of Feryal Özel (Harvard, 2002). The development of many of the conclusions in that paper was a collaborative effort. I performed the observational data analysis, and the analysis of the theoretical results. Feryal Özel and Dimitrios Psaltis wrote the theoretical code to account for curved photon paths in a Schwarzschild metric, and I adapted it to take into account rotational effects.

Chapter 2

The Sample of Oscillations

> This chapter is adapted from the paper "The Frequency Stability of Millisecond Oscillations during Thermonuclear X-Ray Bursts" by Michael P. Muno, Duncan K. Galloway, Deepto Chakrabarty, and Dimitrios Psaltis, which has been submitted to *The Astrophysical Journal.*

As a first step in this study, we present a general survey of the oscillations observed during thermonuclear X-ray bursts. We first establish a sample of oscillations, by searching Fourier power spectra of the X-ray intensity during the bursts (Section 2.2). This section also contains a description of most of the Fourier timing techniques that are used throughout this thesis. We then determine the range of fractional rms amplitudes that the oscillations exhibit, and search for signals at integer and half-integer multiples of the main frequencies (Section 2.2.1). Next, we examine over what frequency ranges the oscillations are observed in each source, which gives a measure of the amount of frequency drift and provides a test of whether there is an upper bound to the frequencies of the oscillations (Section 2.2.2). Finally, we search the sample of oscillations for instances of frequency evolution that are not consistent with a saturating upward drift, such as drifts toward lower frequencies ("spin-down") and instances of two frequencies detected simultaneously (Section 2.2.3).

2.1 Observations

We searched publicly available PCA observations for large deviations in the X-ray intensity of LMXBs that could be caused by thermonuclear bursts. We have checked each candidate burst to confirm that it is thermonuclear in origin, and found 452 X-ray bursts from 34 different LMXBs. As of September 2001 we have found 159 bursts from 8 of the sources that are also known to exhibit burst oscillations.[1] These sources are listed in Table 2.1.

For all of the timing analysis presented in this thesis, we converted the TT photon arrival times at the spacecraft to Barycentric Dynamical Time (TDB) at the solar system

[1]Oscillations in bursts associated with MXB 1743−29 have been observed during observations of the bursting pulsar GRO J1744−28. When the bursting pulsar is active, it emits hundreds of X-ray bursts that originate from instabilities in its accretion disk. This makes the search for a few thermonuclear bursts from a source in the same PCA field of view quite tedious, so we have not included MXB 1743−29 in the current project. The tenth source was discovered while the final version of this thesis was being written, as noted in Table 1.1.

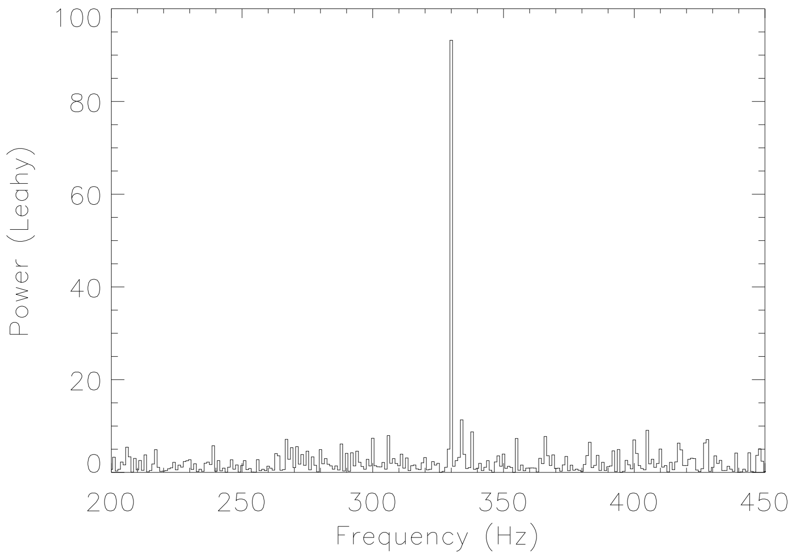

Figure 2-1 Section of a power spectrum from a 1 s interval of a burst from 4U 1702−429 that occurred on 1997/07/30. The power is normalized according to the criteria of (Leahy et al., 1983). An oscillation is clearly present at 329 Hz, while the rest of the power spectrum is dominated by Poisson noise normalized to have a mean power of 2.

barycenter, using the Jet Propulsion Laboratory DE-200 solar system ephemeris (Standish et al., 1992).

2.2 Characteristics of Oscillations

To search for burst pulsations in a uniform manner, we produced Fourier power spectra (see van der Klis 1989, Leahy et al. 1983, and Vaughan et al. 1994 for in-depth discussions) from PCA data with a time resolution of 2^{-13} s combined into a single energy channel (2.5–60 keV). The discrete power spectrum is defined as

$$a_j = \sum_{k=0}^{N-1} x_k e^{2\pi ijk/N}, \tag{2.1}$$

where x_k is the signal as a function of time, k is the time bin, N is the number of points transformed, and j is the frequency bin. The frequency is $\nu_j = j/T$, where T is the total integration time. The largest observable (Nyquist) frequency is $\nu_{\rm Nyq} = 0.5(\Delta T)^{-1}$, where ΔT is the time resolution of the data. We used the Fast Fourier Transform algorithm in Press et al. (1992) to compute power spectra.

Burst oscillations are observed above 100 Hz, where the power spectra are dominated by Poisson counting noise at most frequencies. Figure 2-1 illustrates an example power spectrum from a 1 s interval of a burst from 4U 1702−429. Other than Poisson noise, the only signal evident is the 329 Hz burst oscillation. Therefore, we normalize the power

Table 2.1. Burst Oscillations from LMXBs

Source	$\nu_{\rm burst}$ (Hz)	Number of Bursts	Osc.
4U 1608−522	620	6	1
4U 1636−536	581	24	17
MXB 1659−298	567	15	5
Aql X-1	549	17	3
KS 1731−260	524	13	5
4U 1728−34	363	66	27
4U 1702−429	329	11	8
4U 1916−053	270	7	1

spectra according to the criteria of Leahy et al. (1983),

$$P_j = \frac{2|a_j|^2}{I_\gamma}, \tag{2.2}$$

where I_γ is the total number of counts in a transform, so that noise powers are described by a chi-squared distribution with two degrees of freedom.

With this definition, we can easily establish whether a signal P is significant given the noise in the power spectrum. If we take $1 - C$ to be the certainty that a signal is not due to noise, in the limit that C is small we approximate the threshold power $P_{\rm th}$ above which we think a signal is real by

$$P_{\rm th} = 2\ln(N_{\rm trial}) + 2\ln\left(\frac{1}{C}\right), \tag{2.3}$$

where $N_{\rm trial}$ is the number of bins in the power spectra that we have searched (Vaughan et al., 1994).

For our search, we computed power spectra of 1 s intervals from the first 16 seconds of each burst, starting with the second before the burst rise. We searched these power spectra over 10 Hz frequency intervals centered on the frequencies in Table 2.1. The adequacy of the width of the frequency window for detecting burst oscillations will be confirmed in Section 2.2.2[2]. Each burst requires 160 trials to search, and we searched 159 bursts. Our threshold power is $P_{\rm th} = 24.9$, where any signal stronger than $P_{\rm th}$ has less than a 10% chance of occurring randomly due to Poisson noise, given all of the bins searched. We detected 68 oscillations from these 8 sources, as indicated in Table 2.1. We also recorded the frequencies of each signal detected. The frequencies in Table 2.1 were determined recursively for each source by computing the median value (rounded to the nearest Hz) from the signals detected until that value did not change.

[2]A more general search for oscillations at all frequencies was carried out by Pavlin Savov and Duncan Galloway, but did not reveal any other significant signals

2.2.1 Amplitudes of Oscillations

We next computed the fractional rms amplitudes A of the detected oscillations. For a sinusoidal signal, we take

$$x(t) = x_o[1 + \sqrt{2}A\sin(\omega t + \phi)] + b, \tag{2.4}$$

where x_o is the average source count rate and b is the background, so that $I_\gamma = (x_o + b)T$. If the power spectra were continuous functions, we could compute A according to

$$A = \left(\frac{P}{I_\gamma}\right)^{1/2} \frac{I_\gamma}{I_\gamma - B_\gamma}, \tag{2.5}$$

where $B_\gamma = bT$ is the number of those counts that are from the background. However, the discrete power spectra we have computed are less sensitive to both high frequency signals and to oscillations that fall between the centers of two frequency bins (Leahy et al., 1983). The binned signal with the mean count rate subtracted is

$$x_k = \frac{2x_o\sqrt{2}A}{\omega}\sin\left(\frac{\omega T}{2N}\right)\sin\left(\frac{\omega T}{N}\left[k - \frac{1}{2}\right] + \phi\right). \tag{2.6}$$

To estimate the power from an arbitrary signal, we have to integrate over all ϕ and over all ω in the frequency bin $2\pi\nu_j$. The power turns out to be

$$|a_j|^2 = 0.773\left(\frac{x_o\sqrt{2}ATN}{2\pi j}\right)^2 \sin^2\left(\frac{\pi j}{N}\right). \tag{2.7}$$

Applying our definition for the normalization of the power spectrum (Equation 2.2), I can compute the fractional rms amplitude given the power from Equation 2.7:

$$A = \left(\frac{P_j}{0.773 I_\gamma}\mathrm{sinc}^{-2}\left(\frac{\pi}{2}\frac{\nu_j}{\nu_{\mathrm{Nyq}}}\right)\right)^{1/2} \frac{I_\gamma}{I_\gamma - B_\gamma}. \tag{2.8}$$

The sinc term originates from averaging over the possible phases ϕ of the oscillation, and is unity at low frequencies, but nears 0.405 at the Nyquist frequency. The factor of 0.773 comes from the fact that oscillations can occur with frequencies in between the discrete bins (Leahy et al., 1983).

We applied Equation 2.8 to the powers that we detected in our search. We find that typical oscillations in 1 s intervals have $A = 5 - 20\%$, with the smaller fractional amplitudes observed during the brighter portions of the bursts. We note that larger A are sometimes observed for a fraction of a second during the rises of bursts (e.g Strohmayer et al., 1997a), but that the 1 s transforms we used are not sensitive to these rapidly declining signals.

We used the same technique to search for signals at one-half, three-halves, and twice the oscillation frequency in Table 2.1. We use $P_{\mathrm{th}} = 27.7$ to take into account that we are searching four 10 Hz frequency intervals (including that of the fundamental frequency). We find no significant signals at these half-integer multiples of the fundamental. To compute upper limits on fractional amplitudes of any signal powers, we must take into account the fact that the noise can add destructively with any signal that may be present in the data (Groth, 1975). We used the algorithm in the Appendix of Vaughan et al. (1994) to calculate

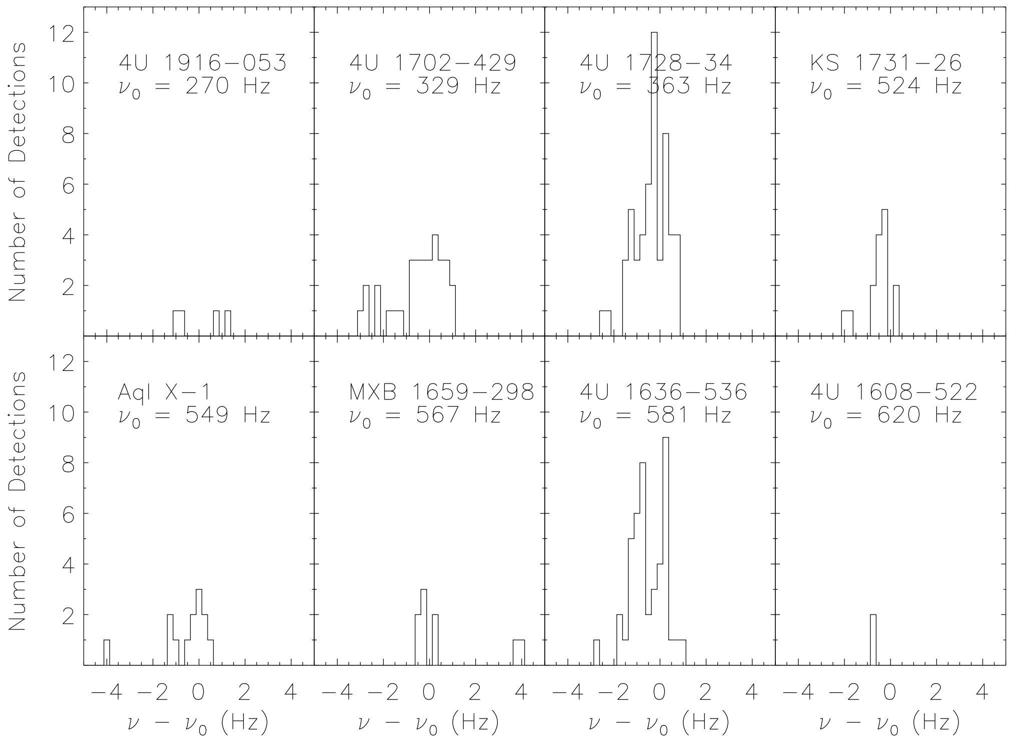

Figure 2-2 Histograms of the number of oscillations detected at each frequency within a 10 Hz range of the mean indicated during the first 16 s of each burst, separated by source. Detections are defined as having a single-trial probability of less than 2×10^{-5} that they are due to noise. The histograms are generally narrowly distributed with an absolute width of about 4 Hz, and appear to have definite upper limits. However, the signal at 571 Hz in MXB 1659−298 has a chance probability of 3×10^{-4} given that we searched 159 bursts from all sources to produce the histograms.

95% upper limits to P, and then Equation 2.8 to compute upper limits on A_n at multiples $n = 0.5$, 1.5, or 2 times the main frequency. We find that $A_n < 5\%$ during the brightest portions of bursts, while we can only place limits of $A_n < 50\%$ in the rise of the burst.

2.2.2 Frequency Range of Oscillations

Burst oscillations often drift in frequency by 1–2 Hz during the course of an individual burst (Figure 1-7). In order to establish the range of frequencies over which the oscillations are observed, and in particular whether there are strict upper limits to their frequencies, we produced a histogram of the distribution of observed frequencies detected in our search (Figure 2-2). For the majority of sources, the histograms are narrowly distributed with a width of 2-4 Hz, significantly smaller than the 10 Hz search window. This corresponds to frequency drifts ranging from 0.4% (KS 1731−260) to 1.2% (4U 1702−429).

The distribution from 4U 1636−536 appears to be double-peaked, possibly owing to two effects. First, oscillations are usually observed from this source only in the rise and tail, and the frequency gap between the two peaks could result from the fact that we do not observe

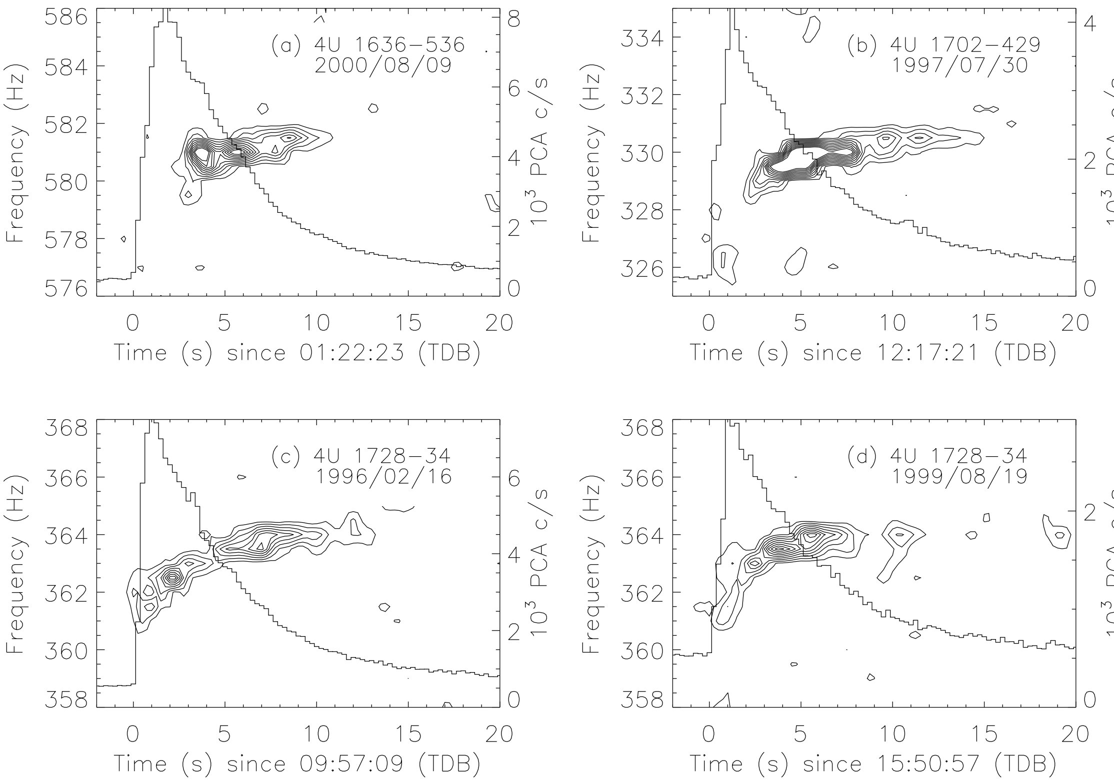

Figure 2-3 Dynamic power spectra, in which we plot contours of power as a function of time and frequency. The PCA count rate showing the burst profile is also plotted referenced to the right axis. We computed power spectra of overlapping 2 s intervals of data every 0.25 s. A Welsh window (Press et al., 1992) was applied to suppress spurious signals from the binning of the data. The contour levels are at powers of 0.02 in single-trial probability starting at a chance occurrence of 0.02. In all of these cases, the frequencies of the oscillations evolve by 1–2 Hz, increasing quickly at first, but saturating at a stable value after about 5 s.

the intermediate frequencies as the oscillations evolve (see Section 4.2.1). However, two oscillations are present simultaneously in several bursts from this source (see Section 2.2.3 and Miller 2000), which could indicate there are indeed two fundamental frequencies.

One detected oscillation is unusual given the distributions in Figure 2-2, and has already been noted by Wijnands, Strohmayer, & Franco (2000). It is detected in MXB 1659−298 about 4 Hz above the next highest frequency, with a probability of 4×10^{-4} that it is due to noise given all of the trial frequencies searched. The oscillation occurs at 571 Hz in a single interval about 15 s into the tail of a burst, while the oscillation detected earlier in the burst seemed to disappear about 5 s into the burst after reaching an asymptotic frequency of 567 Hz. If this signal is a "burst oscillation", it calls into question whether we are observing frequency saturation at all.

2.2.3 Characterization of the Frequency Evolution

We also searched the power spectra to confirm that the oscillations in our sample drift upward in frequency during the course of the burst, saturating at an approximately constant frequency late in the tail. The frequency evolution is most easily visualized by computing power spectra of short intervals of data that overlap in time and plotting contours of power as a function of both time and frequency. Figure 2-3 illustrates such dynamic power spectra of several burst oscillations. In each case, the frequencies of the oscillations increase rapidly at the starts of the bursts, then appear to saturate at relatively stable values within about 5 s, as the bursts decay.

This trend occurs in most bursts. However, there are a few exceptions that have been noted in the literature, such as (*i*) clear evidence for a frequency *decrease* several seconds after the burst is first detected (spin-down; Figure 2-4) and (*ii*) signals present at two frequencies simultaneously (Figure 2-5). Spin-down episodes and simultaneous signals are not common.

We find only 3 clear examples of spin-down episodes during bursts, which we display in Figure 2-4. Two of these have been reported previously, from 4U 1636−536 (Strohmayer, 1999) and KS 1731−260 (Muno et al., 2000), and we find one additional example from 4U 1728−34. In all cases, the frequency decrease is on order 1 Hz. There is no clear pattern as to when in the burst the spin-down occurs. In KS 1731−260, the event occurs in the peak of the burst, while in 4U 1728−34 and 4U 1636−536 the spin-down occurs as the burst decays.

We also find two clear examples of bursts in which two signals are detected simultaneously at frequencies separated by about 1 Hz. The most significant example has already been reported by Miller (2000) from 4U 1636−536, and we find a second example in 4U 1702−429. Both are displayed in Figure 2-5. The second oscillation in 4U 1636−536 occurs between 2–3 s into the burst, and has a chance probability $< 3 \times 10^{-10}$ of occurring randomly due to noise (see also Miller, 2000). The second signal from 4U 1728−34 occurs 11 s into the burst, and is only marginally significant, with a single-trial chance probability of 5×10^{-5}. Less significant examples, with chance probabilities of ~ 0.01, have also been reported in two more bursts from 4U 1636−536 by Miller (2000), and in one burst from 4U 1916−053 by Galloway et al. (2001). In all cases, the secondary frequencies are 1–3 Hz lower than the main signal.

2.3 Summary

We have detected 68 oscillations in a search of 159 bursts from 8 neutron star LMXBS. The fractional rms amplitudes of the oscillations range from 5–20%, in power spectra of 1 s intervals from the bursts. No signals are evident in 1 s intervals at 0.5, 1.5, or 2 times the main frequency. Upper limits on their amplitudes are as low as 5% during the brightest portions of bursts.

The frequencies of the oscillations drift by up to 1.2% (Figure 2-2), but generally reach a stable value on the time scales of seconds. Both spin-down in the oscillation train and obvious examples of simultaneous signals separated by around 1 Hz are relatively rare, occurring in 3 and 2 bursts out of 65 respectively. Therefore, the general picture of the frequency evolution of burst oscillations developed from smaller studies of oscillations is supported by the large sample we have investigated.

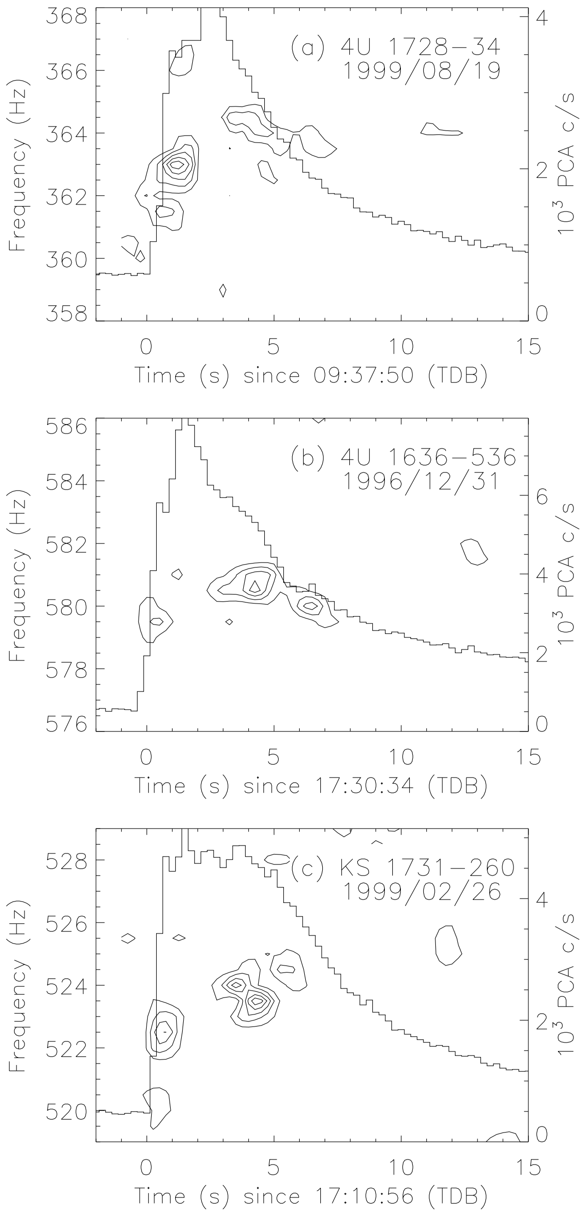

Figure 2-4 Same as Figure 2-3, for the 3 oscillations that exhibited spin-down episodes out of our sample of 68 pulsations. The frequency drift is on order 1 Hz in each case. There appears to be no trend as to when in the burst spin-down occurs.

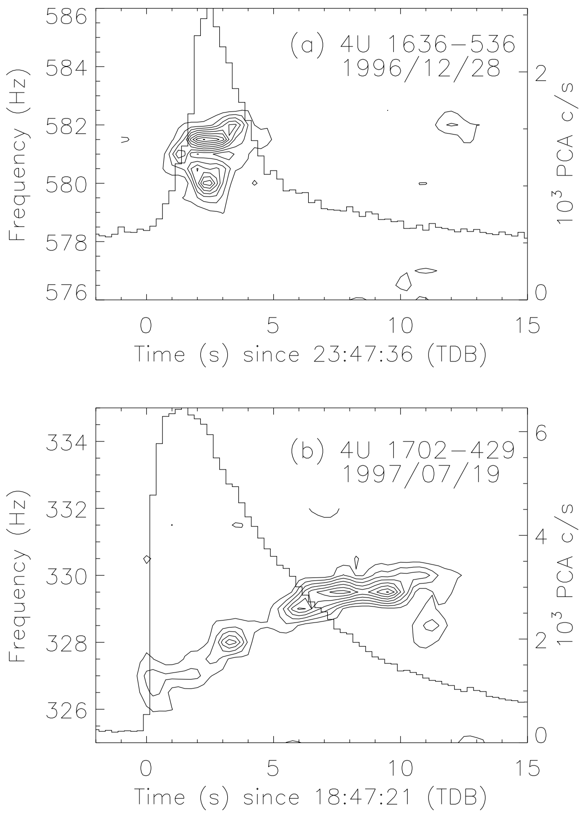

Figure 2-5 Same as Figure 2-3, for oscillations that exhibited two simultaneous signals separated in frequency by ~ 1 Hz. The secondary signal occurs at 2–3 s in panel a, with a chance probability that it is due to noise of 3×10^{-10}. The second signal at 11 s in panel b has a chance probability of 5×10^{-5}. It may not look spectacular, but it is definitely there.

Chapter 3

Evolution of the Oscillation Frequencies

> This chapter is adapted from the paper "The Frequency Stability of Millisecond Oscillations during Thermonuclear X-Ray Bursts" by Michael P. Muno, Duncan K. Galloway, Deepto Chakrabarty, and Dimitrios Psaltis, which has been submitted to *The Astrophysical Journal.*

The fact that the frequencies of the burst oscillations evolve as a function of time complicates investigations into other aspects of the oscillations. However, the frequency drift is quite likely to be sensitive to the temperature, density, and composition of the surface layers of the neutron stars, and thus serve as a probe of their properties. Therefore, in this chapter we derive mathematical models of the observed frequency evolution. This allows us to quantify the intrinsic coherence and stability of the mechanism that produces the oscillations. The models also then are used in Chapter 4 to compare the properties of the oscillations and the bursts, and in Chapter 5 to derive folded profiles of the oscillations.

3.1 Analysis of the Frequency Evolution

In order to examine in detail whether the oscillations are coherent and drift to stable asymptotic frequencies, we developed frequency models using a phase connection technique commonly applied in pulsar timing studies (Manchester & Taylor, 1977; Deeter et al., 1981). A brief summary of the procedure is as follows: we fold the data in 0.25–0.5 s intervals according to a trial frequency model (which is the derivative of a phase model), and compute a Fourier transform of the resulting profile. If the power in the fundamental frequency of the pulsation[1] has less than a 10% chance of occurring randomly due to noise ($P > 4.6$ in the normalization of Leahy et al. 1983), we measure the phase by a linear least squares fit of a sine function to the profile. The measured phase residuals $\phi_{\rm obs}(t_i)$ are then related to the predicted phases $\phi_{\rm model}(t_i)$ by

$$\Delta\phi(t_i) \equiv \phi_{\rm obs}(t_i) - \phi_{\rm model}(t_i). \tag{3.1}$$

[1]We have confirmed that all of the profiles were consistent with sinusoidal signals, justifying the use of only the power at the fundamental frequency.

In the above convention, an increasing phase residual indicates that the instantaneous trial frequency ($d\phi_{\rm model}/dt_i$) is too low.

The phase residuals $\Delta\phi(t_i)$ are then modeled via a least squares minimization, using a χ^2 statistic calculated from the phase residuals:

$$\chi^2 = \sum \frac{(\Delta\phi(t_i))^2}{(\sigma_{\Delta\phi})^2}. \tag{3.2}$$

Here, $\sigma_{\Delta\phi}$ is the uncertainty on the phase measured from the folded profile, which can easily be determined from the diagonal values of the covariance matrix in the linear least squares fit (Press et al., 1992). We have confirmed that these uncertainties are accurate via Monte Carlo simulations, in which we (*i*) perturbed the counts in each bin of the profile within the range expected from Poisson counting noise and (*ii*) recorded the uncertainty as the standard deviation of phase measurements of 100 perturbed profiles. We also verified the values for $\sigma_{\Delta\phi}$ by visual inspection.

The phase connection technique provides a correction $d(\Delta\phi)/dt$ to the original frequency model $\nu_{\rm model}$, so that the best-fit frequency is

$$\nu(t) = \nu_{\rm model}(t) + \frac{d}{dt}(\Delta\phi) \tag{3.3}$$

This procedure can be iterated using the new frequency model, if it is composed of linear functions.

The advantages of this method are (*i*) that the form of the observed phase residuals naturally suggests the best model for the frequency evolution and provides a quantitative test of how well the trial phase evolution matches the data, (*ii*) there are widely accepted techniques to calculate the uncertainties on the model for the frequency evolution from the least squares fit to the phases, and (*iii*) that the method utilizes the phase information that the power spectrum discards, which allows much finer frequency resolution on short time scales. In contrast, the Z^2 method of Strohmayer & Markwardt (1999) distinguishes between models based upon the amount of power in the folded profile, but provides little information about how the frequency of an oscillation deviates from the model assumed. The Z^2 statistic is still very useful for examining the amplitude and phase evolution of the oscillations on short (less than 0.1 s) time scales after the frequency evolution is modeled.

Figure 3-1a illustrates the importance of considering the phases in modeling the frequency evolution. Judging from power spectra alone, the frequency of this oscillation from 4U 1636−536 appears roughly constant (*top panel*). However, when one examines the phase residuals from a constant frequency model it is clear that additional evolution has occurred (*center panel*). An acceptable fit to the frequency evolution only can be achieved using a fifth order polynomial (*bottom panel*). Although some of this frequency evolution can be inferred from the power spectra alone (see also Miller, 2000), by tracking the phase we are able to achieve high frequency resolution and to determine how coherent the oscillations are.

3.1.1 Models for the Phase Evolution

We used data with 2^{-13} s time resolution in a single energy channel (2–60 keV) to study the frequency evolution. Searching in restricted energy bands can sometimes allow one to detect oscillation trains for a second or two longer (e.g. Giles et al., 2002), but in many cases

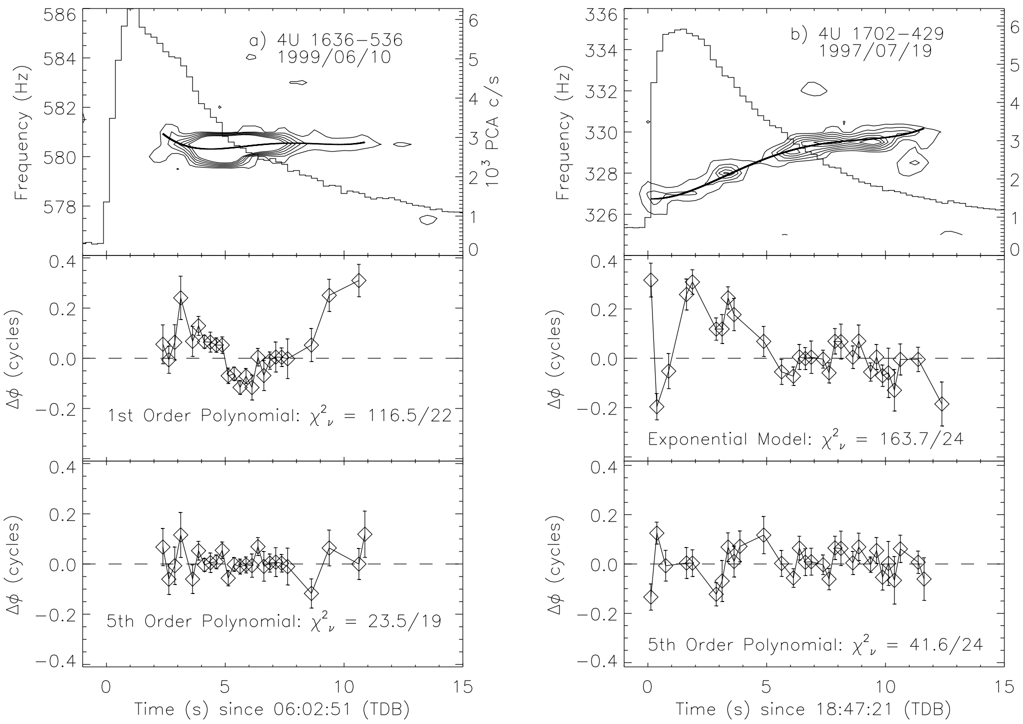

Figure 3-1 The frequency and phase evolution of burst oscillations from (a) 4U 1636−536 and (b) 4U 1702−429. The figures demonstrate how the phase connection method allows one to distinguish between models for the frequency evolution. *Top panel:* Same as Figure 2-3. The solid line at the center of the contours is the best-fit frequency evolution. *Center and bottom panels:* The phase residuals after folding a the data about the model for the frequency evolution indicated. The bottom panel is the best-fit, as indicated by the lower value of χ^2_ν.

Table 3.1. Models for the Phase Evolution of Burst Oscillations

Best Model	Number of Trains
1st Order	9
2nd Order	13
3rd Order	18
4th Order	3
5th Order	10
Exponential	6

these modes have gaps due to the limited size of the data buffer that offset the more efficient detections. We modeled the phase evolution of the oscillations both using polynomial models (up to fifth order) and using a saturating exponential such that the frequency evolution is of the form used by Strohmayer & Markwardt (1999):

$$\nu(t) = \nu_0 - \Delta\nu \exp(-t/\tau), \tag{3.4}$$

where ν_0 is the asymptotic frequency of the oscillation, $\Delta\nu$ is the frequency drift referenced to the start of the burst, and τ is the time scale for the frequency drift. When modeling the data with polynomials, we iterated the procedure until no improvement in the fit to the phase residuals was found. The fits using the exponential model were executed on phase residuals found assuming a constant trial frequency, as a linear basis function is required for the iterative process. Table 3.1 lists the number of oscillation trains best fit with each model, as determined from the value of reduced χ^2. If the reduced χ^2 was greater than one, and if both the number of degrees of freedom and the value of χ^2 decreased in comparing one model to another, an F-test (Bevington, 1969) was used to ensure that the decrease in χ^2 had less than a 5% chance of being random.

We modeled all oscillations that lasted continuously for more than 2 s, for a total of 59 oscillations from 6 different sources. Thirty-seven oscillations required either an exponential model or a polynomial of third degree or higher. Exponential models are only favored over polynomials in only 6 out of 37 cases. The exponential models are formally inconsistent (greater than 99% confidence) in 22 of the remaining 31 cases, while all such frequency models are inconsistent with the data in 12 out of 37 cases.

The polynomial models generally reproduce the frequency evolution better than exponential models because there is slower frequency evolution at the start of the oscillation train, inflection in the evolution during the train, or a decrease in the oscillation frequency as the trains disappear (see also Miller, 2000). Figure 3-1 exhibits all of these variations in the frequency evolution. In addition to the upward drift in frequency that saturates after a few seconds, the frequency also tends to wander by about 0.1 Hz in a manner that is not systematic.

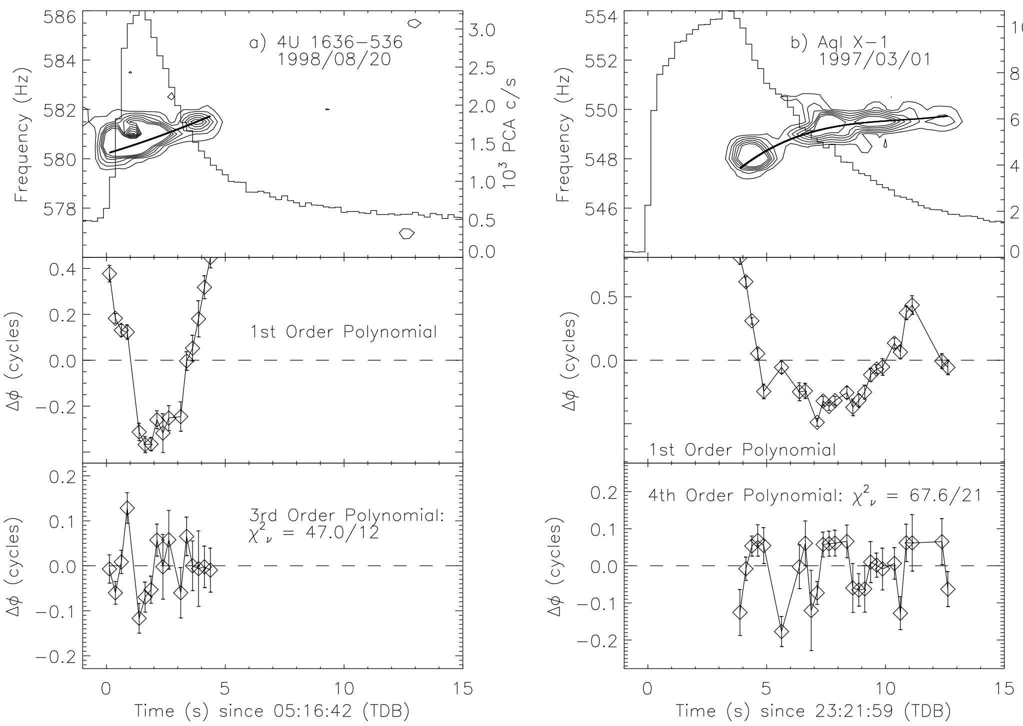

Figure 3-2 The frequency and phase evolution of oscillations from two trains for which the best-fit model was statistically inconsistent with the data. The axes are as in Figure 3-1.

3.1.2 Short-term Stability of the Burst Oscillations

Our inability to model 30% of the oscillations with smooth frequency evolution could indicate that the underlying mechanism is not perfectly stable. We tried higher-order polynomials in instances where our best-fit model is statistically unacceptable, but we find that we achieve only marginal improvements in the chi-squared statistic. Higher-order polynomials can smooth residuals in the middle of the oscillation train, but tend to create larger residuals at the endpoints. Figure 3-2 illustrates two examples of oscillation trains that we were unable to fit with exponential or polynomial models. Piecewise smooth phase functions would provide better fits in some instances, such as between 2–4 s in Figure 3-2a, and 3–6 s in Figure 3-2b. However, the resulting discontinuity in the derivative of the phase implies that the frequency of the oscillation shifts by ~ 0.25 Hz in less than 0.25 s.

Moreover, some of the residuals appear to be discrete changes in the phases of the oscillations. One possible explanation for the phase residuals in the first 1–2 s of Figure 3-2a is that two signals are present simultaneously within about 1 Hz, the resolution of the folding technique. Simultaneous signals with only slightly larger frequency separations have been seen in other bursts from 4U 1636−536 (Miller, 2000). In Figure 3-2b, there appear to be discrete jumps of about 0.1 cycle in the phase of the oscillation from 7–10 s into the burst, similar to that observed by Strohmayer (2001) during an oscillation in the rise of a burst from 4U 1636−536. We confirmed that the sudden changes in the phases of the oscillations are not due to variations in the pulse profile, which is always sinusoidal. The presence of phase jumps suggests that the oscillations are not strictly coherent.

3.1.3 "Asymptotic" Frequencies of Burst Oscillations

Aside from the exceptions noted above and in Section 2.2.3, the fundamental features that led to the adoption of an exponential model for the frequency evolution by Strohmayer & Markwardt (1999) are present in about 70% of burst oscillations: the oscillations increase in frequency when they are first observed, but appear to reach stable frequencies on the time scale of seconds. Several authors have noted that the asymptotic frequencies of burst oscillations detected several years apart are remarkably similar (Strohmayer et al., 1998; Strohmayer & Markwardt, 1999). Therefore, we measured the maximum frequencies that the oscillations reached according to our best fit models, in order to determine whether the asymptotic frequencies of the oscillations are stable. The 1-σ uncertainties on the maximum frequency were found by a search through χ^2 space (e.g Lampton et al., 1976). We inflated the region of χ^2 space by the reduced χ^2 of the fit to account for those instances when the best available fit was statistically unacceptable. The maximum frequency was constrained to occur after a minimum, as in several cases the absolute highest frequency was observed at the start of the oscillation train (e.g Miller, 2000, and Figure 3-1a). Our measurements are consistent with those found using the Z^2 statistic by Strohmayer et al. (1998), Strohmayer & Markwardt (1999), and Giles et al. (2002). We compare our results for 4U 1636−536 with those of Giles et al. (2002) in Section 3.2.2.

In Figure 3-3, we plot how the maximum frequencies vary from burst-to-burst in each source. To indicate those oscillations where the frequency has apparently saturated, we have indicated which ones required at least an exponential or a 3rd order polynomial phase model by diamonds. The measurements taken from first or second order polynomial models are plotted only with error bars. The oscillations are stable to a few parts in 1000. We have calculated the fractional standard deviation in the maximum frequencies, $\sigma_\nu/\langle\nu_{\rm max}\rangle$,

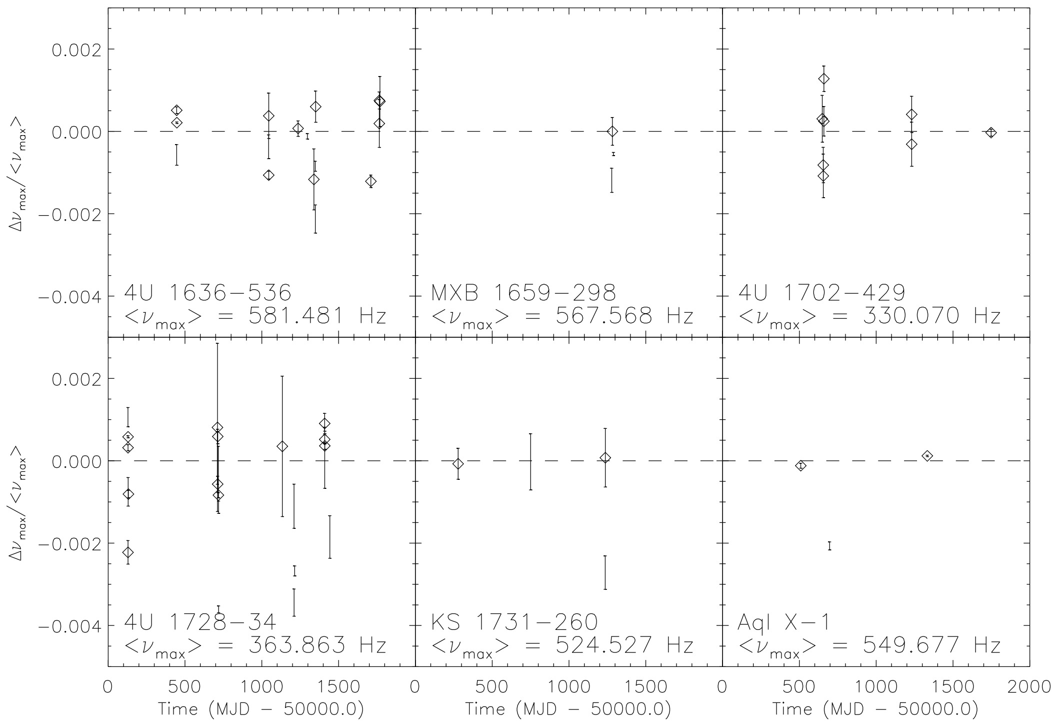

Figure 3-3 The maximum frequencies from the models summarized by Table 3.1 plotted as the fractional deviation from the mean as a function of time. Measurements from oscillation trains which appear to saturate, and are therefore more likely to be indicative of an asymptotic frequency, are marked with diamonds, while those which do not are simply reported with error bars.

Table 3.2. Dispersion in Maximal Frequencies of Burst Oscillations

Source	$\sigma_\nu/\langle\nu_{\rm max}\rangle$
4U 1636−536	7.7×10^{-4}
4U 1702−429	7.5×10^{-4}
4U 1728−34	9.2×10^{-4}
KS 1731−260[a]	7.3×10^{-5}
Aql X-1[a]	1.2×10^{-4}

Note. — σ_ν is defined as the standard deviation of the maximum frequencies measured in oscillations that appear to saturate, unless otherwise indicated.

[a]Only two maximum frequencies were measured, so σ_ν is the difference between the values.

for those sources with more than two values, and listed them in Table 3.2. For Aql X-1 and KS 1731−260, the frequency evolution appears to saturate during two bursts each, so we report the fractional difference between the measurements. The deviations in these frequencies $\sigma_\nu/\langle\nu_{\rm max}\rangle$ are quite small, less than one part in 1000.

3.2 The Stability of Oscillations

The frequency evolution of burst oscillations can be described by smooth phase models in all but 30% of the trains that we have studied (Section 2.5; see also Strohmayer 2001). These discrepancies appear as jumps in the phase or its derivative in Figure 3-2. If the oscillations result from brightness asymmetries on the surface of the neutron star, it appears that some of the following occur: (*i*) there are multiple anisotropies or modes that propagate with slightly different velocities relative to the surface, which results in two simultaneous signals that interfere with each other (see also Section 2.2), (*ii*) the velocity of the pattern changes suddenly on time scales of 0.25 s, or (*iii*) the anisotropies change their longitude in less than a tenth of a second, resulting in sudden phase jumps of about 0.1 cycles.

On time scales of years, the oscillations are stable to a few parts in 1000. This is consistent with the Doppler shifts that are expected from the binary orbit, which raises the possibility of measuring a mass function for the companion star. We now examine this frequency dispersion in detail.

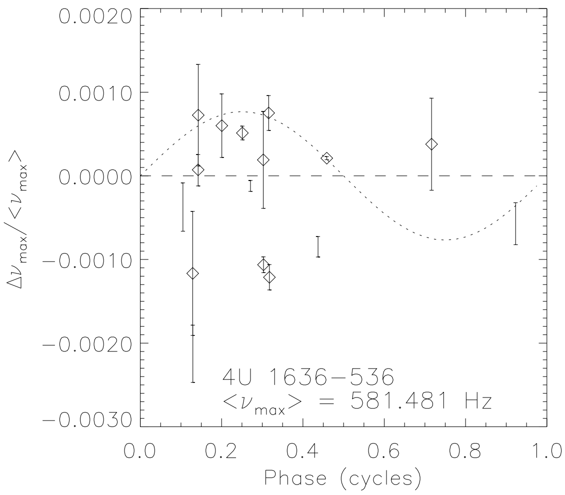

Figure 3-4 The fractional deviation of the maximum frequencies from Table 1 are plotted as a function of orbital phase for 4U 1636−536. The dotted line indicates the expected orbital modulation using the ephemeris of Giles et al. (2002): 2446667.3183(26) + $N \times$ 0.15804669(24) (HJD). The dispersion in asymptotic frequencies can not be explained by orbital motion alone.

3.2.1 Dispersion in the Maximum Frequencies

The change in the apparent spin frequency due to the orbital motion of the neutron star is given by

$$\frac{\Delta\nu_{\max}}{\langle\nu_{\max}\rangle} = 2.0 \times 10^{-3}\frac{M_c \sin i}{P_{hr}^{1/3}(M_x + M_c)^{2/3}}, \tag{3.5}$$

where M_x and M_c are the mass of the neutron star and companion respectively in solar units, P_{hr} is the binary orbital period in hours, and i is the inclination of the orbital plane. Assuming a star with solar density, its mass is $M_c \sim 0.11 P_{\rm hr}$ if it over-fills its Roche lobe (Frank et al., 1995). For $P_{hr} = 5$, $\sin(i) = 0.87$, $M_x = 1.4$, and $M_c = 0.5$, the half-amplitude of the Doppler variation would be $\Delta\nu_{\max}/\langle\nu_{\max}\rangle = 4 \times 10^{-4}$. This is a factor of 2–5 smaller than the dispersions from 4U 1636−536, 4U 1702−429, and 4U 1728−34 (Figure 3-3), but it is of the right order of magnitude.

Three oscillation sources have known orbital ephemerides: MXB 1659−298 (Wachter et al., 2000), Aql X-1 (Welsh et al., 2000), and 4U 1636−536 (Giles et al., 2002). We did not measure enough oscillations from MXB 1659−298 and Aql X-1 to constrain the parameters of the binary orbit. We have measured eleven oscillations that appear to saturate from 4U 1636−536 (the diamonds in Figure 3-3), so we have attempted to fit a sinusoid to the maximum frequencies as a function of orbital phase (Figure 3-4). The best-fit sinusoid, allowing the reference phase to vary, has a χ^2 of 221 for 8 degrees of freedom. Therefore, sinusoidal orbital modulations cannot cause all of the observed dispersion. In Figure 3-4 we have chosen to plot a sinusoid with an amplitude equal to the standard deviation of the points fit, $\sigma_\nu/\langle\nu_{\max}\rangle = 7.7 \times 10^{-4}$. The disagreement between the data and the sinusoid is primarily due to three oscillations with low maximum frequencies. Two of these lasted for more than 5 s, one of which is displayed in the right panel of Figure 3-1 (1999 June 10

06:03). We will discuss this further in the next section.

There are no other effects that ordinarily change the apparent spin frequency of neutron stars (i.e. pulsars) that can produce the dispersion in Figures 3-3 and 3-4. Accretion torques can alternately quicken or slow the rotation of the neutron star, and would provide the next largest effect (Frank et al., 1995). The torque on a neutron star can be estimated by assuming that its magnetic field disrupts the disk at some fiducial radius R_M and removes all of its angular momentum. At R_M, we have $I\dot{\Omega} = \dot{M}(GMR_M)^{1/2}$. We take R_M to be the co-rotation radius, where $2\pi\nu_{\rm kHz} = (GM/R_m^3)^{1/2}$, so that

$$\dot{\nu} = 7 \times 10^{-5} \dot{M} R_{10\rm km} M_x^{2/3} I_{45}^{-1} \nu_{\rm kHz}^{-1/3} \text{Hz yr}^{-1} \tag{3.6}$$

where $\dot{M}$ is the accretion rate in Eddington units, $R_{10\rm km}$ is the radius of the neutron star in units of 10 km, M_x is its mass in solar units, I_{45} is its moment of inertia in units of 10^{45} g cm^2, and $\nu_{\rm kHz}$ is the stellar spin frequency in kHz. The values are scaled to those expected for a burster. For a spin frequency of 200 Hz, Equation 3.6 corresponds to $\Delta\nu_{\rm max}/\langle\nu_{\rm max}\rangle \approx 6 \times 10^{-7}$ in one year. Clearly, the observed dispersion in the maximum frequencies on time scales of a month (Figure 3-3) is much larger than can be explained by accretion torques (Equation 3.6).

3.2.2 Frequency Dispersion in 4U 1636−536

Giles et al. (2002) recently examined a larger sample of oscillations from 4U 1636−536, and found that there is a subset of the burst oscillations whose maximum frequencies are distributed as a Gaussian about 581.64 Hz with a width of 0.08 Hz. We cannot independently test this, as the uncertainties that we report on the maximum frequencies are up to a factor of 5 larger than those in Giles et al. (2002). This is because the phase-connection technique we used to measure the maximum frequencies takes into account the frequency evolution of the oscillations, while the dynamic Z^2 technique Giles et al. (2002) used assumes that the frequency is constant during each 2 s interval that they test. As a result, the magnitude of our uncertainties (0.05–0.4 Hz) are often larger than the width of the Gaussian of Giles et al. (2002).[2]

If we only include those oscillations that are part of the Gaussian in Giles et al. (2002), we find that our data are consistent with no modulation. Fitting a sinusoid to the data, we derive a fractional amplitude of $(5.0 \pm 2.1) \times 10^{-4}$ ($\chi^2 = 6.7$ for 5 degrees of freedom). This is equivalent to a Doppler shift of 150±63 km s^{-1}, which is significantly larger than the 90% upper limit to the velocity from Giles et al. (2001; 55 km s^{-1}). The uncertainties that we assumed result in the larger upper limit on the velocity. These systematic uncertainties also present an additional hurdle in measuring the orbital motion of the neutron star.

3.2.3 Mechanisms for the Frequency Evolution

Three models have been proposed to explain the frequency evolution of the burst oscillations, all of which assume that anisotropies develop in the surface brightness of the neutron star

[2]On the other hand, we may be over-estimating our uncertainties when we model the oscillations with higher-order polynomials, which tend to have large derivatives at their endpoints. A more physical model might assume that the frequency change in the oscillations is much smaller at the endpoints. However, the oscillation that appears 4 Hz from the main signal at the end of the burst on 1999 Apr 14 from MXB 1659−298 (Wijnands et al., 2001) makes us reluctant to apply this assumption in our analysis, and leads us to assume our larger uncertainties.

(Strohmayer et al., 1997b; Cumming & Bildsten, 2000; Heyl, 2002; Spitkovsky et al., 2002). The simplest model was proposed by Strohmayer et al. (1997b), who suggested that the oscillations originate from hot regions on a burning layer that expands and decouples from the neutron star at the start of the burst. The oscillations are observed when the burning layer begins to contract, causing them to increase in frequency as the layer re-couples to the neutron star. However, recent calculations assuming that the burning layer is rigidly rotating predict a frequency drift a factor of three smaller than that observed (Cumming et al., 2002). Moreover, Cumming & Bildsten (2000) predicted that there should be a fractional dispersion of at most $\Delta\nu/\nu \approx 10^{-4}$ in the observed asymptotic frequencies, if the height of burning layer is smaller when it re-couples to the star than when it decouples. This is a factor of 10 smaller than the residual dispersion from 4U 1636−536 in Figure 3-4.

As a result, it is important to consider more complicated models for the frequency evolution of burst oscillations. Spitkovsky et al. (2002) have suggested that a brightness contrast could result from a hydrodynamical instability in a geostrophic flow, similar to Jupiter's Great Red Spot, while Heyl (2002) has proposed that Rossby waves propagating with retrograde motion on the neutron star could produce traveling brightness patterns on the stellar surface. The frequency evolution in both models is caused by changes in the velocity at which the pattern propagates around the star. The velocity in turn is sensitive to the temperature, density, and vertical structure of the surface layers. Thus, variations in the properties of the surface layers near the end of a burst can naturally explain the observed dispersion in the asymptotic frequencies of the oscillations (Figures 3-3 and 3-4). On short time scales, instabilities in either mechanism conceivably could cause the apparent phase jumps in Figure 3-2. Moreover, Heyl (2002) also has predicted that Rossby waves with different numbers of radial nodes could produce simultaneous signals at multiple frequencies, as are seen in rare cases (Section 2.2; compare Section 2.5). These models are promising, although how these mechanisms produce brightness variations on the stellar surface remains to be studied in detail.

3.3 Summary

We have examined 68 burst oscillations observed in 159 bursts from 8 different sources, and have modeled the frequency evolution of 59 oscillations from 6 sources (Table 3.1). In about 60% of the oscillation trains, the frequency evolution displays inflections that cannot be described by the standard exponential model. Two illustrative examples are shown in Figure 3-1. In addition to the upward frequency drift, the frequency tends to wander by on order 0.1 Hz in a manner that is not systematic.

The most notable result is that there appears to be slight instability in the mechanism generating the oscillations on time scales of both seconds and years. About 30% of the oscillation trains do not exhibit smooth phase and frequency evolution, as both low order polynomials and exponential models are statistically inconsistent with the data (Figure 3-2). The possible explanations are that (*i*) two signals may be present simultaneously, invalidating our assumption that there is a single signal in our analysis, (*ii*) there are discrete phase jumps that occur on time scales less than a second, and (*iii*) the frequencies of the oscillations shift dramatically on time scales of 0.25 s. On longer time scales, the maximum frequencies observed during these oscillation trains exhibit a fractional dispersion of $\Delta\nu_{\rm max}/\langle\nu_{\rm max}\rangle \leq 4 \times 10^{-3}$ (Figure 3-3). For 5 of the sources studied, this dispersion could be consistent with Doppler shifts of signals originating from rotating neutron stars as they orbit the centers of mass of their binaries. However, the dispersion in the maximum frequencies in 4U 1636−536 is uncorrelated with its known orbital period (Figure 3-4).

Several models have been proposed in which the oscillations originate from an anisotropy in the emission from the neutron star's surface. Each model the frequency evolution as originating from changes in the velocity of a pattern in the surface brightness (Strohmayer et al., 1997b; Cumming et al., 2002; Heyl, 2002; Spitkovsky et al., 2002). The apparent lack of stability in the underlying clock producing these oscillations favors the models in which the brightness asymmetry originates from hydrodynamic instabilities (Spitkovsky et al., 2002) or modes excited in the neutron star ocean (Heyl, 2002).

Chapter 4

Oscillations and the Underlying Bursts

> This chapter is adapted from sections of the papers "The Frequency Stability of Millisecond Oscillations during Thermonuclear X-Ray Bursts" by Michael P. Muno, Duncan K. Galloway, Deepto Chakrabarty, and Dimitrios Psaltis, and "The Amplitudes and Harmonic Content of Millisecond Oscillations During Thermonuclear X-ray Bursts" by Michael P. Muno, Feryal Özel, and Deepto Chakrabarty. Both of these have been submitted to *The Astrophysical Journal.*

With models for the frequency evolution, we can compare the properties of the oscillations and the bursts that underly them. Here, we determine how the properties of the bursts (*i*) affect our ability to observe oscillations, (*ii*) are correlated with the frequencies of the oscillations, and (*iii*) determine the fractional amplitudes of the oscillations. All of these aspects of the oscillations are sensitive to the structure of the surface layers on the neutron star. We quantify the properties of the bursts by measuring the energy spectra of their X-ray flux, from which we can derive a characteristic temperature, emitting solid angle, and bolometric flux. We also use the frequency models to derive the time scale and magnitude of the drift and the amplitudes of the oscillations as a function of time.

4.1 Spectral Analysis of Bursts

To measure the properties of the bursts, we integrated spectra for each 0.25 s interval during these bursts using combinations of the binned and event mode data for each observation. This provided at least 16 energy channels. The response of the detector to an input spectrum was determined using the FTOOL pcarsp. Since the effect of the X-ray burst on the spectrum of the persistent emission is unknown, it is not clear what "background" should be subtracted from the total received flux in order to obtain the true burst spectrum. As a trial case, we examined bursts from KS 1731$-$260 and estimated the background in two independent ways: (*i*) we used the FTOOL pcabackest to determine the instrumental and cosmic background, and assumed that the persistent flux disappears during the fit, and (*ii*) we used the spectrum of 15 s of data prior to the burst as background, subtracting

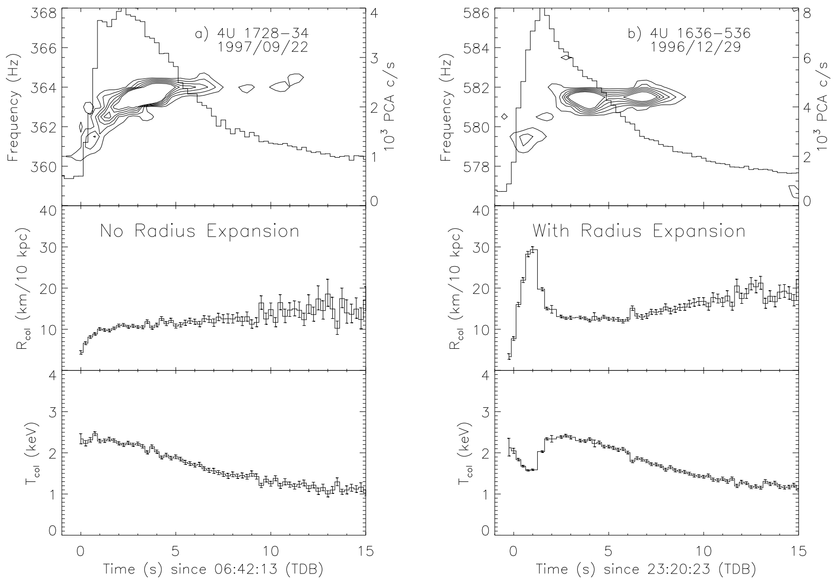

Figure 4-1 *Top Panels*: Same as Figure 2-3. *Center Panels*: The color radius derived from the spectral fits, as a function of time. *Bottom Panels*: The color temperature of the burst. Uncertainties are 1-σ. No radius expansion occurred during the burst on the left, and the oscillations were observed continuously for the first 7 s of the burst. The radius expansion on the right appears to interrupt the oscillations. Note that the power spectra are of 2 s intervals spaced every 0.25 s, while the energy spectra are computed in non-overlapping 0.25 s intervals.

the persistent emission under the assumption that it is unaffected by the burst.[1] We fit each spectrum between 2.5–20 keV in XSPEC with a model consisting of a blackbody multiplied by a constant interstellar absorption factor (determined from the mean value from fits assuming variable absorption). The model provides a color temperature ($T_{\rm col}$) and a normalization proportional to the square of the apparent radius of the burst emission surface ($R_{\rm col}$), and allows us to estimate the bolometric flux as a function of time.

We compared spectral fits for KS 1731−260 after subtracting the background in these two ways, and find that the resulting parameters are very similar, although using the pcabackest estimate of the background increases χ^2_ν for the fit by a factor of 1.3–1.6 relative to fits with the pre-burst emission subtracted. The increase in χ^2_ν is almost certainly due to the presence of flux from steady accretion that remains after subtracting the pcabackest estimate. Therefore, to keep the spectral model simple, we estimate the background as the 15 s of emission prior to each burst, and model the spectra from our sample of 8 sources as outlined above.

[1]We note that it is possible that persistent emission increases during the burst, with accretion induced by the burst itself, but we have no theoretical guidelines for modeling such a process and therefore ignore it.

4.2 Comparison of Burst and Oscillation Properties

4.2.1 How Radius Expansion Affects Oscillations

In many bursts, photospheric radius expansion is evident at the start of the burst, during which $R_{\rm col}$ increases and $T_{\rm col}$ decreases such that the bolometric flux remains constant, presumably at the Eddington limit (see Figure 4-1b and Lewin et al. 1993). We examined whether radius expansion episodes affect the times in the burst when the oscillations are observed. We find that of the 17 oscillation trains that are observed continuously throughout the rise, peak, and tail of bursts, all but one lack radius expansion episodes. Of the remaining 51 bursts where the oscillation train is not observed during the peak of the burst, 40 exhibit radius expansion. Since it also has been noticed previously that oscillations in KS 1731−260 (Smith et al., 1997) and MXB 1743−29 (Strohmayer et al., 1997b) appear only after the radius expansion episodes end, we conclude that radius expansion either obscures or interrupts the oscillations.

4.2.2 Magnitude and Time Scale of Frequency Drift

The phase models from the previous chapter allowed us to compare the frequency evolution to other properties of the bursts. We first measured the observed change in frequency $\Delta\nu$ for the continuous portion of each oscillation. We then measured the time scale τ that represents how long the oscillation took to evolve in frequency by $(1-e^{-1})\Delta\nu = 0.632\times\Delta\nu$ from the minimum observed frequency (compare Equation 3.4). As measures of the burst time scales, we have fit the decay in flux of each of these bursts with either one or two exponential functions ($\exp[-t/t_d]$). We also computed the peak bolometric flux and the fluence (total energy released) during each burst, using the exponential fit to determine the flux contribution at late times. We find that neither $\Delta\nu$ nor τ are correlated with any of these burst properties (not shown).

We have also compared $\Delta\nu$ and τ with the duration of the oscillations and the time at which they began. We find that τ is not correlated with the start time or duration of the oscillations (not shown). Instead, τ is distributed uniformly between 0.75–5.5 s. We plot the frequency drift $\Delta\nu$ as a function of these parameters in Figure 4-2. Oscillations that are first observed early in the burst evolve over a larger frequency range (*top panel*), but their frequency drift is not correlated with how long the oscillations last (*bottom panel*). This suggests that the evolution is initiated by the start of the burst.

Cummings & Bildsten (2000) previously noticed that the fractional frequency drifts $\Delta\nu/\nu$ in sources with ~600 Hz oscillations are a factor of two smaller than those in ~300 Hz oscillations. We have indicated the data from the faster (600 Hz) oscillations in Figure 4-2 with filled circles. The continuous portions of the fast oscillations tend to start later in the burst (with only two exceptions) and to drift by a smaller absolute frequency range. We believe that this is due to the fact that the faster oscillations tend to occur in bursts with radius expansion episodes (see Chapter 7), which prevents the oscillations from being observed earlier in the bursts (see Section 2.1). Indeed, when considering the non-continuous portions of the oscillations as well, the frequency histograms of the fast oscillators in Figure 2-2 do not in general have a narrower distribution. The fractional frequency drift is a factor of two smaller in the 600 Hz oscillators than in the 300 Hz ones, but only because the frequencies ν are larger.

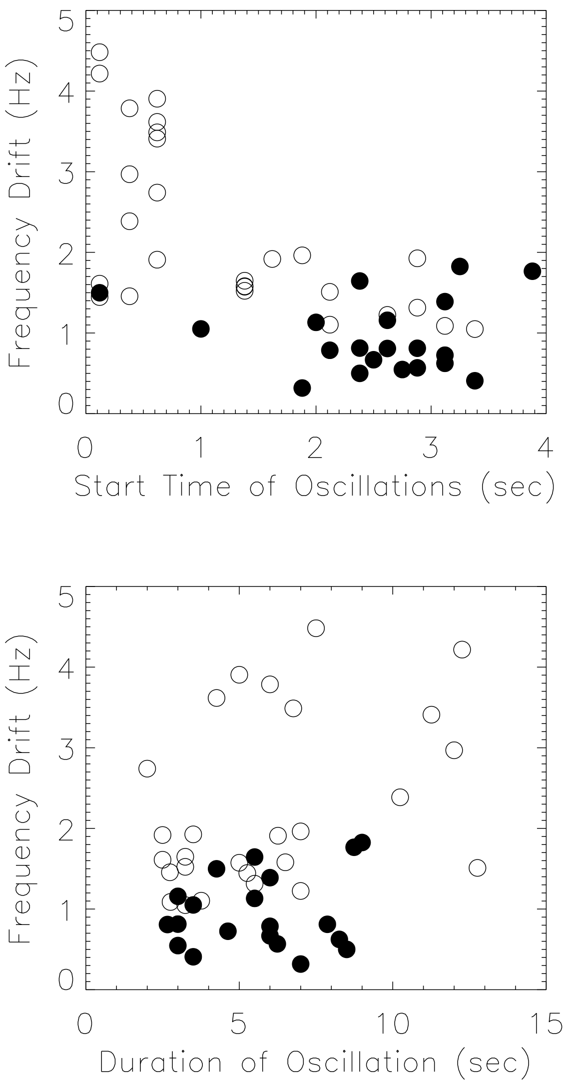

Figure 4-2 The total frequency drift in the continuous portion of the oscillation trains plotted as a function of the (*top panel*) the time at which the continuous oscillation train began, and (*bottom panel*) the duration of the continuous train. The total frequency drift is largest when the oscillations are first observed at the start of the bursts, but is not correlated with the duration of the oscillations. The solid circles are data from fast (600 Hz) oscillations, while the open circles are from slow (300 Hz).

4.2.3 Amplitude Evolution of the Oscillations

In order to examine how the amplitudes of the oscillations evolve as a function of time during each burst, we folded short intervals of data using the frequency models in Chapter 3. We compute Fourier power spectra of each interval, and use Equation 2.5 to define the fractional rms amplitude. Each interval contained a constant total number of counts from the burst emission, and therefore had an identical sensitivity to oscillations of a given fractional amplitude. We note that this renders our search insensitive to oscillations that have very large amplitudes in the rises of bursts, since the small count rates during these periods required us to use time bins that washed out the rapidly declining signals. In order to place upper limits on the amplitudes in those intervals when oscillations were not detected, we assumed that the frequency remained constant at the value we derived for the detection nearest in time. Upper limits and uncertainties on the amplitudes were calculated taking into account the distribution of noise powers in the spectra (Groth, 1975; Vaughan et al., 1994).

Of the 59 oscillations that we examined, 34 oscillations exhibited significant variations in their amplitudes that could be measured when folding the data in bins with constant count rate. The amplitudes of the rest of the oscillations did not vary significantly, and always remained just above the detection threshold (4–10% rms). Figure 4-3 displays six examples of oscillations (top panels) and their associated amplitude evolution (bottom panels) that are representative of our sample as a whole. In most cases, maxima in the fractional amplitudes occur as the flux from the burst decays. Figures 4-3a and b illustrate two bursts in which the largest amplitudes are observed 1–2 s after the flux from each burst begins to decline. This behavior is observed in 13 of the oscillation trains from our sample. In Figure 4-3c the largest fractional amplitude is observed much later in the burst, 8 s after the flux from the burst starts to decay. In 10 of the oscillations, peaks in the amplitudes are observed several seconds into the decays of the bursts. The oscillations in Figures 4-3d and e exhibit two separate and significant maxima in their amplitudes during the burst decays. In total, 3 oscillations exhibit this behavior; less significant secondary maxima may also be present in Figures 4-3b and f.

Strong oscillations are also observed in the rises and peaks of X-ray bursts, although less often. In Figure 4-3f, the amplitude of the oscillation is largest when the flux from the burst is highest, and declines steadily as the burst decays. Maxima are observed during the peaks of bursts in only 5 cases. This behavior is to be distinguished from instances where the amplitude declines *as the burst flux is rising* (e.g., Strohmayer et al., 1997a). We detect this latter behavior in only 6 cases, probably because the bins containing a constant number of counts are insensitive to oscillations with large fractional amplitudes that occur as the flux is rising. Of these 6, there are maxima in the amplitudes both in the rise and the peak in 1 case, and in both the rise and the decay in 2 cases.

In all of the examples in Figure 4-3, by 15 s into the burst, the fractional amplitudes of the oscillations drop suddenly below our detection threshold. Their disappearance is due to a genuine decrease in their amplitudes, as opposed to a lack of sensitivity when the flux from a burst is low. Besides this general trend, the amplitudes of the oscillations are not correlated with the underlying flux from the bursts.

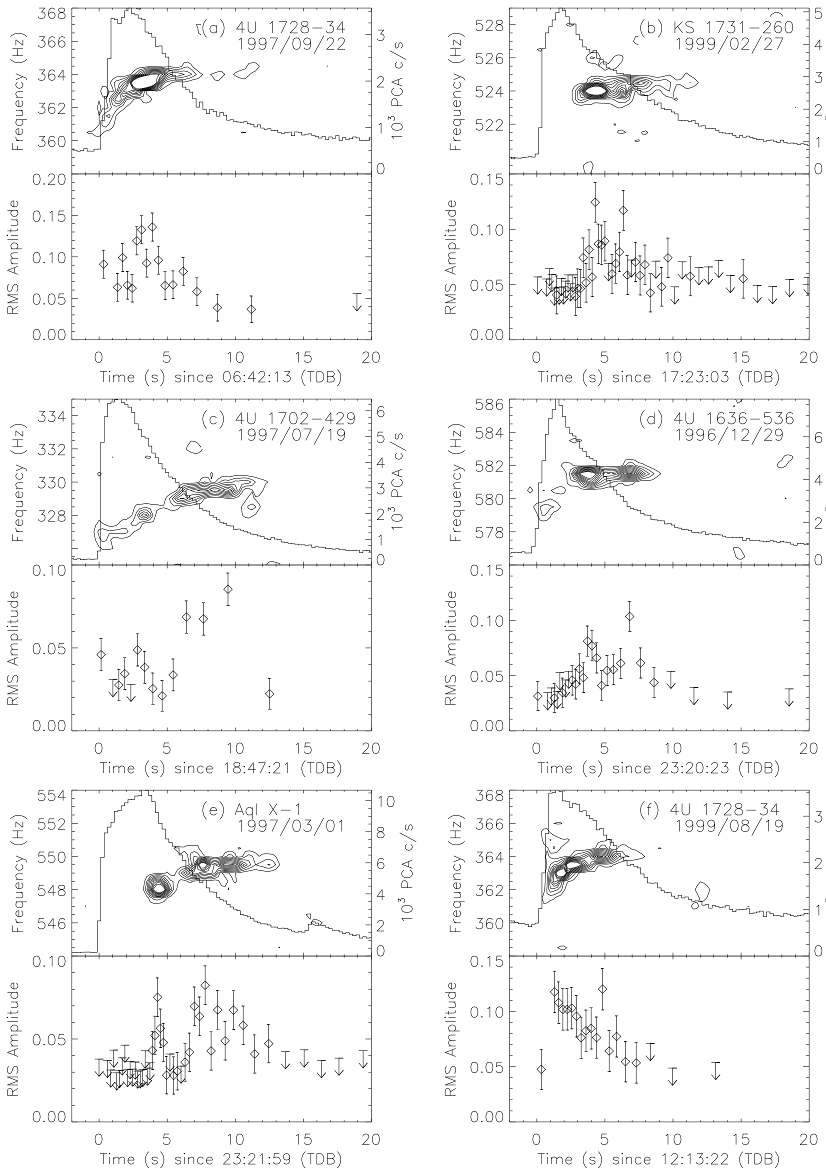

Figure 4-3 Six examples of oscillations during X-ray bursts. *Top Panels*: Same as Figure 2-3. *Bottom Panels*: The fractional rms amplitude of the oscillations as a function of time during the burst. The data were folded in intervals that contained a constant count rate, such that each interval is sensitive to oscillations of a constant fractional amplitude (between 4–10%). The amplitudes of the oscillations do not appear to be correlated with the amount of flux from the underlying burst.

4.3 Summary

We examined how the frequency and amplitudes of 59 burst oscillations are correlated with the properties of the underlying bursts. We find that:

1) Episodes of photospheric radius expansion appear to prevent us from observing oscillations. Of the 15 oscillation trains that appear continuously from the rise to the tail of the burst, all but 1 occur in bursts without radius expansion. When radius expansion does occur, oscillations are often seen in the rise and/or the tail of the burst, but rarely during the radius expansion episode.

2) The amount of the frequency drift appears larger when the oscillations are observed earlier in the burst (Figure 4-2). This suggests that the evolution is triggered by the start of the burst.

3) Aside from the above points, the time scale and magnitude of the frequency evolution does not appear to be correlated with other properties of the burst, such as its decay time scale, peak flux, or fluence.

4) The oscillations have rms amplitudes as high as 15% during the declines of bursts. Large intrinsic variations in the fractional amplitudes cause the oscillations to appear and disappear, but the maxima in the amplitudes are not related to the underlying flux in the bursts.

The lack of obvious connection between the bursts and oscillations is a bit disappointing, because it is expected the pulsations should be sensitive to the properties of the burning layer. Spectral changes in the burst atmosphere could mask true correlations (e.g. London et al., 1984). In KS 1731−260, very different spectral evolution is sometimes seen during the tails of different bursts (Chapter 6). At the same time, the oscillations may be more sensitive to the density and metallicity of the burning layer, which are harder to determine from the emission at the photosphere. More sophisticated models for the oscillations could direct a pointed search for correlations.

Chapter 5

Profiles of the Burst Oscillations

> This chapter is adapted from the paper "The Amplitudes and Harmonic Content of Millisecond Oscillations During Thermonuclear X-ray Bursts" by Michael P. Muno, Feryal Özel, and Deepto Chakrabarty, which has been submitted to *The Astrophysical Journal*.

One of the best means of discriminating between the various mechanisms for producing burst oscillations is the location and size of the brightness patterns that the models produce. These geometric parameters may be revealed in the profiles of the oscillations, possibly along with constraints on the physical parameters of the neutron star. In this chapter, we use the frequency models from Chapter 3 to derive folded profiles of the burst oscillations. We then compare the amplitudes and harmonic content of the oscillations to theoretical models of the emission from bright regions on a rotating neutron star.

5.1 Folded Profiles

We examined the profiles of each oscillation train by folding the data about the best-fit phase model of Chapter 3 (see Figure 5-1). The models used were low-order polynomials or exponential functions that reproduced the phase evolution well in 70% of the oscillations. In the remainder of the oscillation trains, there was evidence both for discrete phase jumps and for phase evolution that was only piecewise smooth. Additional power in principle could be recovered from these oscillations with more complicated frequency models, but we believe that the advantage would be small. For instance, we compared the powers we detected at the fundamental frequency to those obtained by Strohmayer & Markwardt (1999) for two oscillations that are common to both samples (bursts on 1997 Jul 26 and 30 from 4U 1702−429). Strohmayer & Markwardt (1999) used a Z^2 technique to determine the exponential frequency models that recovered the most power in the oscillations, while our technique determined that polynomial models best reproduced the phases of the oscillations. Nonetheless, we find that the values for the amplitudes of the oscillations are consistent within 1% fractional rms (see Figures 1 and 2 in Strohmayer & Markwardt, 1999). This is similar to the uncertainty in the oscillation power that is introduced by Poisson counting noise (Vaughan et al., 1994), indicating that slight modifications to the frequency models introduce only minor differences in the amplitudes derived for the oscillations.

To allow for the possibility that the strongest signal is observed at $2 \times \nu_{\rm spin}$, in practice we folded the data with a frequency one-half that predicted by the phase model. A typical

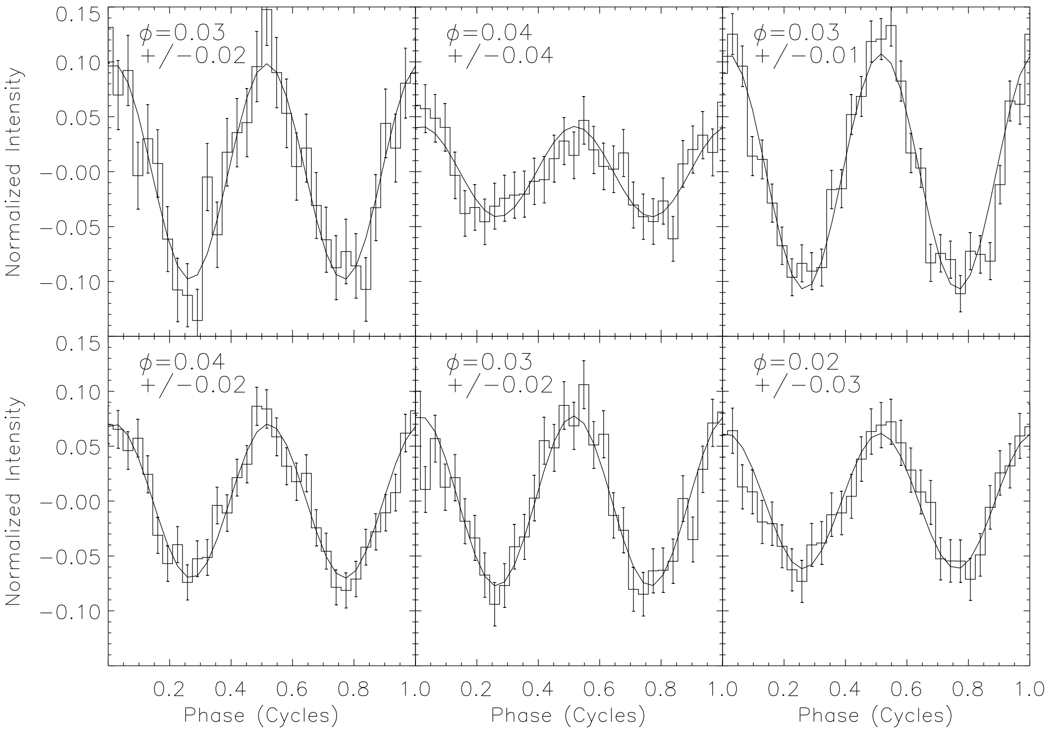

Figure 5-1 Profiles of six oscillations from 4U 1636−536 folded about one-half the best-fit phase model. The normalized instensity represents the fractional variation in the count rate. By construction, the phases of the profiles are all the same. All of the oscillations are consistent with sinusoids.

Table 5.1. Harmonic Amplitudes of Burst Oscillations

(1) Source	(2) ν_1	(3) No. Osc.	(4) Counts	(5) Background	(6) $A_{1/2}$	(7) A_1	(8) $A_{3/2}$	(9) A_2
4U 1636−536	581	17[a]	1.1×10^6	1.3×10^5	< 0.6	5.4(3)	< 0.5	< 0.3
MXB 1659−298	567	3	2.8×10^4	6.1×10^3	< 2.7	9.3(8)	< 2.8	< 2.7
Aql X-1	550	3	4.2×10^5	2.0×10^4	< 0.6	3.3(1)	< 0.5	< 0.5
KS 1731−260	521	4	2.5×10^5	4.5×10^4	< 1.2	4.7(2)	< 0.9	< 0.6
4U 1728−34	363	24[b]	1.6×10^6	2.3×10^5	< 0.6	5.5(1)	< 0.6	< 0.3
4U 1702−429	330	8	6.1×10^5	5.6×10^4	< 0.6	4.6(2)	< 0.7	< 0.7

Note. — Columns are as follows: (1) Source name. (2) The approximate frequency of the observed oscillations. (3) Number of bursts with oscillations used to make a combined profile. (4) Total number of counts in the profile, including background. (5) Estimated background counts in the profile. (6-9) Amplitudes or 95% upper limits on amplitudes at n =0.5,1,1.5, and 2 times the main frequency (ν_1).

[a]11 oscillations were used to constrain $A_{1/2}$ and $A_{3/2}$, for a total of 9.8×10^5 counts with 1.0×10^5 counts background.

[b]13 oscillations were used to constrain $A_{1/2}$ and $A_{3/2}$, for a total of 1.2×10^6 counts with 1.9×10^5 counts background.

oscillation train contains 6.8×10^4 photons. Since we modeled the phase evolution of each burst directly, the relative phases of each oscillation train were known, so we also produced summed profiles for each source. In searching for half-frequency signals, there is an uncertainty of one-half cycle between oscillations from different bursts, so we coherently added n oscillations in 2^{n-1} combinations to account for our lack of knowledge of the true phase. For 4U 1636−536 and 4U 1728−34, we only summed those profiles with more than 5×10^4 total counts in order to reduce slightly the number of profiles we examined.

We then computed the Fourier transform of (*i*) each of the 59 profiles individually and (*ii*) the sum of all profiles from each source, and searched for possible signals at 0.5, 1.0, 1.5, 2.0, 2.5 or 3.0 times the main oscillation frequencies. We considered a signal that had less than a 32% chance of occurring randomly in our entire search as a detection. We computed the fractional rms amplitudes of the oscillations from the power spectra according to Equation 2.5. Upper limits were computed taking into account the distribution of noise powers (Groth, 1975; Vaughan et al., 1994).

We find that the typical oscillation train has an rms amplitude of 5%. The most significant oscillation has a Leahy-normalized power (Leahy et al., 1983) of 615 in 10^5 counts from a burst from 4U 1636−536 on 2000 June 15, which translates to an 8% oscillation amplitude. Oscillations from the eclipsing source MXB 1659−298 have amplitudes of 10%, although the bursts are faint (10^4 photons in a typical folded profile).

The amplitudes from the summed profiles are listed in Table 5.1. The most significant signals are from 4U 1636−536 and 4U 1728−34, since we modeled 17 oscillation trains from 4U 1636−536 and 24 from 4U 1728−34. The summed waveform from 4U 1636−536 contains 1.0×10^6 photons and has a Leahy-normalized power of 2580. The profile from 4U 1728−34 contains 1.5×10^6 photons with a power of 2430. We find no evidence for signals at half-integer or integer multiples of the oscillation frequencies.[1] Typical individual

[1]In particular, we do not detect a signal at $A_{1/2}$ from 4U 1636−536. Miller (1999) has previously reported

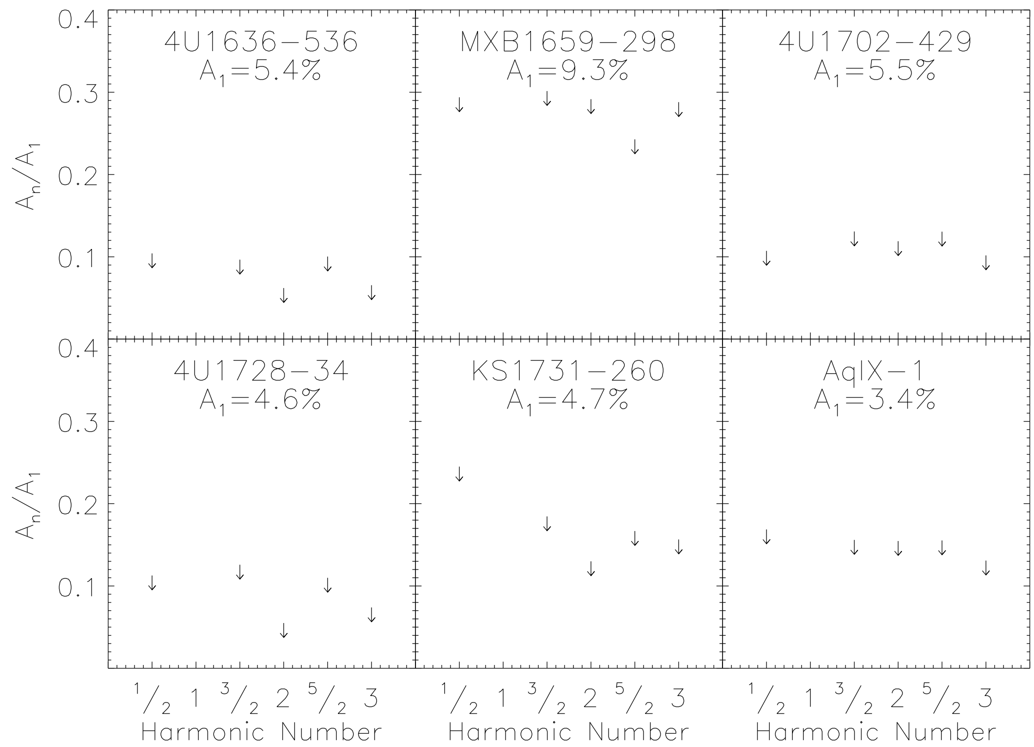

Figure 5-2 Upper limits (95% confidence) on the fractional amplitude of signals present at integer and half-integer multiples of the strongest signal (A_1), from combined pulse profiles using all of the oscillations in each source.

oscillations provide upper limits on the fractional rms amplitudes of harmonic signals (A_n) of 1.6% (95% confidence), but they can be as low as 0.7% in the brightest bursts from Aql X-1. Upper limits from the summed profiles range from 2.5% in MXB 1659−298, for which we examined oscillations in only three weak bursts, to 0.3–0.6% for 4U 1636−536 and 4U 1728−34, for which we combined oscillations from many bright bursts (Table 5.1). In Figure 5-2 we display the ratio of the upper limits on the amplitudes A_n to the amplitude of the largest signal A_1. The strongest constraints are again obtained for 4U 1728−34 and 4U 1636−536, for which any integer harmonic signal must be less than 5% of the amplitude of the detected signal, and any half-integer multiple of the main frequency must be less than 10% of the amplitude of the main signal.

We took care to establish that the harmonic content would not be reduced when producing a mean profile. We searched power spectra of short (1 s) intervals of data, and did not find evidence for signals at any multiples of the oscillation frequencies with amplitudes greater than 5–15% (Section 2.2.1). We also examined the folded profiles of the short intervals of data used in Section 4.2.3, and they are all consistent with sinusoidal signals to 5–10%. We concluded that there are no gross changes in the pulse profiles with time. From the theoretical standpoint, we used the simulations described in Section 5.2 below to

the detection of such a signal in combined profiles from the first 0.75 s of bursts from this source (see also Strohmayer, 2001).

confirm that the relative phases of the fundamental and harmonic signals do not vary as we change the parameters of a bright region on the neutron star surface (such as its location, temperature, and size). Although the amplitudes of harmonic signals may change, they can not add destructively, except in the special case where the region covers on average half of the neutron star. Therefore, the average profiles we measured accurately reflect the mean harmonic content of the oscillations, if they originate from a brightness asymmetry on a rotating neutron star.

5.2 Model Profiles

In order to interpret our observational results and to place constraints on theoretical models of burst oscillations, we calculated lightcurves from an anisotropic temperature distribution on the surface of a rapidly rotating neutron star using the techniques outlined by Pechenick et al. (1983), Braje et al. (2000), and Weinberg et al. (2001). We considered either a single circular polar cap or two antipodal caps (hereafter referred to as the $m = 1$ and $m = 2$ geometries) emitting with a uniform intensity to describe the temperature patterns on the stellar surface. We denoted the angular radius of the circular hot region(s) by ρ, and its (their) location by an angle α from the rotational axis of the neutron star. The angle between the line-of-sight of the observer and the spin axis of the neutron star was defined as β.

We assumed that the bright regions emit as blackbodies of a uniform temperature $T_{\rm col}$, and that the rest of the neutron star is dark. The latter choice will produce the largest amplitude oscillations; we confirmed that assuming the rest of the neutron star is warm decreases the amplitude of oscillations, but does not change the relative amplitude of the harmonics. The choice of a blackbody spectrum is reasonable for our purposes because the burst spectra can be adequately modeled as such in the PCA bandpass. In reality, however, both the spectra and the angular distribution of surface emission are affected by the neutron star atmosphere (e.g., London, Taam, & Howard 1984; Madej 1991). To roughly account for these effects, we adopted the Hopf function (approximately a $0.75(0.7 + \cos\delta)$ dependence; see Chandrasekhar, 1960, pp. 76–97) to describe the beaming of radiation emerging from the surface, because the atmosphere is scattering-dominated during a burst.

Photons were propagated from the neutron star to the observer through a Schwarzschild metric for an object with a compactness $p = Rc^2/2GM$. Since a 10 km neutron star spinning at 500 Hz has a surface velocity of 0.1c, we also computed time delay and Doppler effects assuming a neutron star spin frequency of Ω (details of the calculations are given in Appendix A). Although the Schwarzschild metric is not strictly correct for the spacetime exterior to a rotating neutron star, we utilized it because the exact metric for a neutron star depends on its unknown structure. The correction introduced by considering a Kerr metric instead, for example, is of order of a few percent (Braje et al., 2000). We neglected this effect in our calculations, since both the corrections from a metric appropriate for a rapidly-rotating neutron star and the measurement uncertainties in the observed waveforms are of the same magnitude.

For each set of parameters, we produced light curves in 40 phase bins, and in 64 energy bins logarithmically spaced between 0.01–25 keV. The observed spectrum is simply a sum of blackbodies whose temperatures are multiplied by Doppler factors; therefore, the signal from a bright region of arbitrary temperature could be obtained by rescaling from a calculation with $T = 1$ keV. For each phase, the resulting spectra were folded through a fiducial PCA response matrix, which we generated for Proportional Counter Unit 2 during December 1999 (gain epoch 3), in order to obtain predicted lightcurves that can be compared directly to the observations. To analyze these theoretical PCA lightcurves, we used the same Fourier technique that we applied to the observational data to measure the amplitude of the oscillation and its harmonics (Section 5.1).

5.2.1 The Amplitude of the Oscillations

In total, our simulations included eight parameters that can affect the amplitudes of the oscillations and their harmonics: the compactness and the spin frequency of the neutron star; the number, size, position, and temperature of the hot regions; the angular distribution of the emission from the hot region; and the viewing angle of the observer. We will focus on the compactness of the star, the geometric parameters of the hot spot, and the observer's line of sight in this section. We will briefly summarize the results for the other parameters. Similar studies have been carried out previously (Miller & Lamb, 1998; Weinberg et al., 2001; Özel, 2002). In the present work, we also take into account the response of the PCA, which allows us to compare the theoretical light curves directly to the properties of the oscillations. Including the PCA response increases the amplitude of the oscillations and their harmonics by a few percent (compare Miller & Lamb, 1998).

In Figure 5-3 we illustrate the effects of varying the compactness of the star p for a few values of the neutron star spin frequency, Ω. We have assumed that the single ($m = 1$) bright region has a temperature $T_{\rm col} = 3.0$ keV (at the surface), size $\rho = 60°$, is located at the equator ($\alpha = 90°$), and is viewed along the equator ($\beta = 90°$). As the compactness of the neutron star increases, the amplitude of the strongest signal A_1 decreases monotonically, because the curved photon trajectories allow the observer to see the bright region even when it is behind the limb of the neutron star. However, when $\Omega = 0$ the amplitude of the harmonic signal A_2 reaches a minimum at $p = 1.7$, and increases for smaller values of p because the neutron star lenses the bright region when it is on the opposite side of the star from the observer (Pechenick et al., 1983; Miller & Lamb, 1998). The signal at $2 \times \nu_{\rm spin}$ from antipodal bright regions with $\rho = 60°$ located at $\alpha = \beta = 90°$ is identical to A_2 in Figure 5-3 (see below and Weinberg et al., 2001).

In all cases, increasing the spin frequency increases the amplitude of the harmonic more than that of the fundamental. Moreover, the minimum in the amplitude of the harmonic at $p = 1.7$ disappears when the neutron star is spinning rapidly. This is because the light travel time of the photons becomes comparable to the rotational period of the star, which delays the arrival of the harmonic peak formed by strong lensing. Thus, the power in A_2 is transferred to higher harmonics for a rapidly spinning neutron star.

We adopted a fiducial value of $p = 2.5$ for the rest of the calculations, corresponding to a neutron star of mass 1.4 $M_\odot$ and radius 10 km. If instead we choose $p = 2.0$, the amplitudes of the fundamental signals decrease by a factor of 1.2 in the following figures, and the amplitudes of the harmonic signals decrease by a factor of 1.5–2.0 (Figure 5-3). This decrease in the amplitude would not change qualitatively the results that we describe in Section 5.3.

We then explored the effects of changing the temperature and angular dependence of the emission from the hot region, in order to select fiducial values for the rest of our study. Miller & Lamb (1998) have shown that varying the temperature of the emitting region only changes the amplitudes of oscillations when the peak of the X-ray spectrum lies at energies lower than the response of the detector. For the temperature ranges of the observed bursts,

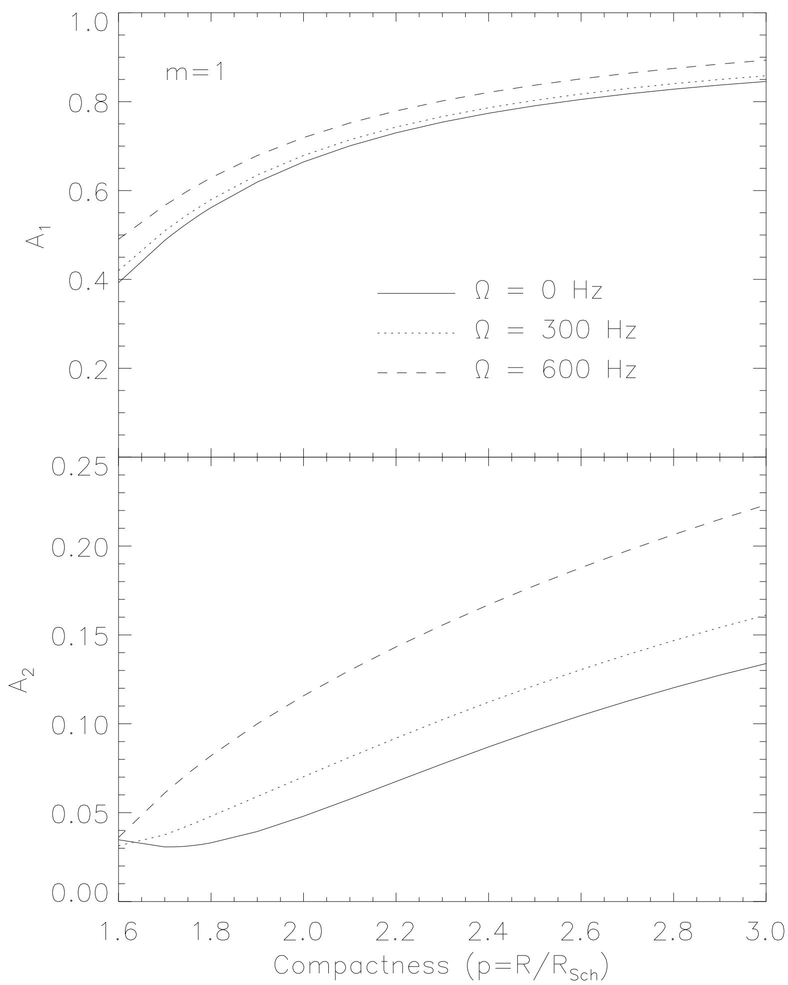

Figure 5-3 The predicted amplitudes of the oscillations as a function of the compactness p of the neutron star, for a few values of the spin frequency Ω. One hot region of size $\rho = 60°$ and of uniform temperature $T_{\rm col} = 3.0$ keV (at the neutron star) is located on the rotational equator ($\alpha = 90°$), with the observer also viewing along the equator ($\beta = 90°$). Increasing the radius (higher p) or the spin frequency (Ω) of the star generally increases the amplitudes A_1 and A_2. The amplitudes A_1 of an $m = 2$ emission geometry at $\alpha = \beta = 90°$ will be the same as A_2 in this figure.

$T_{\text{col}} \sim 2 - 3$ keV, we find that the amplitudes are essentially constant as a function of T_{col}, since most of the flux is emitted in the 2–60 keV PCA bandpass. We use $T_{\text{col}} = 2.3$ keV (as observed at infinity) in all of the following simulations.

As the emission is peaked more strongly about the normal to the surface, the amplitudes of the oscillation and its harmonics can be increased arbitrarily (Weinberg et al., 2001; Özel, 2002). The amplitudes at small compactness ($p < 2$) are particularly sensitive to the assumed beaming (Özel, 2002). For instance, if the emission is assumed to be isotropic and the star is not spinning, the harmonic signal disappears near $p = 2.0$ (Miller & Lamb, 1998), but reappears for $p < 1.75$ when the spot is strongly lensed by the neutron star (compare Figure 5-3 and Pechenick et al., 1983). The difference is less stark when the star is spinning; only the minimum at $p = 1.75$ is evident, and the harmonic does not disappear (not shown). Here, we restrict ourselves to beaming that is described by the Hopf function (Chandrasekhar, 1960), which is probably most relevant for these scattering-dominated atmospheres (compare Madej, 1991). The Hopf function is slightly more radially peaked than isotropic emission.

We now examine in detail the effects of changing the parameters directly related to the geometry of the hot regions, α, β, and ρ. We first restrict both the position of the emission region and the observer's line of sight to the neutron star's rotational equator ($\alpha = \beta = 90°$). In Figure 5-4, we plot the fractional rms amplitude of the oscillations and their harmonics as a function of the size of the hot region (ρ) for several values of the rotational frequency as observed at infinity. For a single hot region, larger areas produce lower-amplitude oscillations at the fundamental frequency (A_1), since the hot region is visible to the observer for a greater fraction of the rotational period. In contrast, the signal at the harmonic (A_2) disappears when the bright region covers exactly half of the neutron star, and then increases again as ρ exceeds $90°$.

For two identical, antipodal emitting regions with $\alpha = \beta = 90°$, no signal is seen at the neutron star's spin frequency because of symmetry. Therefore, in the $m = 2$ case we take A_1 to be the amplitude of the strongest observed signal (consistent with the definition in Figure 5-2), which occurs at twice the spin frequency of the neutron star (see also Miller, 1999). For the particular case of $\alpha = 90°$ or $\beta = 90°$, the amplitude at $2 \times \nu_{\text{spin}}$ for two bright regions with size ρ is exactly the same as that at $2 \times \nu_{\text{spin}}$ for one bright region of the same size (see also Figure 5-5). The lower right panel of Figure 5-4 demonstrates that the signal at four times the spin frequency (A_2) is always less than 5% rms amplitude. Since the rotational frequencies of the neutron stars we are studying must be of order 300 Hz or less if an $m = 2$ brightness asymmetry is responsible for the oscillations, we would only expect to see harmonics with $A_2 < 2\%$ amplitude, or 6% of the amplitude of the main signal (A_1). This is similar to our best upper limits on the amplitude of such a signal in Figure 5-2, indicating that we do not have the sensitivity to detect a signal at A_2 from antipodal bright regions. Therefore, we do not consider this signal further.

In Figure 5-5, we consider the effect of changing the position of the hot region (α) and the viewing angle (β) on the amplitude of the oscillations and their harmonics. We display the amplitudes of signals from $m = 1$ or $m = 2$ bright regions with fixed size $\rho = 60°$. For the $m = 1$ case, the amplitudes of the oscillations at both the fundamental (A_1) and harmonic (A_2) decrease as either the observer's line-of-sight or the center of the hot region is moved away from the rotational equator. Note also that the amplitude of the harmonic decreases more quickly with decreasing angles than that of the fundamental. However, for $\alpha < 90°$, the largest amplitude oscillation occurs when the observer is near the opposite pole, i.e., $\beta = 180° - \alpha$.

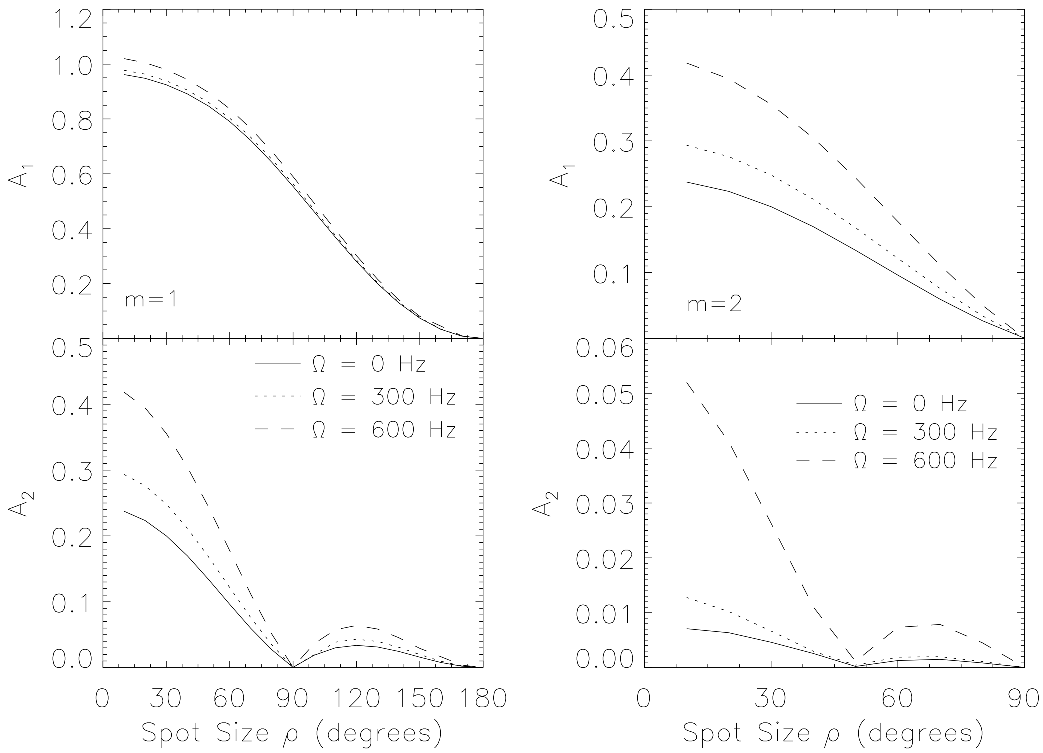

Figure 5-4 The predicted amplitudes of oscillations and their harmonics from $m = 1$ or $m = 2$ emission geometries with temperature $T_{\rm col} = 2.3$ keV (at the observer) as a function of their of size ρ and of the spin frequency Ω. Here, $\alpha = \beta = 90°$. *Left Panels*: Amplitudes from $m = 1$ bright region, where A_1 occurs at the spin frequency. *Right Panels*: Amplitudes from $m = 2$ bright regions, where no signal appears at the spin frequency, and the strongest signal A_1 occurs at twice the spin frequency. In all cases the amplitudes of the oscillations increase with larger Ω, and generally decrease with increasing ρ.

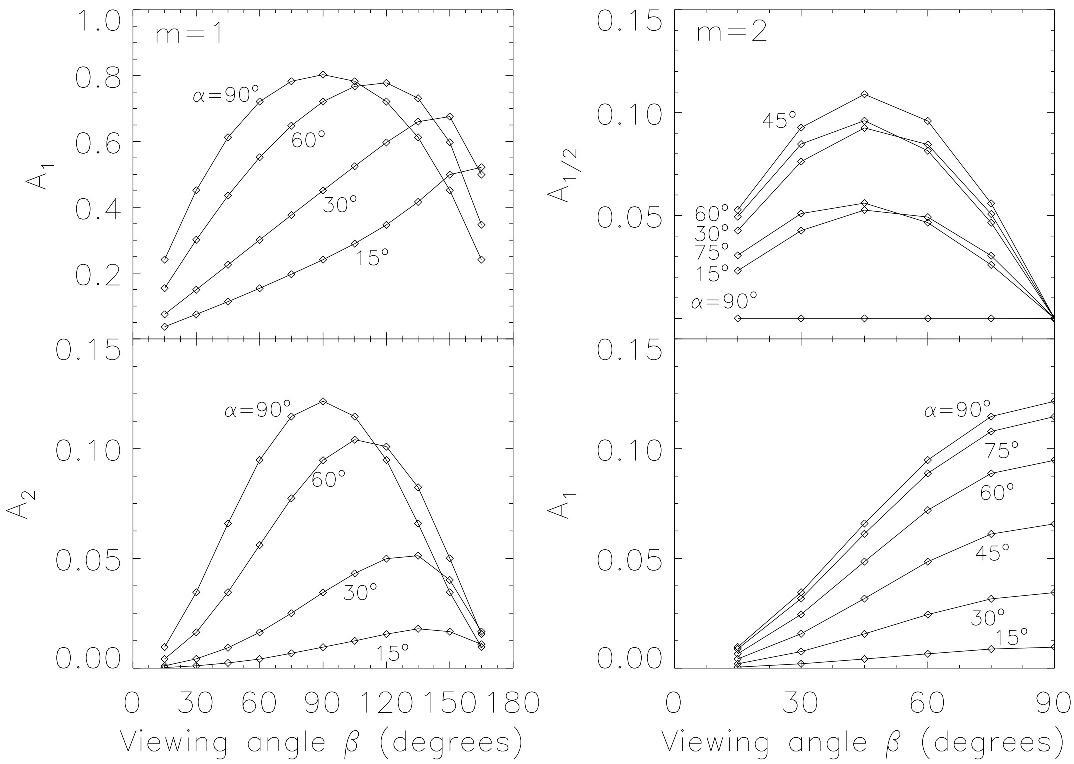

Figure 5-5 The predicted amplitudes of oscillations and their harmonics from $m = 1$ (*left panels*) and $m = 2$ (*right panels*) hot regions, located at various angles α and viewed from lines of sight $15^\circ < \beta < 165^\circ$. Here, $\rho = 60^\circ$ and $\Omega = 300$ Hz. For the $m = 1$ case, the amplitudes of both the fundamental (A_1) and the harmonic (A_2) decrease when α or β moves away from the equator (90°). For the $m = 2$ case, power is transferred from A_1 at $2 \times \nu_{\rm spin}$ to $A_{1/2}$ at $\nu_{\rm spin}$ with decreasing α or β.

For the $m = 2$ case, one observes a signal at the spin frequency of the neutron star whenever both the emitting regions and the observer's line-of-sight are away from the equator ($\alpha < 90°$, $\beta \neq 90°$ in Figure 5-5). We refer to this signal as $A_{1/2}$, consistent with the assumption that several observed signals may occur at $2 \times \nu_{\rm spin}$ from an $m = 2$ geometry (Miller, 1999). However, it is clear from Figure 5-5 that as the viewing angle decreases ($\beta < 90°$), the amplitude of the signal at twice the spin frequency (A_1 here) decreases monotonically, while that at the spin frequency ($A_{1/2}$) reaches a maximum at $\beta = 45°$. In fact, $A_{1/2}$ is larger than A_1 for most combinations of α and β.

5.3 Properties of the Brightness Asymmetries

In this section, we compare the observed properties of the burst oscillations with the model profiles presented in Section 5.2. We first determine the range of sizes and locations of the hot regions that are consistent with the evolution of the amplitude of the oscillations as a function of time (Section 5.3.1). We then examine the constraints that the lack of harmonic signals place on the emission geometry (Section 5.3.2).

5.3.1 Amplitude Changes in the Oscillations

Figure 5-6 shows the amplitude evolution of an oscillation from 4U 1636−536. Superimposed are theoretical amplitudes expected from several combinations of the size (ρ) and location (α) of the hot region, and of the viewing angle (β).

It is evident that several different combinations of these parameters can produce identical fractional amplitudes, because a smaller hot region located near the pole of the neutron star will on average cover the same fraction of the observer's view of the neutron star as will a larger region on the equator, which is obscured as it passes behind the neutron star (Figures 5-4, 5-5, and 5-6). Moreover, it is also possible to produce smaller oscillations with small hot regions if the rest of the neutron star is emitting flux within the PCA bandpass. Thus, the amplitudes of the oscillations do not provide interesting constraints on the parameters of a brightness asymmetry, unless the amplitudes are very large (Miller & Lamb, 1998; Nath et al., 2002).

Changes in the amplitude of the oscillation throughout the burst can be caused by variations in the size (ρ) or position (α) of the bright region, and by changes in the magnitude of the brightness contrast. Oddly enough, the amplitude variations are not correlated with any particular feature of the burst (Figures 4-3 and 5-6). If the oscillations are due to brightness patterns on the neutron star surface, then the properties of the asymmetry must vary independent of the amount of flux emitted from the photosphere.

We also computed the mean PCA flux we would expect from the same range of α, β, and ρ. The predicted count rates are consistent with those observed, given $T_{\rm col} \approx 2-3$ keV, but neglecting scattering effects that can greatly modify the spectrum (London et al., 1984; Madej, 1991). Thus, thermal emission from hot regions on a neutron star can explain both the mean fluxes during thermonuclear X-ray bursts and the amplitudes of the oscillations.

5.3.2 Harmonic Structure of the Oscillation Profiles

The lack of harmonic structure in the oscillation profiles (Figure 5-2 and Table 5.1) provides interesting and stringent constraints on the emission geometry. Since the amplitudes of the oscillations vary significantly (Figures 4-3 and 5-6), the best means of using the harmonic

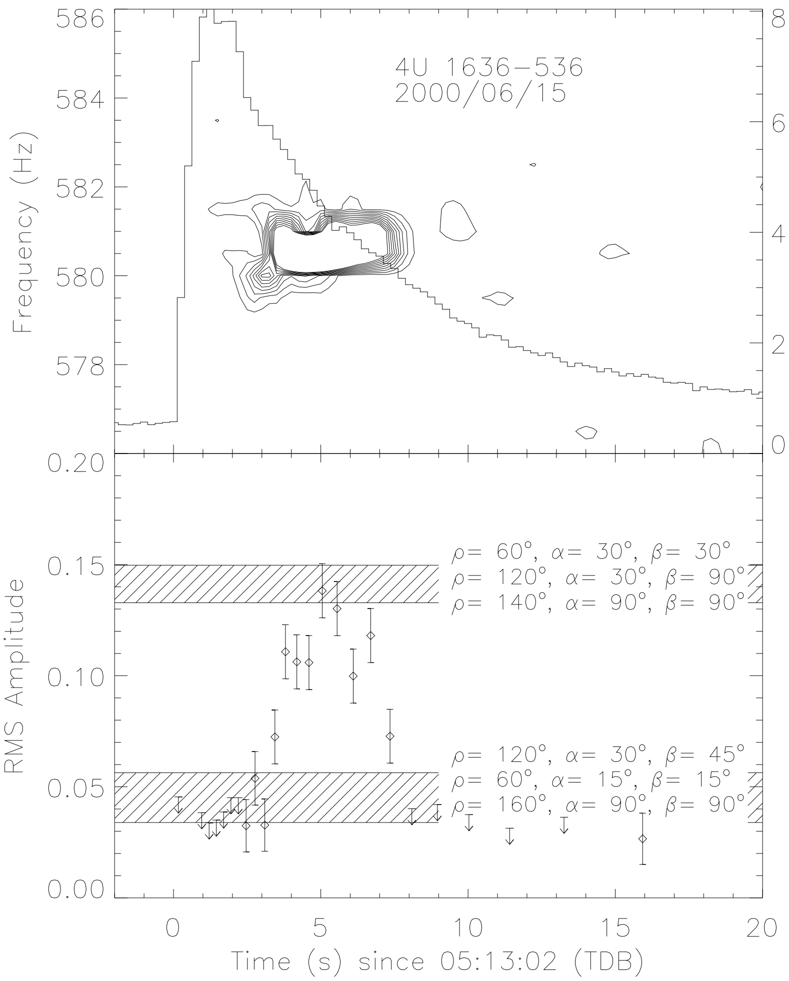

Figure 5-6 Same as Figure 4-3, for a burst from 4U 1636−536. The hatched regions indicate the range of ρ, α, and β for a single bright region that are consistent with the observed amplitudes. Amplitude variations during the burst can be explained by changes in the location or size of the bright region, but there are clearly degeneracies in these parameters that prevent us from determining them from the amplitudes alone.

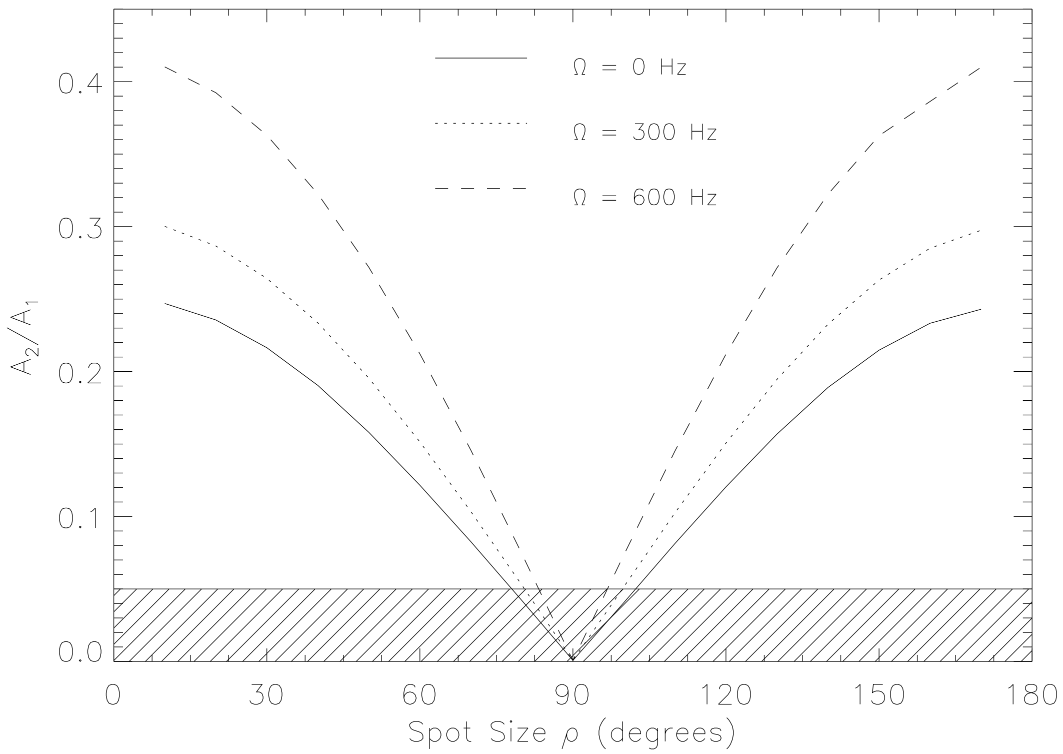

Figure 5-7 The ratio of the amplitude of the harmonic signal to that of the fundamental, as a function of size (ρ) and spin period (Ω), for the one bright region at $\alpha = \beta = 90°$. The hatched region indicates those values of A_1/A_2 consistent with the upper limits from 4U 1728−34 in Figure 5-5, and demonstrates that a circular bright region located on the equator must have an angular radius of $\rho = 90° \pm 10°$ in order to suppress the harmonic content of the oscillations.

amplitudes as a constraint is to examine the ratios of the upper limits on their amplitudes (A_n) to that of the largest signal (A_1; Figure 5-2).

For the case of an $m = 1$ brightness asymmetry, the largest harmonic signal occurs at twice the spin frequency of the neutron star. There are three ways to suppress a signal by varying the parameters of the hot region, as we show below: requiring $\rho \approx 90°$, $\alpha \leq 20°$, or $\beta \leq 30°$. Results are displayed for $p = 2.5$, but are not greatly sensitive to the compactness. For instance, assuming $p = 2.0$ decreases the relative amplitude of the harmonic signals by about a factor of 1.4 (Figure 5-3).

In Figure 5-7, we plot for a few values of the spin frequency (Ω) the ratios of the amplitudes at the first harmonic to that at the spin frequency (A_2/A_1) as a function of the size of the emitting region (ρ), assuming that the bright region and viewing angle are centered about the equator ($\alpha = \beta = 90°$; compare Figure 5-4). The shaded region represents the range of A_2/A_1 consistent with the upper limits from 4U 1636−536 and 4U 1728−34 in Figure 5-2. Clearly, any single bright region at $\alpha = \beta = 90°$ must cover almost exactly half the neutron star ($80° \leq \rho \leq 100°$).

As indicated in the top panel of Figure 5-5, A_2 from an $m = 1$ brightness asymmetry also decreases relative to A_1 if the observer or the bright region are moved away from the

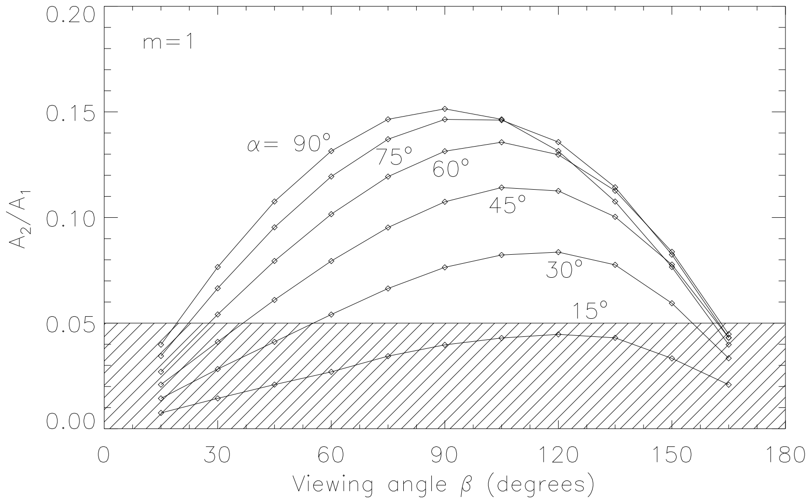

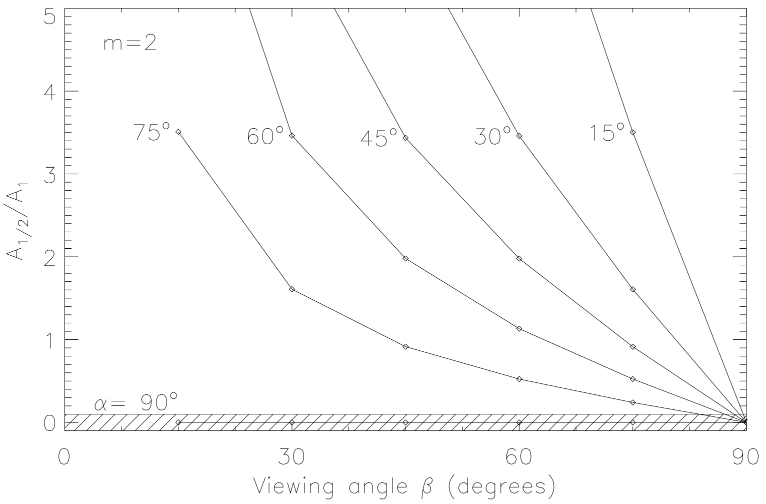

Figure 5-8 The ratio of harmonic signals to the main signals as a function of the viewing angle (β) and the location of the bright region (α). Here, $\rho = 60°$ and $\Omega = 300$ Hz. The hatched regions indicate the ranges of angles consistent with the upper limits in Figure 2. *Top Panel*: For one bright region, the harmonic content is suppressed if the bright region is located at the pole ($\alpha < 20°$) or the oscillation is viewed from along the pole ($\beta < 30°$). *Bottom Panel*: For two bright regions, one would observe signals at both $\nu_{\rm spin}$ and $2 \times \nu_{\rm spin}$ unless either the bright regions are centered about the equator ($\alpha = 90°$) or the observer's line of sight is along the equator ($\beta = 90°$).

equator. We have plotted A_2/A_1 as a function of these angles in the top panel of Figure 5-8, for a $\rho = 60°$ hot region. The shaded region once again indicates the range of angles consistent with the upper limits in Figure 5-2. The harmonic components can be suppressed if the observer's line-of-sight is nearly aligned with the spin axis ($\beta < 30°$) or if the bright region is centered near the pole ($\alpha < 20°$). It is unlikely that all of these systems are viewed along their rotational axis. The eclipses from MXB 1659−298 indicate that it is in fact viewed near its orbital plane (Cominsky & Wood, 1984), which presumably lies in the rotational equator. Therefore, it appears that an $m = 1$ brightness pattern either (*i*) forms near the rotational pole, or (*ii*) is symmetric on the neutron star surface, with an opening angle of $\rho \approx 90°$.

For the $m = 2$ case, the lack of a signal at the half-frequency ($A_{1/2}$) provides the most interesting constraints (compare Figure 5-4 and 5-5). It has already been demonstrated that the lack of such a signal implies that the two bright regions must be nearly perfectly antipodal and have almost exactly the same brightness (Weinberg et al., 2001). We estimate that the signal at the spin frequency will have an amplitude less than 10% that at $2 \times \nu_{\rm spin}$ only if the hot regions are antipodal to within 2°, and have no more than 2% difference in their relative brightness.

In the bottom panel of Figure 5-8, we show the ratio of the expected signals at the spin frequency of the neutron star to those at twice the spin frequency ($A_{1/2}/A_1$) as a function of the angles α and β for an $m = 2$ pattern. Assuming that the strongest observed signal occurs at $2 \times \nu_{\rm spin}$, we have indicated with a shaded region those angles for which the relative amplitudes of the $A_{1/2}/A_1$ signals are consistent with the upper limits in Figure 5-2. This shows that if an $m = 2$ brightness pattern is present, either (*i*) the observer's line of sight must be within a few degrees of the equator ($\beta = 90°$) or (*ii*) the hot regions must be centered on the equator ($\alpha = 90°$), in order for the two regions to appear symmetric to the observer. Regarding the first possibility, if the $m = 2$ model is to be applied to all of the sources with oscillations near 600 Hz (Miller et al., 1998; Miller, 1999, see also Table 5.1), it seems unlikely that 4 of the 6 systems in Figure 5-2 are observed along the rotational equator ($\alpha = 90°$). Although the X-ray eclipses from MXB 1659−298 suggest it is observed nearly edge-on (Cominsky & Wood, 1984), there is no reason to believe that Aql X-1, 4U 1636−536, and KS 1731−260 are. If an $m = 2$ brightness asymmetry is giving rise to the burst oscillations, the second possibility is the only likely one, i.e. some mechanism must force the hot regions to form on the rotational equator.

In addition, we can also examine the possibility that all of the sources form an $m = 2$ temperature pattern on their surface during bursts, but that we do not observe a signal at $2 \times \nu_{\rm spin}$ in a subset of the sources. By extending the bottom panel of Figure 5-8 to examine $A_{1/2}/A_1 > 15$ (not shown), we find that the observer sees only one of the two hot regions if they are located near the poles, and if they are viewed along the poles. This is precisely the opposite of the case that would allow us to see only the signal at $2 \times \nu_{\rm burst}$. Therefore, if an $m = 2$ pattern is present in all of these systems, the two hot regions must form only at the equator or near the poles.

5.4 Implications of Sinusoidal Profiles

We examined the amplitudes and profiles of a sample of 59 burst oscillations observed from 6 different neutron star LMXBs with the PCA aboard *RXTE*. On average, the rms amplitudes of the oscillations are 2–10%, and the typical folded profile contains 7×10^4 photons.

The most significant individual oscillation has a Leahy-normalized power of 615 in 1×10^5 photons, for an amplitude of 8%. However, the eclipsing source MXB 1659−298 routinely produces 10% oscillations in weak bursts (1×10^4 photons). We also produced summed pulse profiles for each source. Those from 4U 1636−536 and 4U 1728−34 contained more than 1×10^6 photons, which allowed us to place upper limits on the amplitudes of harmonic and half-frequency signals of less than 0.3% and 0.6% respectively (95% confidence). These upper limits are 6% and 10% of the amplitudes of the strongest signals (Figure 5-2 and Table 5.1). Thus, the profiles of the oscillations are remarkably sinusoidal.

We then derived theoretical lightcurves of pulsations from one or two circular bright regions on the surface of a rapidly rotating star. Comparing the observed and theoretical light curves, we find that the lack of harmonic content in the oscillations can be explained for a single bright region if it either lies near the rotational pole (Figure 5-8, *top*) or covers nearly half the neutron star (Figure 5-7). These results are fairly insensitive to the compactness of the neutron stars (Figure 5-3).

If two antipodal hot regions give rise to the flux oscillations, the situation is even more restricted (Figure 5-8, *bottom*). The bright regions would have to be located either (*i*) near the poles such that only the signal at $\nu_{\rm spin}$ is visible, or (*ii*) on the equator, so that only the signal at $2 \times \nu_{\rm spin}$ is visible. A mechanism would have to be invoked that prevents bright regions from being formed at intermediate latitudes. Furthermore, the flux difference between the two hot regions would need to be less than 2% to be consistent with the lack of harmonic signals.

The geometric constraints implied by the sinusoidal pulse shapes present a challenge for theoretical models for producing brightness patterns on the neutron star's surface. Models that invoke uneven heating or cooling (Strohmayer et al., 1997b) or hydrodynamical instabilities in a geostrophic flow (Spitkovsky et al., 2002) do not propose natural mechanisms for constraining the size and location of brightness asymmetries (Figures 5-7 and 5-8).

The most promising mechanism for producing symmetric anisotropies with restricted geometries is the excitation of global modes that propagate in the neutron star ocean (e.g., Heyl 2002). If the oscillations occur in a linear regime, the density fluctuations of an $m = 1$ oscillation would divide the neutron star into symmetric halves. An $m = 2$ mode would naturally form on the equator, its symmetry ensured by the Coriolis forces at higher latitudes. However, no physical mechanism to convert density fluctuations on the stellar surface to flux oscillations has been proposed. Furthermore, the surface velocities of the global excitations, and hence their observed frequencies, depend sensitively on the vertical structure of the neutron star atmosphere. Therefore, it is important to model the outer layers of a neutron star during thermonuclear burning and subsequent cooling in order to establish whether the frequencies of these modes are similar to those required to explain the frequency drift of the burst oscillations.

Chapter 6

Bursts that Produce Oscillations in KS 1731−260

> This chapter is adapted from the paper "Nearly Coherent Oscillations in Type I X-Ray Bursts from KS 1731−260" by Michael P. Muno, Derek W. Fox, Edward H. Morgan, and Lars Bildsten. It has appeared in *The Astrophysical Journal*, volume, 542, pages 1016–1033 (2000), and in the MIT Ph.D. thesis of Derek W. Fox (see also Section 1.5.1).

As is clear from Chapter 2, oscillations occur in less than half of the bursts from the 8 sources we have searched. Therefore, it is important to search for systematic trends in which bursts produce oscillations that could reveal the conditions required to produce strong brightness asymmetries on the stellar surface. In this chapter, we study one particular source, KS 1731−260. This source is one of a few transient LMXBs that appear and disappear on time scales of years. It was observed several times when its outburst was decaying, which provided the first opportunity to study the properties of bursts occurring over a wide range of accretion rates from a source that exhibits oscillations.

6.1 Observations of KS 1731−260

We have analyzed all 27 observations of KS 1731−260 taken between 1996 July 14 to 1999 February 27 with the *RXTE* PCA (Table 6.1). During these observations, nine X-ray bursts were seen, including the one previously reported by Smith et al. (1997).

6.1.1 Characterization of Persistent Emission and Source State

In order to characterize the persistent emission from KS 1731−260, we created background-subtracted light curves of its X-ray intensity from Standard2 data with 128 channel energy resolution and 16 s time resolution for each observation. We calculated the ratios of the count rates in the 3.4–4.8 keV : 2.0–3.4 keV bands (soft color), and in the 8.5–18.0 keV : 4.8–8.5 keV bands (hard color) for 256 s interval during each observation. The mean count rates and hardness ratios, excluding time intervals containing bursts, are listed in Table 6.1. Figure 6-1 displays the color-color diagram for this set of observations (see van der Klis, 1995, for a review of color-color diagrams in LMXB studies). The states with the lowest observed count rates correspond to points with a hard color of > 0.65, while those points

Table 6.1. PCA Observations of KS 1731−260

Observation ID	Date UT	Start Time	End Time	Exposure Time (s)	Count Rate[a]	Flux (10^{-9})[b]	Soft Color	Hard Color
10416-01-01-00	1996 Jul 14	02:32:31	07:05:31	9960	552	6.38	1.63	0.40
10416-01-02-00	1996 Aug 01	16:53:56	20:51:56	9900	344	2.74	1.50	0.39
10416-01-03-00	1996 Aug 31	17:40:17	19:44:16	3540	405	4.73	1.54	0.38
20085-01-01-01	1997 Oct 28	22:12:38	03:41:39	13080	404	4.69	1.62	0.40
20085-01-01-02	1997 Oct 29	06:22:45	08:28:45	4320	467	5.37	1.65	0.41
20085-01-01-03	1997 Oct 29	18:00:34	20:00:33	4320	489	5.63	1.62	0.43
20085-01-01-00	1997 Oct 29	21:07:33	11:39:33	28260	505	5.85	1.71	0.46
30061-01-01-00	1998 Jul 31	11:26:08	15:17:07	9000	377	4.36	1.65	0.40
30061-01-01-01	1998 Aug 01	01:49:06	04:09:07	6480	381	4.42	1.53	0.42
30061-01-01-02	1998 Aug 01	06:47:02	17:18:02	22980	369	4.28	1.63	0.41
30061-01-01-03	1998 Aug 01	23:04:02	02:54:02	9480	369	4.28	1.64	0.41
30061-01-01-04	1998 Aug 02	08:32:00	09:07:56	2160	378	4.36	1.65	0.40
30061-01-02-00	1998 Oct 02	03:26:02	08:40:02	11040	106	1.26	1.73	0.72
30061-01-02-01	1998 Oct 02	13:01:58	14:01:58	3600	118	1.41	1.74	0.73
30061-01-02-02	1998 Oct 03	01:49:53	04:11:54	5100	103	1.23	1.73	0.71
30061-01-02-03	1998 Oct 03	05:44:53	09:14:53	7800	109	1.30	1.61	0.71
30061-01-02-04	1998 Oct 04	05:35:44	10:49:44	11880	107	1.29	1.69	0.71
30061-01-02-05	1998 Oct 05	16:13:32	17:12:33	3540	108	1.30	1.74	0.73
30061-01-02-06	1998 Oct 06	01:49:29	09:11:29	15360	115	1.37	1.73	0.72
30061-01-02-07	1998 Oct 08	10:12:10	10:47:10	2100	128	1.55	1.58	0.61
30061-01-03-00	1999 Feb 22	18:23:17	20:59:17	7380	271	3.22	1.46	0.42
40409-01-01-00	1999 Feb 22	23:46:17	05:00:17	9300	266	3.16	1.56	0.42
30061-01-03-01	1999 Feb 25	21:35:42	23:57:42	6060	322	3.76	1.62	0.41
30061-01-03-02	1999 Feb 25	23:59:42	00:12:42	780	313	3.65	1.62	0.41
30061-01-04-00	1999 Feb 26	15:08:47	20:58:48	13380	390	4.55	1.69	0.45
30061-01-04-01	1999 Feb 27	11:56:54	14:23:55	6840	389	4.51	1.61	0.44
30061-01-04-02	1999 Feb 27	15:08:56	17:35:56	6120	380	4.38	1.69	0.42

[a] Counts per second per PCU

[b] erg cm^{-2} s^{-1} between 2–18 keV. Uncertainty is approximately 0.01×10^{-9} erg cm^{-2} s^{-1} for all entries.

with higher count rates have a hard color < 0.50. The count rate from the source is not a monotonic function of position on this diagram (Table 6.1). Although motion on the branch with lower hard color is observed in the course of several hours, the transition from hard colors of > 0.65 to < 0.50 occurred between observations separated by more than a month.

We produced power spectra of photons in the 2–60 keV *RXTE* band for each observation, in order to determine whether KS 1731−260 exhibits the canonical branches of the color-color diagram for LMXBs (van der Klis, 1995). The power spectrum of each observation was created by combining averaged power spectra from data with 2^{-13} s time resolution in 64 s intervals (covering frequencies above 0.015 Hz) with a single power spectrum of data with 2^{-3} s time resolution for the entire observation (covering lower frequencies). Bursts were excluded from the power spectra. We find that power spectra are of two types, as represented in Figure 6-2. Figure 6-2a is representative of power spectra from observations with hard colors > 0.6, which can be described as the sum of relatively weak (2% rms) low frequency noise below 0.1 Hz and strong (13% rms) flat-topped high frequency noise that decreases in power above a few Hz. Figure 6-2b is representative of power spectra from observations with hard colors < 0.5, and which can be characterized as a combination of $\sim$ 8% rmslow frequency noise below 1 Hz and weak power (2% rms) at high frequencies. Strong (> 1% rms) QPOs are not evident below 100 Hz in the power spectra from either state. Although single kHz QPOs are evident on a few occasions in photons with energies above 5 keV (not shown), twin kHz QPOs are only evident in the observation reported by Wijnands & Van der Klis (1997).

Taken together, the color-color diagram and power spectra indicate that KS 1731−260 is indeed an atoll source, as suggested by Wijnands & van der Klis (1997) (see Muno et al. 2002 for color-color diagrams of several LMXBs as observed with the *RXTE* PCA). The state with hard color > 0.65 is the Island State, which is thought to represent a low accretion rate (~ 0.01 times the Eddington rate, $\dot{M}_{Edd}$). The state with hard color < 0.50 is the Banana State, thought to occur at a somewhat higher accretion rate ($\sim 0.1\dot{M}_{Edd}$). This classification of KS 1731−260 is consistent with the presence of strong X-ray bursts — only two Z sources, GX 17+2 (Sztajno et al., 1986) and Cyg X−2 (Kuulkers et al., 1995), exhibit type I X-ray bursts. An arrow has been drawn on the color-color diagram to indicate the direction believed to correspond to increasing accretion rate (Muno et al., 2002).

We estimated the source flux during each observation (Table 6.1) by fitting the Standard2 data summed over each *RXTE* orbit with a two-component model, consisting of an exponentially cut-off power-law ($N_\Gamma E^{-\Gamma} \exp -E/kT$, where E is the photon energy, Γ is the power law photon index, kT is the cut-off energy, and N_Γ is the photon flux at 1 keV) and a Gaussian line at 6.4 keV, which is likely due to iron emission. We accounted for interstellar absorption with a low-energy cut-off equivalent to a column density of 10^{22} cm^{-2} of hydrogen (according to the value derived with *ROSAT* Predehl & Schmitt, 1995). Emission from bursts has been excluded from the spectra. Although we fit the spectra between 2.5–25 keV, the flux was calculated from the model between 2–18 keV, to correspond with the energy range used for the color-color diagram. The reduced chi-squared value for this model is less than 1.1 for all observations except 20058-01-01-00, 30061-01-03-00, and 30061-01-04-01, for which the reduced chi-squared values are near two. The derived flux is not significantly affected by the poor values of reduced-chi squared, and we report all values in Table 6.1. For a more detailed discussion of the X-ray spectrum of KS 1731−260 as observed by *RXTE* see Barret et al. (2000).

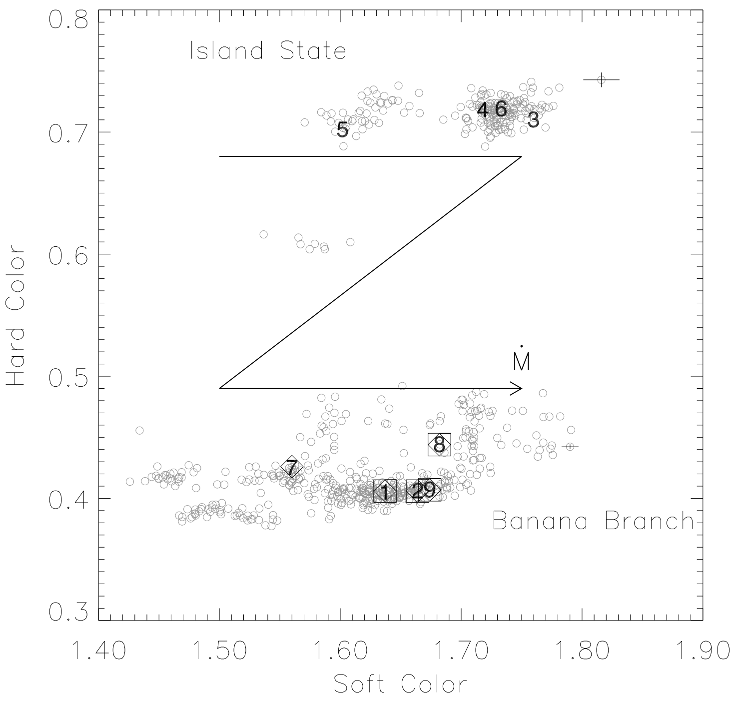

Figure 6-1 Color-color diagram from PCA observations of KS 1731-260. The Hard Color is the ratio of the count rates in the 8.5–18.0 keV and 4.8–8.5 keV bands, while the soft color is the ratio of the count rates in the 3.4–4.8 keV and 2.0–3.4 keV bands. Background subtraction was applied before calculating the ratios. Representative 1-σ error bars are plotted at the right of the figure. The numbers indicate the colors just prior to each of the nine bursts. Squares are placed around bursts which exhibited radius expansion, while diamonds were placed around those which coherent oscillations. The arrow on the figure indicates the direction of increasing accretion rate.

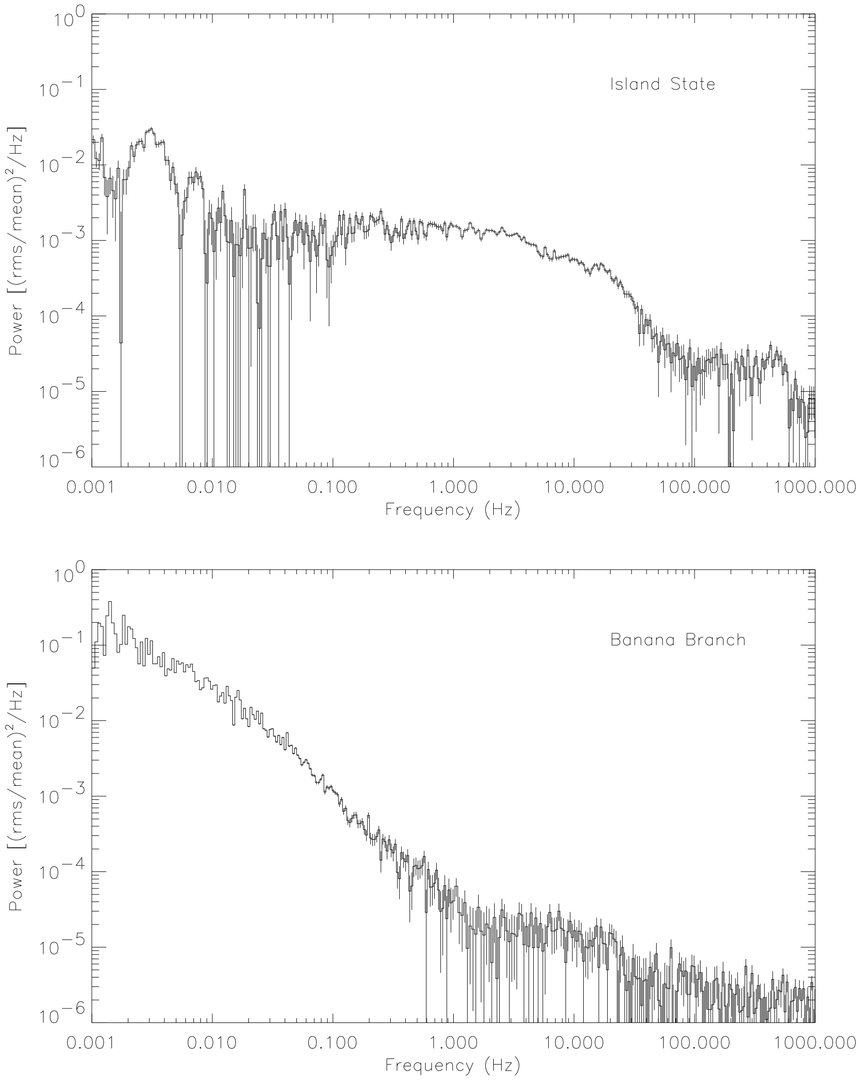

Figure 6-2 Representative power spectra from (a) the Island State (1998 October 6; 15000s), and (b) the Banana Branch (1997 October 28; 13000 s). The error bars represent the standard deviation in the powers that were rebinned for each point in the above plot.

Table 6.2. Bursts from KS 1731-260

Burst Number	Date UT	t_{rise} (s)	t_s (s)	t_d (s)	F_{peak} (10^{-8} erg cm^{-2} s^{-1})[a]	E_b (10^{-7} erg cm^{-2})	τ (s)	Radius Expansion
1	1996 Jul 14 04:23:42	3.25	4.0	4.08(8)	4.6(1)			
			11.0	9.4(6)		3.24(7)	6.6(2)	Y
2	1997 Oct 29 08:10:23	3.00	4.5	4.4(1)	6.3(1)			
			10.0	11.4(3)		4.25(7)	6.8(2)	Y
3	1998 Oct 02 07:34:54	3.75	9.0	11.0(1)	4.4(1)	7.01(7)	15.9(4)	N
4	1998 Oct 02 14:00:27	3.50	9.0	7.6(2)	4.7(1)			
			20.0	9.4(2)		7.02(8)	14.6(4)	N
5	1998 Oct 03 09:11:55	5.25	9.0	11.5(1)	3.4(1)	5.85(7)	17.2(5)	N
6	1998 Oct 06 03:26:58	2.75	9.0	9.11(6)	4.4(1)	6.78(7)	15.1(4)	N
7	1999 Feb 23 03:06:16	1.25	1.5	3.7(1)	2.1(1)	0.77(2)	3.3(2)	N
8	1999 Feb 26 17:10:53	1.50	5.0	4.01(9)	5.3(1)			
			10.0	9.2(2)		4.57(7)	8.6(2)	Y
9	1999 Feb 27 17:23:01	2.00	2.5	6.27(7)	5.2(1)			
			15.0	14.6(9)		4.65(9)	8.6(2)	Y

[a]Bolometric flux (see text).

Note. — The three times listed are the rise time of the burst (t_{rise}), the approximate starting time of the exponential decay measured from the start of the burst (t_s), and the e-folding time for the exponential decay of the burst (t_d).

6.1.2 Time Scales and Energetics of Bursts

Table 6.2 lists the times (corrected to the Earth-Sun barycenter) of the nine bursts observed with the PCA. We integrated spectra for each 0.25 s interval during these bursts using combinations of the binned and event mode data for each observation, as in Section 4.1. We modeled each energy spectrum with a blackbody modified by a constant low-energy absorption. This provides two parameters: the apparent temperature $T_{\rm col}$ and solid angle of the emission region. From the solid angle derived the apparent radius $R_{\rm col}$ of the emission region given a derived or assumed distance to the source. We also calculated the bolometric flux for each interval during the burst, $F = \pi R_{\rm col}^2 \sigma T_{\rm col}^4$. The resulting spectral parameters should be interpreted with some caution, because it is not likely that the burst emission is a pure black body. On the contrary, electron scattering in the neutron star atmosphere is likely to cause systematic deviations in the spectrum which would result in systematically high $T_{\rm col}$ (and thus low $R_{\rm col}$) at a given flux (see also the discussion in Section 6.2.1).

We analyzed the profiles and strengths of the bursts by finding the rise time t_{rise}, start time of the decay t_s, decay time scale t_d, maximum flux F_{peak}, fluence E_b, and duration $\tau = E_b/F_{peak}$ of each burst (Table 6.2). The rise time t_{rise} is defined as the time for the burst to increase from 25% to 90% of the peak flux. The start time of the decay t_s is the approximate time when the flux begins decreasing exponentially, measured from the start of the burst. We fit the decay in flux of each of these bursts with either one or two successive exponential functions, $\exp(-t/t_d)$, (for four and five bursts, respectively, depending on the value of reduced chi-squared for a fit with a single exponential) in order to estimate the time-scale for the decay of the bursts. The exponential fits work well; for all of the bursts, $\chi^2_\nu < 1.3$. Finally, we summed the total flux from the burst, integrating the exponential fit to calculate the contribution at late times, to determine the fluence of the burst E_b.

6.1.3 Radius Expansion during Bursts

The spectral parameters from three representative bursts — a large burst without radius expansion (Burst 3), a large burst with radius expansion (Burst 9), and a weak burst without radius expansion (of which we observe only one case, Burst 7) — are displayed in Figure 6-3. The apparent radius of the blackbody has been plotted assuming that the distance to KS 1731−260 is 7 kpc. The radius expansion bursts tend to be shorter than the bursts without radius expansion (as indicated by τ in Table 6.2).

The spectral fits reveal which of the bursts exhibited an episode of radius expansion (last column in Table 6.2). We find that four bursts exhibit radius expansion episodes. In all cases the effective area of the emitting region expands by a factor of 2.5–5.2. Since the maximum luminosity during the radius expansion episodes is thought to represent the Eddington luminosity of the neutron star L_{Edd}, we can use the maximum peak flux from all of the radius-expansion bursts, $F_{peak} = 6.3 \times 10^{-8}$ erg cm^{-2} s^{-1}, to estimate the distance to the source D via (van Paradijs et al., 1988a)

$$L_{Edd} = 4\pi D^2 F_{peak} = 3.6 \times 10^{38} \text{ erg s}^{-1}. \tag{6.1}$$

This provides the L_{Edd} corresponding to a pure helium photosphere for a 1.4 $M_\odot$ neutron star, if the red-shift of the photosphere is zero when the peak flux is measured. We use the largest value because some variation in the peak flux in radius expansion bursts is to be expected, as the observed Eddington luminosity decreases when a lower fraction of helium is present in the photosphere, when there is any anisotropy in the burst emission, and when

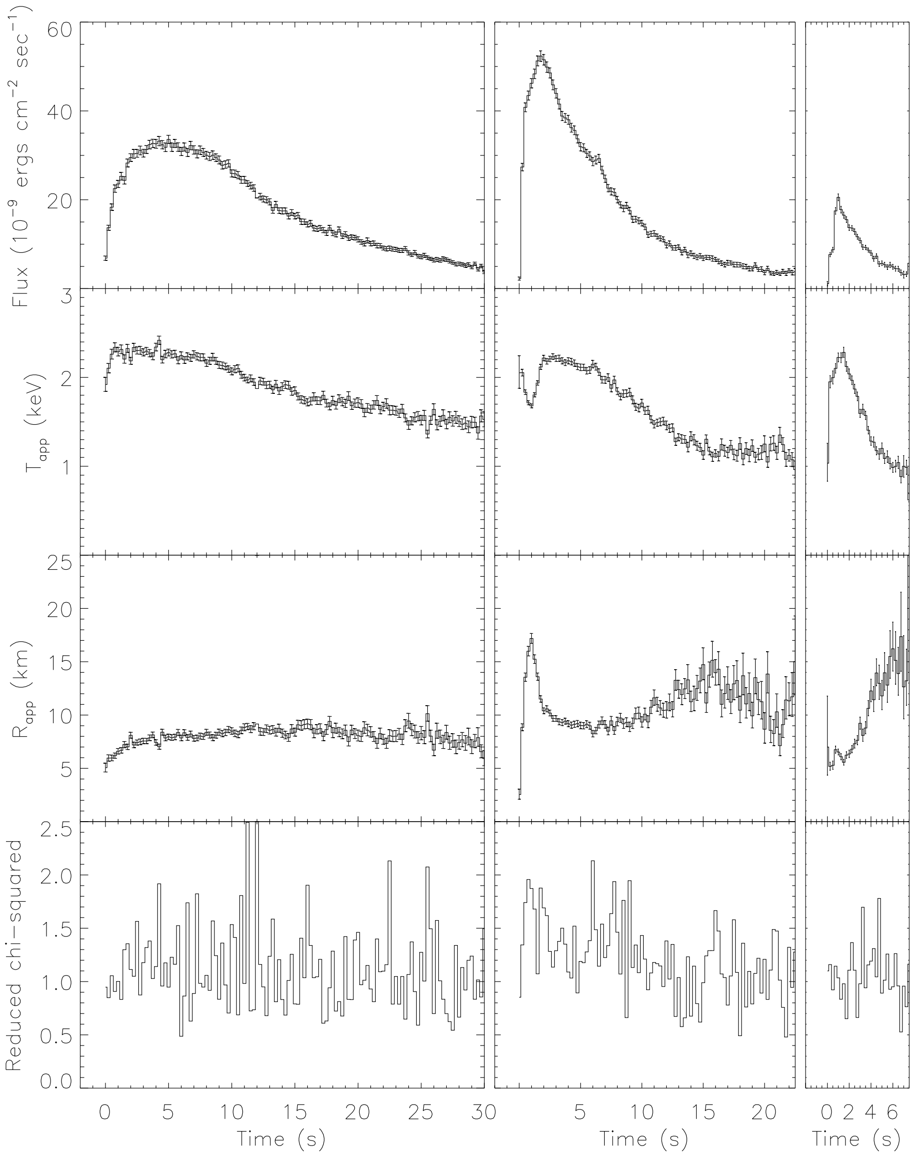

Figure 6-3 Representative spectral fits to three bursts: (a) Burst 3, a long burst with no radius expansion; (b) Burst 9, with radius expansion; (c) Burst 7, the only short, weak burst. From top to bottom are bolometric flux, color temperature, color radius (assuming a distance of 7 kpc; see text), and reduced chi-squared for the fit. Error bars plotted are 1 σ.

the red-shift of the photosphere at its maximum observed expansion is larger. Our estimate places an upper limit to the distance to KS 1731−260 of $D \approx 7$ kpc. The previous estimate of the distance to KS 1731−260 was derived from the flux from Burst 1 in the same manner as above by Smith et al. (1997).

We indicate the spectral state during which the bursts occurred by the numbers in Figure 6-1. The placement of the numbers indicates the colors of the persistent emission immediately before the burst, and a square has been drawn around the burst number if the burst exhibited radius expansion. All of the bursts that exhibit radius expansion episodes (Bursts 1, 2, 8, and 9) occurred while KS 1731−260 was on the Banana Branch, with hard color less than 0.5, while all of the large bursts without radius expansion episodes (Bursts 3, 4, 5, and 6) occurred while KS 1731−260 was in the Island State, with hard color greater than 0.6. The single small Burst 7 occurred on the banana branch, which is not surprising given its small τ and short decay time scale. This behavior was also seen in EXOSAT observations of other sources (e.g van der Klis et al., 1990).

6.1.4 Spectral Tracks during Bursts

Following Gottwald et al. (1986), in Figure 6-4 we plot the color radius (top panels) and the bolometric flux (bottom panels) from the bursts as a function of the color temperature. The numbers in the figure indicate the burst from which the data have been taken. We have only plotted points where the burst flux is greater than 15% of the peak flux from the burst, because at lower fluxes the uncertainty on the spectral parameters becomes large (see Figure 6-3). The panels on the left represent the bursts which occurred on the Banana Branch, when the persistent flux greater than 2.0×10^{-9} erg cm^{-2} s^{-1}. The panels on the right, represent the bursts which occurred in the Island State at persistent flux less than 2.0×10^{-9} erg cm^{-2} s^{-1}.

A two-branch pattern in the R_{col} versus T_{col} relationship is evident in bursts from the Banana branch (top-left panel of Figure 6-4), which is not present for the bursts from the Island State (top-right panel). The right-side ($T_{app} \sim 1.5 - 2.5$ keV) excursion to high $R_{app} \sim 12 - 22$ km represents the radius expansion phase at the start of the burst (note that Burst 7 exhibits no radius expansion, and therefore does not follow this track), while the excursion at lower temperatures ($T_{app} \sim 0.8 - 1.5$ keV, $R_{app} \sim 10 - 17$ km) represents an increase in the apparent emitting area in the tails of the fast bursts (e.g. Fig. 6-3b).

6.1.5 Recurrence Times of Bursts

It is impossible to precisely determine the time interval between bursts because KS 1731−260 is occulted by the Earth for about a third of every 90 minute *RXTE* orbit, and the observed bursts occur infrequently. We can only roughly estimate the rate with which bursts occurred during four intervals with more than 10 ks of exposure time over the course of a few days (see Table 6.1). The values that follow are uncertain by about a factor of two because of the small number of bursts detected. During the earlier observations, bursts were observed infrequently. For 1997 October 28 to 29, the source was on the Banana Branch and one burst was observed during 13.9 hours of exposure, suggesting an approximate rate of 0.07 hr^{-1}. No bursts were observed during 13.9 hours of observations during the interval from 1998 July 31 to August 1, also on the Banana Branch, which is consistent with the single burst seen in the first interval. Bursts occurred more often during later observations. KS 1731−260 was in the Island State for 1998 October 2 to 6, and the approximate burst

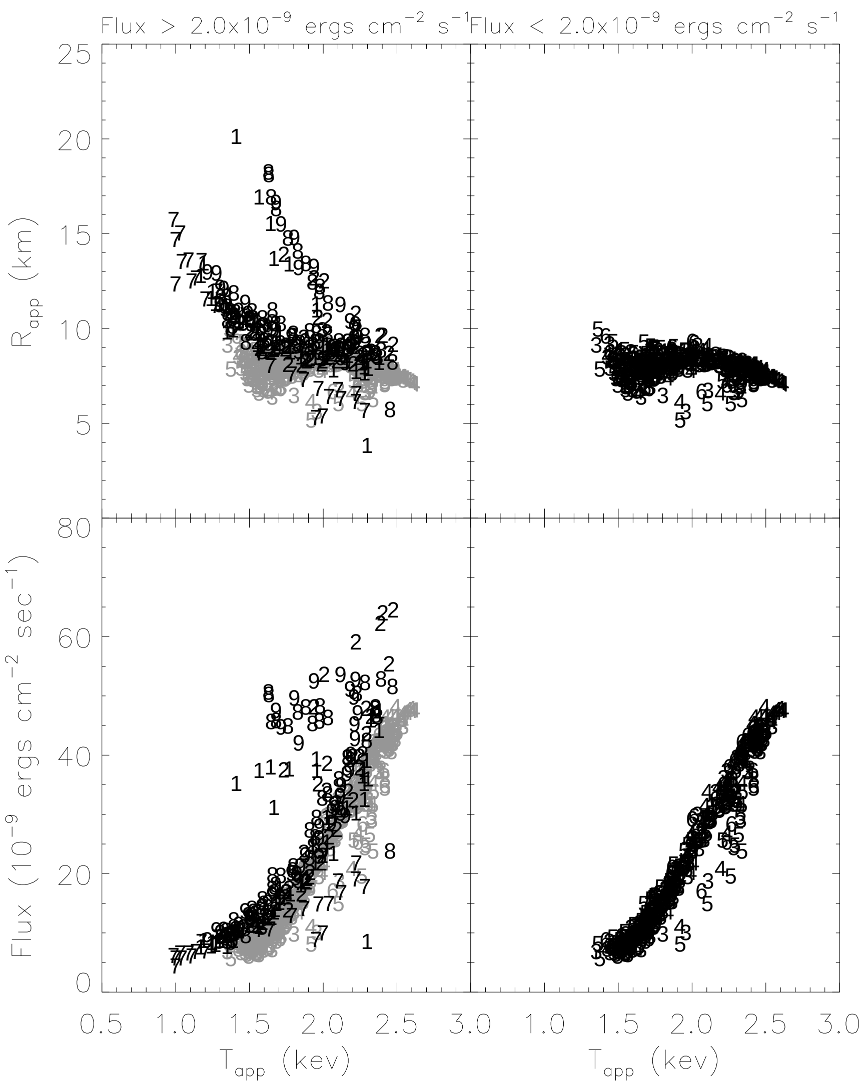

Figure 6-4 Color radius (top) and bolometric flux (bottom) plotted as a function of color temperature during the bursts. The left panels contain fast bursts, and the right panels contain slow bursts (which are also plotted in grey on the left panels). The numbers indicate the burst from which the data was taken (see Table 6.2). Error bars on the plotted values are comparable to the size of the numbers used to mark each point.

Table 6.3. Oscillations in Bursts from KS 1731−260

Burst Burst	Fundamental (% RMS)	Harmonic (% RMS)	Sub-Harmonic (% RMS)	Time[a] of Signal (s)	Signal Duration (s)	Radius Expansion
1	9.2 ± 0.6	<11.1	<5.9	2	3	Y
2	5.4 ± 1.1	<6.9	<6.1	4	2	Y
3	<9.2	<9.2	<9.9	···	···	N
4	<6.6	<8.0	<8.7	···	···	N
5	<8.9	<7.8	<9.0	···	···	N
6	<8.0	<7.2	<6.7	···	···	N
7	8.6 ± 1.1	<13.3	<8.9	0	1	N
8	6.5 ± 1.5	<5.6	<11.5	3	1	Y
9	12.6 ± 0.4	<5.6	<7.8	2	6	Y

[a]Measured from the start time of the burst; see Table 2.

Note. — Values with one-sigma error estimate represent percent RMS of the largest detected signal; upper limits represent the 90% confidence level of the percent RMS for non-detections.

rate was 0.24 hr^{-1}. During 1999 February 22 to 27 the source was again on the Banana Branch, and the burst rate was $\sim 0.22\ \mathrm{hr}^{-1}$. Thus, the burst rate does not seem to show any correlation with the spectral state of the source, which suggests that some parameter other than the accretion rate determines the frequency with which bursts occur.

We attempted to determine whether bursts could have occurred regularly during the four time intervals above. We assumed that that bursts recur with times distributed in a Gaussian fashion about mean intervals between 0.2–20 hours, and determined the probability that we would observe bursts at the times in Table 6.2. We find that either (*i*) no constant mean recurrence time is consistent with the observed bursts (and lack thereof); or (*ii*) the only consistent recurrence times are longer than our estimate of the burst times above, which would suggest that we were "lucky" to observe the bursts that we did. An alternative possibility is that bursts from KS 1731−260 occur in clusters, similar to the behavior of Ser X-1 (Sztajno et al., 1983), 4U 1735−44 (Lewin et al., 1980; van Paradijs et al., 1988b), and 4U 1636−53 (Lewin et al., 1987).

6.1.6 Search for Burst Oscillations

We searched for burst pulsations in the same manner as in Chapter 2.2. Table 6.3 reports the rms amplitudes of the largest detected oscillations, or upper limits on oscillations derived from the largest observed power, for each of the bursts. Five signals have been detected at a frequency of 524 Hz, and no significant signals have been detected at the sub-harmonic or first harmonic. The signal in Burst 7 is significant with only 90%-confidence given our broad search parameters, but since there is a (much smaller) 0.2% chance that the signal could be due to noise in a search restricted to the first second of the burst rise, we treat this signal as a detection. The rms amplitude of the oscillation in Burst 7 is large only because the count rate in the rise of the burst is a factor of 2 smaller than the other bursts (compare Table 6.2). The bursts with coherent oscillations are marked with a diamond in Figure 6-1.

A brief comparison of Table 6.3 and Figure 6-1 reveals a striking discovery. All four of the oscillations that occur after the rise of the burst were found in bursts that exhibited radius expansion episodes (Bursts 1, 2, 8, and 9). As a signal is also found in the rise of Burst 7, all of the bursts seen on the Banana Branch exhibited coherent oscillations. On the other hand, none of the bursts in the Island State (Bursts 3, 4, 5, and 6) exhibited coherent oscillations (to the sensitivity of our search).

6.2 Discussion of Bursts from KS 1731−260

Our results allow us to address a number of important aspects of the phenomenology of type I X-ray bursts and their burst pulsations.

6.2.1 Two Populations of Thermonuclear Bursts

The nine bursts that we have observed from KS 1731−260 divide into two populations, as shown in Table 6.2 and Figure 6-1. When the source is in the Island State and the persistent flux is low, bursts have relatively broad maxima (as measured by the time until the start of the burst decay), long decay time scales (τ), large fluences, and no evidence for radius expansion (Bursts 3, 4, 5, and 6); following Gottwald et al. (1986) we call these *slow bursts.* When the source is on the Banana Branch and the persistent flux is high, the peaks of bursts are sharper, the bursts are shorter, radius expansion episodes are present, and burst fluences are smaller (Bursts 1, 2, 8 and 9); we call these *fast bursts.* Burst 7 is particularly weak, but still exhibits the short decay, narrow maximum, and small τ characteristic of fast bursts. The decrease in burst duration with increasing accretion rate is consistent with the global relationship which van Paradijs et al. (1988a) reported for their sample of 10 LMXBs. Note however that they found burst properties to span a continuum between the slow and fast populations in a sample of many burst sources. KS 1731−260 itself may display a continuum of bursting properties should the source be observed for a longer period of time at an intermediate value of the inferred accretion rate (Figure 6-1).

The association between fast bursts and radius expansion has previously been noted by several authors (see, e.g., Gottwald et al. 1986 for EXO 0748−676 and Lewin et al. 1987 for 4U 1636−53). Hanawa, Fujimoto, & Miyaji (1981) suggest that the fast bursts result from the burning of helium-rich material. They predict that helium-rich bursts should occur when the accretion rate onto the surface is low, at about 0.01 $\dot{M}_{\rm Edd}$(Case 2 of Chapter 1). However, in KS 1731−260 the fluxes in Table 6.1 range from 0.02–0.1 times the Eddington luminosity (F_{peak} from Burst 2 in Table 6.2), which implies that $\dot{M} = 0.02 - 0.1\ \dot{M}_{\rm Edd}$. Radius expansion bursts are observed at higher accretion rates, contradicting expectations.

It appears that the rate at which matter accretes onto the surface while KS 1731−260 is on the Banana Branch is a factor of 10 lower than that inferred from the X-ray flux. If the Island State then represents $\dot{M} < 0.01\dot{M}_{\rm Edd}$, we might expect that bursts are triggered by episodic hydrogen burning (Case 3). However, bursts from KS 1731−260 occur every few hours in the Island State, which is more often than would be expected if hydrogen does not burn stably.

This paradox can be resolved if accretion takes place over a larger fraction of the neutron star when the total accretion rate is high, such that the accretion rate per unit area is reduced (Bildsten, 2000). Evidence for this hypothesis may be found in spectral fits to the burst emission. Gottwald et al. (1986) noted that the fitted blackbody radii during the tails of fast bursts from EXO 0748−676 were systematically larger than the radii for the slow bursts and Bildsten (2000) showed that this is adequate to change the local accretion rate. Similarly, we find that the color radii in the tails of fast bursts from KS 1731−260 are systematically larger than those of slow bursts (Figure 6-4); this behavior can also be seen in the spectral evolution of Bursts 3 and 9 in Figure 6-3. If this difference in $R_{\rm col}$ reflects a physical increase in the area of the burst emission, that might explain why the properties of bursts observed at high total accretion rates are those expected for bursts occurring at a low local accretion rate, and vise-versa.

The behavior of Burst 7 runs somewhat counter to this trend: although this burst has significantly less fluence than the other fast bursts, it exhibits a larger increase in blackbody radius during the tail of the burst. If a burst only ignites when sufficient material per unit area is accreted to produce the critical density and temperature, then larger burst areas should correspond reliably to larger burst fluences. On the other hand, if a burst occurred during the Earth occultation 25–75 minutes prior to Burst 7, then the observed burst would be similar to other weak bursts with short waiting times and relatively large apparent radii from 4U 1705−44 (Langmeier et al., 1987) and EXO 0748−676 (Gottwald et al., 1986). These weak bursts may be triggered by unburnt nuclear fuel from the previous burst (Lewin et al., 1987; Fujimoto et al., 1987), and still cover most of the star.

It is also possible that scattering in the neutron star atmosphere causes the spectra of bursts on the Banana Branch to systematically deviate from a blackbody. London et al. (1984, 1986) demonstrated that the ratio $\xi = T_{\rm col}/T_{\rm eff}$ of the color temperature derived from a blackbody fit to the effective temperature of the emission region can vary significantly as $T_{\rm eff}$ increases. Since $R_{\rm col} \propto F^{1/2}T_{\rm col}^{-2} = F^{1/2}(\xi T_{\rm eff})^{-2}$, and for a constant physical emission area $F \propto {T_{\rm eff}}^4$, we have $R_{\rm col} \propto \xi^{-2}$. Thus, if $T_{\rm eff}$ and ξ decrease together as the burst cools, $R_{\rm col}$ will appear to increase (see also Sztajno et al., 1985). If the anti-correlation between $R_{\rm col}$ and $T_{\rm col}$ in Figure 6-4 is indeed due to electron scattering, then the trend is not a probe of accretion onto the neutron star surface, but indicates that the atmosphere of the neutron star is fundamentally different in the Banana and Island states. In that case, the accretion rate paradox remains. However, whether ξ is correlated or anti-correlated with $T_{\rm eff}$ depends on the value of $T_{\rm eff}$ (London et al., 1986). The effect of scattering on burst spectra needs to be understood in more detail, as does the manner in which accreted matter spreads over the neutron star surface.

6.2.2 Fast Bursts Show Oscillations

It has been observed that coherent oscillations are not present in every burst from 4U 1728−34 and 4U 1702−43 (Markwardt et al., 1999), although no systematic study has been previously carried out to determine whether the properties of the bursts or persistent emission from those sources are correlated with the presence of detectable coherent oscillations. We find that in KS 1731−260 the presence or absence of oscillations is strictly consistent with the two burst populations we identify: all of the fast bursts exhibit near-coherent oscillations and none of the slow bursts do (to limits of about 10% RMS in any single second; see Table 6.2). The general association between fast bursts and coherent oscillations suggests that the process which produces the oscillations is related to the particularly intense helium-rich burning in these bursts.

Comparing the various time scales that we can infer for the bursts provides some insight into the origin of the oscillations. The frequency drift occurs with a time scale of several seconds (Section 4.2.2), and the time it takes for the signal to drift one cycle indicates that the hot spot moves around the star on time scales of a second (Figures 3-1 and 3-2). However, the time for the nuclear energy released at the burning layer to diffuse through the neutron star atmosphere can also be as large as several seconds (Hanawa & Fujimoto, 1984). If the hot spot is moving with respect to the photosphere more quickly than the signal from it can escape, the signal will be unobservable.

These time scales are strongly correlated with the metallicity of the burning layer. Cumming & Bildsten (2000) have shown that the smaller opacity of a helium rich shell could reduce the thermal diffusion time through the atmosphere. Under the contracting burning layer model of (Strohmayer et al., 1997b), they also found that the time for the hot spot to drift is longer when more helium is present, because the higher mean molecular weight of helium prevents the burning layer from expanding as far. The combination of the two effects implies that a signal from a contracting burning layer is more likely to be observed during a pure helium burst.

The possible connection between helium bursts and oscillations has not been explored under the hydrodynamical instability (Spitkovsky et al., 2002) or the Rossby mode (Heyl, 2002) models. Should similar relationships be observed in other systems, investigation along these lines could be very fruitful. A search for such trends is the subject of the next chapter.

Chapter 7

Photospheric Radius Expansion and Oscillations

> This chapter was adapted from the paper "Millisecond Oscillations and Photospheric Radius Expansion in Thermonuclear X-Ray Bursts" by Michael P. Muno, Deepto Chakrabarty, Duncan K. Galloway, and Pavlin Savov, which appeared in *The Astrophysical Journal*, volume 553, pages L157–L160 (2001).

Although burst oscillations in KS 1731−260 appear only during intense bursts that exhibit photospheric radius expansion, further studies of a second source, 4U 1728−34, demonstrate that this can not be a general trend (van Straaten et al., 2001; Franco, 2001). In 4U 1728−34, oscillations are often observed in bursts without radius expansion, and many radius expansion bursts lack oscillations. This contradicts the suggestion that the oscillations require a helium-rich burning layer to form (Cumming & Bildsten, 2000). On the other hand, oscillations in both KS 1731−260 and 4U 1728−34 are only observed at high inferred accretion rates. This suggests that oscillations may always be present, but that structures in the accretion flow at low $\dot{M}$ obscure the oscillations (Franco, 2001).

To pursue these results further, we examined the properties of bursts that exhibit pulsations in all 9 oscillation sources.

7.1 Data Analysis

We have examined all observations of 8 of the 9[1] burst oscillation sources in the *RXTE* public archive as of 2001 March 22. We searched all of the data taken with the *RXTE* Proportional Counter Array (PCA) for type I bursts and found a total of 125 bursts with data that allowed both timing and spectral analyses. These bursts are summarized by source in Table 1. We searched for oscillations as described in Section 2.2. For the five sources for which detailed burst studies have been published, our results are consistent with the published work (MXB 1659−298: Wijnands, Strohmayer, & Franco 2001; Aql X-1: Fox et al. 2001; KS 1731−260: Chapter 6; 4U 1728−34: Franco 2001, van Straaten et al. 2001; and 4U 1916−05: Galloway et al. 2001).

[1]Since the localization of bursts associated with MXB 1743−29 is uncertain due to its proximity to the bursting pulsar GRO J1744−28, we use the results from Strohmayer et al. (1997a). For the same reason, the persistent emission cannot be isolated for this source.

Table 7.1. Burst Oscillations (BOs) and Photospheric Radius Expansion (PRE)

Source Name	$\nu_{\rm burst}$ (Hz)	Total Bursts	Number (Percentage) of Bursts: BOs PRE	no BOs PRE	BOs no PRE	no BOs no PRE	$F_{\rm ASM}$[a] (c s^{-1})	D (kpc)	$P_{\rm orb}$ (hr)	Ref.
Fast Oscillators										
4U 1608−522	620	6	2 (33%)	0	0	4 (67%)	3.36	4.0	···	[1,2]
MXB 1743−29	589	3	3 (100%)	0	0	0	···	···	···	[3]
4U 1636−536	581	16	12(75%)	0	2 (13%)	2 (13%)	14.55	6.5	3.8	[2,4,5]
MXB 1659−298	567	15	5 (33%)	5 (33%)	1 (7%)	4 (27%)	0.74	10[b]	7.1	[4,6]
Aql X-1	550	10	3 (33%)	1 (10%)	0	6 (60%)	2.79	4.8	19	[2,7,8]
KS 1731−260	521	13	4 (31%)	0	1 (4%)	8 (62%)	10.12	7	···	[5]
Total Fast		60	26 (46^{+7}_{-6}%)	6 (10^{+5}_{-3}%)	4 (6^{+5}_{-1}%)	24 (38^{+7}_{-5}%)[c]				
Slow Oscillators										
4U 1728−34	363	49	11 (22%)	11 (22%)	16 (33%)	11 (22%)	6.58	4.3	···	[10,11,12]
4U 1702−429	330	8	0	0	7 (87%)	1 (13%)	3.50	6.7	···	[4,12]
4U 1916−053	270	8	0	5 (50%)	1 (10%)	2 (20%)	1.21	10	0.83	[2,13,14]
Total Slow		65	11 (17^{+6}_{-3}%)	16 (25^{+6}_{-4}%)	24 (37^{+7}_{-5}%)	14 (22^{+6}_{-4}%)[c]				

[a] Mean 1.5-12 keV count rate observed with *RXTE*/ASM.

[b] Distance was derived assuming the peak flux from the brightest burst observed with *RXTE* represents the Eddington luminosity for pure helium.

[c] 1-σ uncertainties derived assuming a binomial distribution (see text).

References. — [1] Chakrabarty, priv. comm.; [2] Christian & Swank (1997); [3] Strohmayer et al. (1997b); [4] current paper; [5] Smale & Mukai (1988); [6] Cominsky & Wood (1984); [7] Fox (2000); [8] Chevalier & Ilovaisky (1991) [9] Muno et al. (2000); [10] Franco (2001); [11] van Straaten et al. (2001); [12] Ford et al. (2000); [13] Galloway et al. (2001); [14] Walter et al. (1982)

In order to characterize the persistent emission, we calculated average soft (3.7–5.1 keV/2.3–3.7 keV) and hard (8.7–18 keV/5.1–8.7 keV) X-ray colors for 256 s intervals using background-subtracted light curves. Location on an X-ray color-color diagram is a good tracer of the accretion rate $\dot{M}$ (see van der Klis 1995 and references therein). KS 1731−260 (Muno et al., 2000) and 4U 1728−34 (Franco, 2001; van Straaten et al., 2001) exhibit bursts over the widest range of $\dot{M}$, while cursory checks of the color-color diagrams for the other sources suggest that bursts were only observed at high accretion rates, because few or no observations were made during low $\dot{M}$ intervals.

We produced energy spectra for each 0.25 s interval from each burst using available combinations of data modes which provide at least 32 energy channels. We subtracted spectra from 15 s of emission from before the burst to account for background, and fit each spectrum between 2.5–20 keV with a model consisting of a blackbody multiplied by a constant interstellar absorption (determined from the mean value from fits using variable absorption). The model provides an apparent temperature ($T_{\rm col}$) and a normalization equal to the square of the apparent radius ($R_{\rm col}$) of the burst emission surface, and allows us to estimate the bolometric flux as a function of time. The peak flux of bursts from a given source can vary by a factor of 5–10. In many bursts, photospheric radius expansion is evident at the start of the burst, during which $R_{\rm col}$ increases and $T_{\rm col}$ decreases such that the bolometric flux remains constant, presumably at the Eddington limit (see Figure 4-1 and Lewin et al. 1995). Our definition of radius expansion includes bursts which exhibit a second increase in radius immediately after the minimum which follows the expansion phase. We find several such bursts from 4U 1728−34 (see also van Straaten et al., 2001), and one such burst from both 4U 1916−053 and 4U 1608−522.

7.2 When Oscillations Occur

A summary of our results for the nine burst oscillation sources is given in Table 7.1. There is a tight connection between the presence of oscillations and of radius expansion in fast ($\simeq$ 600 Hz) sources from every perspective. Fast oscillations occur predominantly during bursts with radius expansion, and almost all bursts with radius expansion exhibit oscillations. At the same time most of the bursts without fast oscillations also lack radius expansion. In slow ($\simeq$ 300 Hz) sources, there is no preference for whether bursts with or without radius expansion exhibit oscillations. This suggests that the frequencies of burst oscillations and the properties of bursts are connected.

Although the sample of bursts from an individual source is in some cases quite small, the correlations for fast and slow sources as groups are quite significant. In order to quantify the significance of our results, we hypothesize that radius expansion occurs in bursts with a fixed probability, f. Given a sample of m bursts, the probability of observing a number n of bursts with radius expansion is

$$P(n|f,m) = f^n(1-f)^{m-n}\frac{m!}{n!(m-n)!}.$$

We can then compute the probability density for f given n radius expansion bursts in a sample of m bursts. We plot these probability densities in Figure 7-1 for fast and slow sources, considering as our sample population either all observed bursts (dashed line) and only those bursts which exhibit oscillations (solid line). Although fast and slow sources exhibit radius expansion in about equal fractions of bursts in general, fast sources exhibit

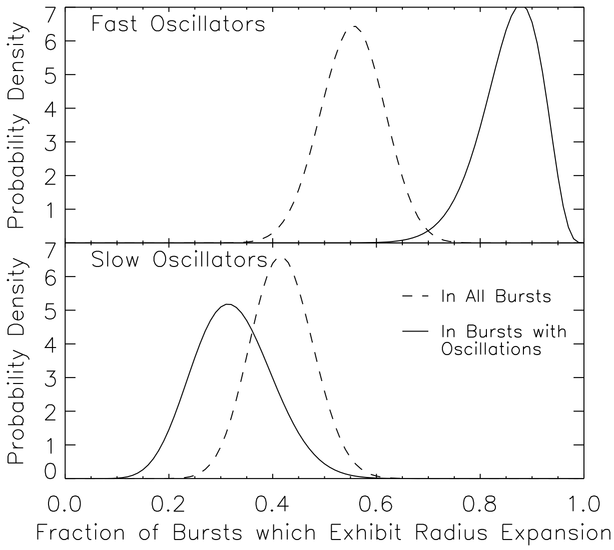

Figure 7-1 The probability that radius expansion bursts occur in a given fraction of all bursts (*dashed line*) and of bursts in which oscillations are observed (*solid line*), assuming that the number of radius expansion bursts out of a sample population is distributed according to a binomial distribution.

radius expansion during bursts with oscillations far more often (88^{+4}_{-8}% of the time) than slow sources (31^{+10}_{-6}%). The trends for individual sources are interesting in that they follow the behavior expected from considering the sources as groups (Figure 7-2). On the other hand, slow sources are more likely to show radius expansion during bursts *without* oscillations (53^{+9}_{-8}%) than fast sources (20^{+10}_{-5}%).

We can rule out some observational selection effects as causes for these correlations. For example, we are not systematically missing oscillations from weak bursts, as might occur if all oscillations had the same fractional amplitude. We observe oscillations in some of the weakest bursts from KS 1731−260, 4U 1636−536, 4U 1916−053, and 4U 1728−34, while no oscillations are detected during some of the stronger bursts from these sources. Therefore, our correlations are based upon genuine variations in the strengths of the oscillations.

However, since bursts were observed from only two sources at low $\dot{M}$ (KS 1731−260 and 4U 1728−34), there is a remote chance that these correlations are an artifact of the higher $\dot{M}$ at which the remaining sources were observed. For instance, the bursts with the longest time scales take place at low fluxes in 4U 1608−522 (Murakami et al., 1980) and at low inferred $\dot{M}$ in 4U 1636−536 (van der Klis et al., 1990). It is reasonable to believe that these long bursts do not exhibit radius expansion (as in KS 1731−260), so there would be no strict relationship between radius expansion and fast oscillations if these bursts exhibit oscillations. However, we would consider this a surprise given the absence of oscillations at low accretion rates in KS 1731−260 and 4U 1728−34. On the other hand, the time scales of bursts from the slow oscillators 4U 1916−053 (Swank, Taam, & White 1984) and 4U 1702−429 (Makishina et al., 1982) have not been observed to vary systematically with the persistent flux, so we cannot predict how observing bursts at low $\dot{M}$ in slow sources would affect our correlations.

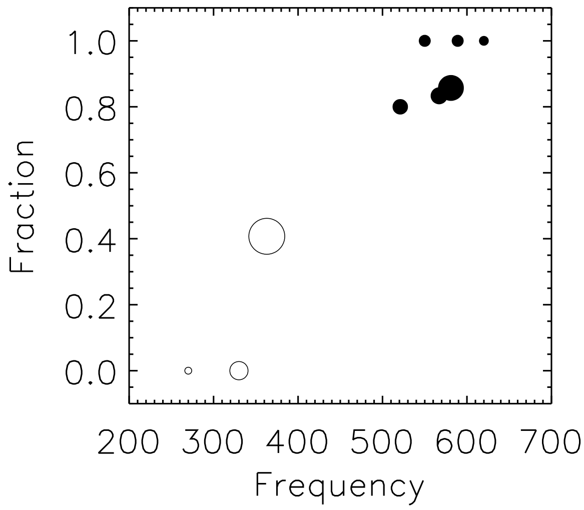

Figure 7-2 The fraction of bursts with oscillations that are also radius expansion bursts, plotted as a function of source oscillation frequency. Open circles denote slow ($n = 1$) oscillation sources, while solid circles denote fast ($n = 2$) oscillation sources. The size of the circle indicates the number of bursts with oscillations observed for each source.

7.3 Discussion

We have found that oscillations from the 6 fast burst oscillation sources are tightly connected to photospheric radius expansion, whereas oscillations from the 3 slow sources are about equally likely to be found in bursts both with and without radius expansion. What drives this correlation remains to be determined: is it the burst properties themselves, the oscillation frequencies, or some unseen third parameter?

According to the beat frequency model of kHz QPOs, the fact that $\nu_{\rm burst} \simeq \Delta\nu_{\rm kHz}$ for the "slow" sources whereas $\nu_{\rm burst} \simeq 2\Delta\nu_{\rm kHz}$ for the "fast" ones can be accounted for if one or two antipodal hot spots on the surface of the rotating neutron star are visible to the observer (Miller et al. 1998). One possibility is that the distinction between fast and slow oscillations is due to a difference in the orientation of the hot spots and the observer with respect to the rotation axis of the star (Section 5.3.2). This seems unlikely. Radius expansion is observed with similar likelihood from both fast and slow sources, and therefore is unlikely to depend on our viewing angle. We would not expect oscillations to be associated with radius expansion bursts only in the fast sources if the viewing angle determines whether one or two spots are observed.

It also does not appear that the strengths of the bursts determine the oscillation frequencies by igniting either one or two hot spots. If this were the case, one would expect to detect slow oscillations during weak bursts without radius expansion from the fast sources, and fast oscillations during strong bursts from the slow sources. Out of the 125 bursts we observed from sources of burst oscillations, we find no evidence for harmonic or half-frequency signals with powers comparable to the signals at the frequencies in Table 7.1 (Chapter 2.2.1 and Figure 5-2).

If the distinction between slow and fast oscillators is equivalent to a division between slow and fast rotators, $\nu_{\rm spin}$ (or some related quantity, e.g., the effective surface gravity) could determine which bursts show oscillations. However, that option is not free of complications, as the transition between the burst properties for sources that exhibit fast and slow oscillations must be very sharp, since the two populations are not at all well separated in frequency (see Table 7.1). When comparing the observed distribution of $\nu_{\rm burst}$ to a uniform distribution of frequencies between 250–650 Hz, a Kolmogorov-Smirnov test (e.g., Eadie et al. 1971) can exclude a uniform distribution at only the 1.3σ (81%) confidence level. It is interesting to note that the recent report of a possible ≈ 400 Hz burst oscillation from the 401 Hz pulsar SAX J1808.4$-$3658 (in 't Zand et al. 2001) would make the $\nu_{\rm burst}$ distribution even more consistent with a uniform distribution (excluded at only the 0.9σ or 64% confidence level), so the putative transition would have to be correspondingly sharper.

We have listed a few additional properties of these LMXBs in Table 7.1. Neither the activity level nor the long-term average accretion rate $< \dot{M} >$, as determined from nearly 5 years of data from the *RXTE* All-Sky Monitor (Levine et al. 1996), appears to be correlated with the frequencies of the burst oscillations. Fast oscillations are observed in both transient (4U 1608$-$522 and Aql X-1) and persistent (e.g., 4U 1636$-$536) sources, as well as from both low $< \dot{M} >$ and high $< \dot{M} >$ sources. Orbital periods are measured for only 4 of the 9 sources, and range from 0.81 to 19 hours. It is apparent that these burst oscillation sources are an inhomogeneous group, which makes measurements of oscillations from other sources highly desirable.

We feel that the most likely explanation for the observed correlations is that the burst properties change differently as a function of $\dot{M}$ in fast and slow sources. X-ray burst theory predicts that radius expansion should occur only at low $\dot{M}$ (Fujimoto, Hanawa, & Miyaji 1981; Ayasli & Joss 1982). This agrees with observations of the slow oscillator 4U 1728$-$34 (Franco 2000; van Straaten et al. 2000), but does not appear to hold true for the fast oscillators KS 1731$-$260 (Muno et al., 2000), 4U 1608$-$522 (Murakami et al., 1980), and 4U 1636$-$536 (van der Klis et al., 1990). If oscillations only appear at high $\dot{M}$ (as suggested by Franco 2001), then they would indeed be associated with radius expansion in the fast sources, but not the slow sources. Furthermore, Bildsten (2000) has suggested that some mechanism acts in these latter sources to confine the accreted material such that the *local* $\dot{M}$ can decrease even as the global $\dot{M}$ increases. If this is true, such confinement is somehow related to the higher frequency of the fast burst oscillations.

Chapter 8

Summary

Although it has long been expected that pulsations should occur at the spin frequency of a neutron star as it undergoes a thermonuclear X-ray burst (Schoelkopf & Kelley, 1991), the persistence and frequency evolution of the observed oscillations is surprising. Several models have been proposed to explain these aspects of the burst oscillations (Strohmayer et al., 1997b; Spitkovsky et al., 2002; Heyl, 2002), each of which suggest that a pattern forms in the surface brightness of the rotating neutron star. To explain the upward frequency drift (Chapter 2), the pattern must move opposite the rotation of the star with a velocity that decreases as the burst decays, so that the observed frequency increases at first, and then saturates near that of the stellar spin.

The coherence and stability of the oscillations (Chapter 3) provides compelling evidence that the asymptotic frequencies of the oscillations represent the stellar spin. However, there is residual dispersion in the frequencies from 4U 1636−536 that can not be explained by mechanisms that ordinarily operate in pulsars. In particular, the dispersion is uncorrelated with the expected Doppler motion of the binary, and the next largest effect, accretion torque, is several orders of magnitude too small. Moreover, 30% of the oscillations exhibit evidence for either discrete phase jumps, sudden frequency changes, or two signals that are present simultaneously within < 1 Hz. This instability points toward models in which the velocities of the brightness patterns are highly sensitive to the properties of the stellar surface — e.g., its composition, temperature, and density (Spitkovsky et al., 2002; Heyl, 2002).

Given that the properties of the surface layer should greatly influence the oscillations, it is somewhat surprising that no correlation is apparent between the frequencies and amplitudes of the oscillations and the time scales, temperatures, and intensities of the bursts (Chapter 4). It is possible that this is because the emission during the burst is so dramatically altered by scattering in the stellar atmosphere that the conditions on the surface are obscured. However, if the amplitude and frequency of the oscillations are most sensitive to the composition and vertical structure of the burning layer, then we probably should not expect obvious correlations with the flux from the photosphere. Instead, the oscillations themselves could be the best probe of the structure of the degenerate ocean on the neutron star. Of course, to use the oscillations as a probe, we must understand how they are generated.

The best constraints on the models for producing oscillations are from their surprisingly sinusoidal profiles (Chapter 5). Geometric, Doppler, and time delay effects all generally produce asymmetric profiles that should be easily detectable by searching for harmonics of the main signals. The lack of harmonic content — less than 5–10% of the amplitude of the main signal — indicates that the brightness patterns are quite symmetric. This favors models in which the oscillations originate from global oscillation modes in the density of the neutron star ocean (Heyl, 2002). However, how such density variation can be translated into a brightness contrast has yet to be determined.

Information on the surface layers can also be obtained from examining in which bursts the oscillations occur. Oscillations are observed in less than half of the bursts from a given source, preferably in bursts that occur when the persistent accretion rate is high ($\sim$0.1 $\dot{M}_{\rm Edd}$). Theoretical models predict that the composition of the burning layer should change dramatically as the accretion rate onto the surface varies, which causes the time scales, intensities, and fluences of the bursts to change as well. Oscillations from KS 1731$-$260 tend to occur exclusively during fast, radius expansion bursts, which suggests that the burning layer must consist largely of helium to produce oscillations (Chapter 6).

However, observations of other the sources contradict this suggestion. Instead, it appears that fast (500-600 Hz) oscillations occur preferentially during bursts with radius expansion episodes, while slower (200–400 Hz) oscillations exhibit no such preference (Chapter 7). This suggests that the properties of the bursts change differently as a function of the accretion rate in these two groups of sources, due to some physical difference that also determines the frequency of the oscillations. The origin of this correlation is unclear. Studies of other burst sources will provide a better understanding of how the accretion rate affects the properties of bursts.

As an aside, there is one question that has bothered the LMXB community for several years, and may remain unanswerable for a while. The conjecture that the $\sim$ 600 Hz oscillations occur at $2 \times \nu_{\rm spin}$ is a critical component of the beat frequency model for the kHz QPOs. It can be argued that the lack of a half-frequency signal from any of the sources examined in this thesis does not resolve the controversy as to whether some of the faster oscillations occur at twice the spin frequency of the neutron star. The obstacle to such a conclusion is the fact that the one reported case of a half-frequency signal occurred during the rise of a burst, when the oscillations could be produced by a localized burning region (Miller, 1999). Oscillations later in the burst, which were the focus of this work, may be produced by a separate mechanism that naturally produces symmetric, antipodal bright regions. This leaves room for the $2 \times \nu_{\rm spin}$ model to wiggle, but only just a bit. In the same way, the lack of a half-frequency signal at the 10% level in an oscillation observed by Strohmayer & Markwardt (2002) during an hour-long "superburst" does not solve the issue. Unfortunately, while another detection of a half-frequency signal would confirm the validity of the first, further non-detections can only produce doubt, but no resolution.

Although I believe that this thesis has provided a comprehensive analysis of burst oscillations as observed with the *RXTE* PCA, there is clearly more to do for the future. Observational breakthroughs may still occur, particularly in understanding why oscillations are not observed from every burst. I am currently examining the energy dependence of the oscillations. Other interesting questions include whether the oscillations evolve differently as a function of photon energy, or what the time scales are at which the apparent phase jumps occur. Most importantly, a solid theoretical model must be established for understanding burst oscillations. With such a model, it will be feasible to study the surface layers of the neutron star in a quantitative manner, and it may be possible to constrain the mass and radius of the neutron stars.

Appendix A

Oscillations from the Surface of a Neutron Star

Four effects must be taken into account when simulating the emission that the observer sees from a bright region on the surface of a rapidly rotating neutron star: (*i*) the geometric occultation of the bright region, (*ii*) the bending of photon paths in a general relativistic metric, (*iii*) Doppler modifications of the emergent spectrum due to the large surface velocity, and (*iv*) time delays due to the finite velocity of the photons and the bright region with respect to the observer.

A.0.1 Geometric Effects

First, the solid angle that the bright region subtends changes as the anisotropy rotates with the neutron star, and the observer receives no flux when the emitting region passes behind the limb of the neutron star. As this geometric effect is the largest factor in determining the amplitudes of any oscillations, it is instructive to examine it in detail in the absence of gravitational, Doppler, and time delay effects.

The flux that an observer sees from a solid angle on the sky is defined as $dF_\nu = I_\nu d\Omega$, where I_ν is the specific intensity of a region of the sky. This needs to be related to the flux from the surface of the neutron star. The solid angle on the sky is related to the area on the surface by

$$D^2 d\Omega = R^2 \cos\delta dA = R^2 \cos\delta \sin\theta d\theta d\phi \tag{A.1}$$

where D is the distance from the star to the observer, R is the radius of the star, dA is a unit area on the surface, and δ is the angle between the normal to the surface and the observer's line of sight. The specific intensity at the surface of the star, $I_n u(\theta, \phi, \delta)$ is a function of the position on the star, θ and ϕ, and the angle from the normal to the surface at which the photon was emitted, δ. In flat space-time, $\delta = \theta$ for an observer far from the surface, since the emitted photons follow parallel paths to the observer. We will generally keep an explicit dependence on δ in I_ν, since we will be working in a curved space-time later. Thus, the received flux from the surface is can be related to the flux emerging from the surface by

$$dF_\nu = I_\nu(\theta, \phi, \delta) \frac{R^2}{D^2} \cos\theta \sin\theta d\theta d\phi, \tag{A.2}$$

This can be integrated over the visible surface of the neutron star.

In order to produce flux oscillations when the star is rotating, I_ν must vary as a function

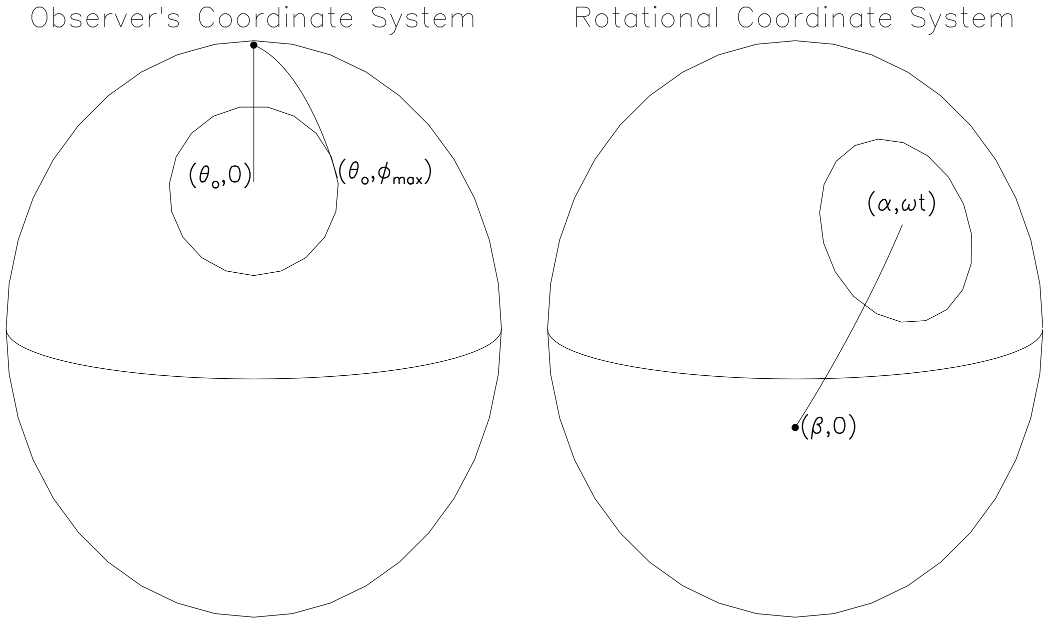

Figure A-1 Simple illustrations of the two coordinate systems used throughout this section. *Left*: In the observer's coordinate system, the line-of-sight is along $\theta = 0$, and the spot is located at $\theta = \theta_o$ and $\phi = 0$. This is the easiest coordinate system in which to compute both the flux from the spot and the paths of photons that reach the observer. *Right*: In the rotational coordinate system, the spin axis of the neutron star is oriented along $\theta = 0$. The position and velocity of the spot is most easily calculated in this frame. In both cases, the point at which the line-of-sight to the center intersects the surface is indicated by a dot.

of the position on the surface (θ and ϕ). My model for such a brightness asymmetry will be a circular region of size ρ with a uniform temperature T and centered an angle θ_o from my line of sight. I will work in a coordinate system in which the observer is along the $\hat{z}$ ($\theta = 0$) direction, as indicated by the observer's coordinate system in Figure A-1. To compute the flux from the bright region, I integrate over all values of θ and ϕ within the spot. My bounds on θ are $\theta_{\rm min} = \max(\theta_o - \rho, 0)$, since $0 < \theta < \pi$ in spherical coordinates, and $\theta_{\rm max} = \min(\theta_o + \rho, \pi/2)$, so that I do not include the flux from the spot if it is behind the limb of the neutron star ($\theta > \pi/2$). For each θ, the range of ϕ in which I am interested is given by considering the angular displacement ρ between the center of the spot, $\vec{A}$, and the point where the circle of constant θ intersects the circle of radius ρ, $\vec{B}$. These vectors are given by

$$\begin{aligned} \vec{A} &= (1, \theta_o, 0) = [\sin\theta_o, 0, \cos\theta_o] && \text{(A.3)} \\ \vec{B} &= (1, \theta, \phi_{\rm max}) = [\sin\theta\cos\phi_{\rm max}, \sin\theta\sin\phi_{\rm max}, \cos\theta] && \text{(A.4)} \end{aligned}$$

where I use curved parenthesis to denote the position in spherical coordinates, and square brackets to denote the position in Cartesian coordinates. To solve for $\phi_{\rm max}$, I will use the fact that the angle between $\vec{A}$ and $\vec{B}$ is ρ. Therefore, the dot-product $\vec{A} \cdot \vec{B} = \cos\rho$, so that

$$\cos\phi_{\rm max} = \frac{\cos\rho - \cos\theta\cos\theta_o}{\sin\theta\sin\theta_o}. \tag{A.5}$$

I can integrate Equation A.2 with these limits on θ and ϕ to get

$$F_\nu = \frac{R^2}{D^2}\int_{\theta_{\rm min}}^{\theta_{\rm max}}\int_{-\phi_{\rm max}}^{\phi_{\rm max}} I_\nu(\theta, \phi, \delta)\cos\theta\sin\theta d\theta d\phi \tag{A.6}$$

I have taken the spot to have a specific intensity that is not dependent on θ and ϕ, $I_\nu(\delta)$. Fortunately, δ varies only with θ, so the ϕ integral is simply $2\phi_{\rm max}$. Therefore, the total flux is

$$F_\nu = 2\frac{R^2}{D^2}\int_{\theta_{\rm min}}^{\theta_{\rm max}} I_\nu(\delta)\cos\theta\sin\theta\cos^{-1}\left(\frac{\cos\rho - \cos\theta\cos\theta_o}{\sin\theta\sin\theta_o}\right)d\theta. \tag{A.7}$$

When I rotate the neutron star, I need to compute how the angle between the center of the spot and the observer's line-of-sight, θ_o, varies as a function of the rotational phase, Ωt. Switching to the frame in which the spin of the star is along the $\hat{z}$-direction (the rotational coordinate system in Figure A-1), I consider the spot centered at a position angle $\theta = \alpha$ and $\phi = \Omega t$, and the observer's line-of-sight along $\theta = \beta$ and $\phi = 0$. The angle between the two, θ_o is found by converting the corresponding coordinates to a Cartesian system and taking a dot product, as in Equation A.5:

$$\cos\theta_o = \sin\alpha\sin\beta\cos\Omega t + \cos\alpha\cos\beta \tag{A.8}$$

I can now calculate Equation A.7 as θ_o varies with time to produce the light curve from a spot on a rotating neutron star.

In Figure A-2, I have illustrated a light curve from two circular spots of size $\rho = 60°$ located at $\alpha = 75°$ and $105°$ from the rotational axis (*solid line*). They are viewed at $\beta = 60°$ from the pole. Two peaks, one from each spot, are clearly seen, with the spot that is nearer to the observer's line of sight producing the larger peak.

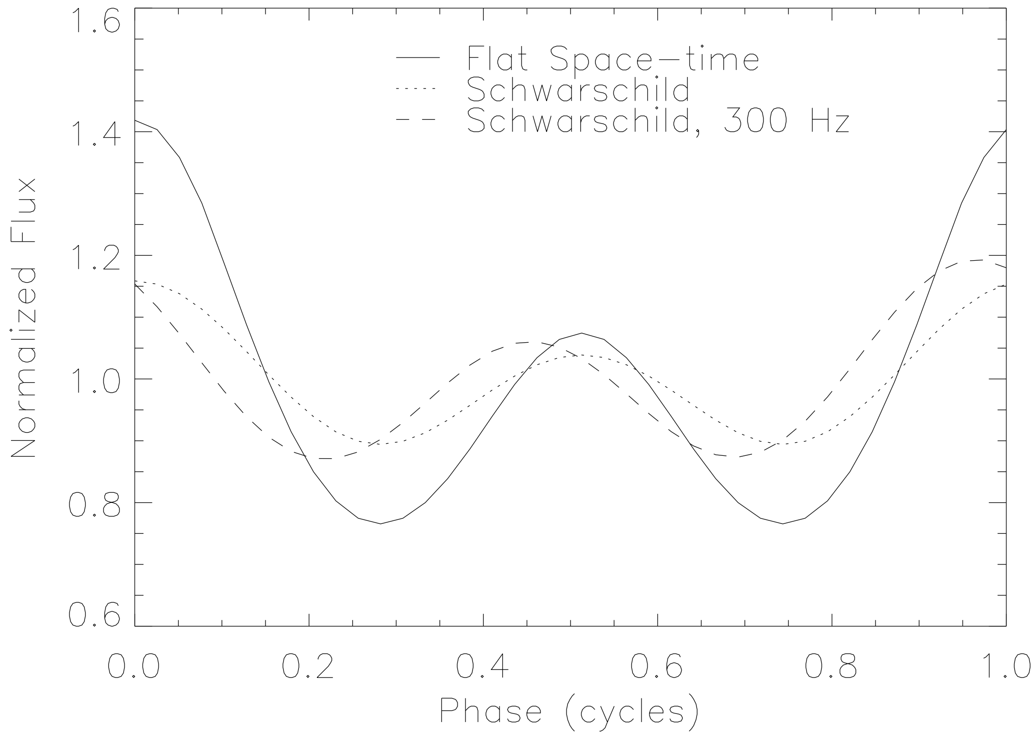

Figure A-2 General relativistic and Doppler effects modify the pulse profile from a spinning neutron star. These light curves were produced from two $\rho = 60°$ bright regions located at $\alpha = 75°$ and $105°$ from the rotational axis. They were viewed at $\beta = 60°$ from the pole.

A.0.2 General Relativistic Effects

The space-time curvature induced by the mass of the neutron star bends the paths of photons as they propagate toward the observer (Pechenick et al., 1983). The Schwarzschild metric can be written as (Price, 1982),

$$ds^2 = -\left(1-\frac{2M}{r}\right)dt^2 + \left(1-\frac{2M}{r}\right)^{-1}dr^2 + r^2(d\theta^2+\sin^2\theta d\phi^2). \tag{A.9}$$

Since the metric has no dependence on t or ϕ, I can compute two constants of motion instantly: the energy $p_t \equiv -E$ and angular momentum $p_\phi \equiv L$ of the photon. (There is a third constant of motion as well, but it is not needed.) From these constants I can compute the measured parameters

$$p^t = \left(1-\frac{2M}{r}\right)^{-1}E \tag{A.10}$$

$$p^\phi = \frac{L}{r^2\sin^2\theta}. \tag{A.11}$$

If I restrict myself to the $\theta=\pi/2$ plane, from the spherical symmetry of the metric I further know that $p^\theta=0$. Finally, since I know that $p^\mu p_\mu=0$, I can solve for p^r using the equation

$$0 = \frac{b^2}{r^2} + (p^r)^2\left(1-\frac{2M}{r}\right)^{-1} - \left(1-\frac{2M}{r}\right)^{-1}. \tag{A.12}$$

I have defined $b=L/E$ as the impact parameter of the photon, which indicates the direction of the photon when it reaches the observer. Considering b allows me to determine which photons reach the observer, and greatly simplifies computing the total flux at the observer. Solving for p^r, and combining with the other components of the momentum,

$$\frac{dr}{d\lambda} \equiv p^r = \left\{1-\frac{b^2}{r^2}\left(1-\frac{2M}{r}\right)\right\}^{1/2} \tag{A.13}$$

$$\frac{dt}{d\lambda} \equiv \frac{p^t}{E} = \left(1-\frac{2M}{r}\right)^{-1} \tag{A.14}$$

$$\frac{d\phi}{d\lambda} \equiv \frac{p^\phi}{E} = \frac{b}{r^2}, \tag{A.15}$$

where λ is an affine parameter.

For each impact parameter, I need to find the angle $\Delta\phi$ at which the photon impacts the neutron star by combining the equations for p^r and p^ϕ:

$$\Delta\phi = b\int_R^\infty r^{-2}\left\{1-\frac{b^2}{r^2}\left(1-\frac{2M}{r}\right)\right\}^{-1/2}dr \tag{A.16}$$

The maximum impact parameter at which the photon hits the neutron star can be found from the condition that $dr/d\lambda$ be real when the photon hits the surface:

$$\frac{R^2}{b^2}\left(1-\frac{2M}{R}\right) \le 1 \tag{A.17}$$

$$b_{\max} = R\left(1 - \frac{2M}{R}\right)^{-1/2}. \tag{A.18}$$

The maximum impact parameter increases as the mass of the star grows, given a fixed radius (top panel of Figure A-3). A more massive star appears to have a larger radius than the coordinate R. I can then define a compactness, $p = R/2M = R/R_{\rm Sch}$, and make a coordinate transformation in Equation A.16, $u = M/r$, and to obtain a simplified expression

$$\Delta\phi = \int_0^{2/p} \left\{\frac{M^2}{b^2} - u^2(1-2u)\right\}^{-1/2} du. \tag{A.19}$$

This integral must be evaluated numerically. Note that there is a singularity in the integrand when $b = b_{\max}$, which I can avoid by another coordinate transformation ($\xi = [M/R - u]^{1/2}$). To compute the trajectory of a photon in an arbitrary θ-plane, I simply take advantage of the spherical symmetry of the Schwarzschild metric to re-define that θ-plane as the $\theta = \pi/2$ plane.

The photon that reaches the observer at $\phi = 0$ from the largest $\Delta\phi_{\max}$ has an impact parameter $b_{\max}$. We have illustrated how $\Delta\phi_{\max}$ varies with the compactness of the star p in the bottom panel of Figure A-3. It is evident that the observer sees behind the limb of the neutron star, which would be at $\Delta\phi = 90°$ in Euclidean space, even for stars that are not very compact (large p). For very compact stars ($p < 1.75$), an observer always sees the entire surface of the star ($\Delta\phi > \pi$). This is illustrated by Figure A-4, in which we plot an image of a hot region on a neutron star as observed through a flat space-time and a Schwarzschild metric.

I now can calculate the flux that the observer sees from the relativistic star per unit solid angle. This is most simply computed in a coordinate system centered on the neutron star with the observer located at $\theta = 0$ (Figure A-1, *left*). Following (Pechenick et al., 1983), I define the solid angle on the observer's sky as

$$d\Omega' = \sin\theta' d\theta' d\phi' \approx \theta' d\theta' d\phi' \tag{A.20}$$

since θ' is infinitesimally small for an observer very far away from the neutron star. Space-time at the observer is flat, so the impact parameter is given by $b = D\theta'$. The relationship between b at the observer and θ on the neutron star is given by Equation A.19, where I have (somewhat confusingly) re-named $\Delta\phi$ as θ. Due to the spherical symmetry of the problem, $\phi' = \phi$, and I can orient the $\phi = 0$ direction through the center of the hot spot. Therefore, I find

$$d\Omega' = \frac{1}{D^2} b\ db\ d\phi. \tag{A.21}$$

The specific intensity at infinity is affected by gravitational red-shift, so that $I'_\nu(b,\phi) = (1 - 2M/R)^{3/2} I_\nu(\theta, \phi, \delta)$. The three factors of $(1 - 2M/R)^{1/2}$ result from the red-shifting of (*i*) the apparent angular size of the spot, (*ii*) the arrival rate of the photons, and (*iii*) the energy interval in which the photons are counted. The δ in the argument of the specific intensity represents the angular dependence of the intensity at any point on the surface. The angle δ is given by (see Pechenick et al., 1983):

$$\sin\delta = (b/R)(1 - 2M/R)^{1/2} = b/b_{\max}. \tag{A.22}$$

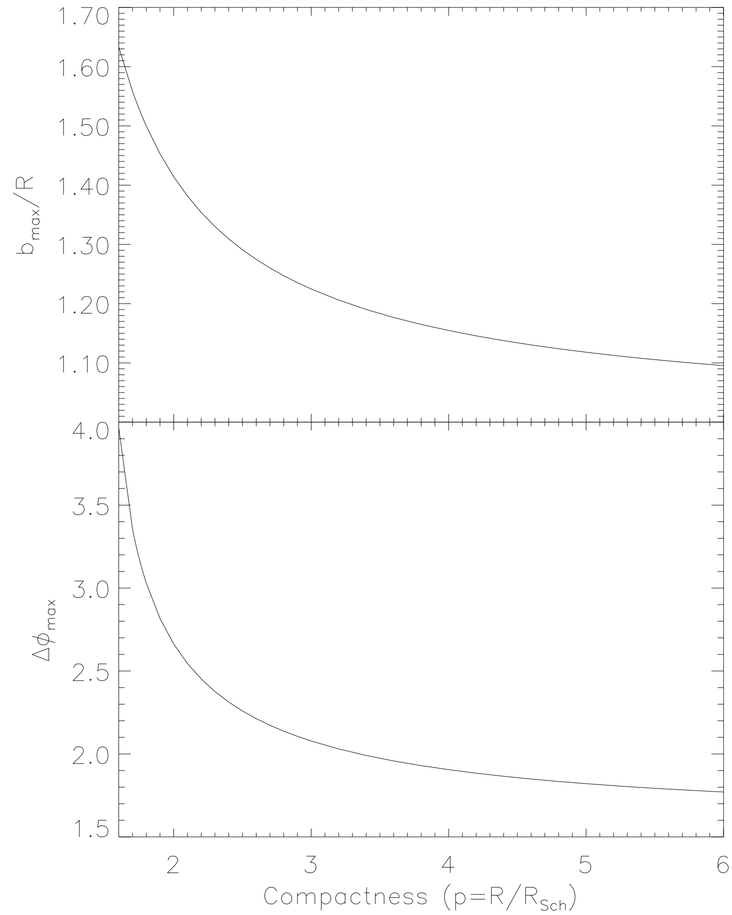

Figure A-3 Plots illustrating how the compactness of the neutron star p affects the curvature of photon paths. (*Top panel*): the maximum impact parameter $b_{\max}$ of a photon that leaves the neutron star as a function of p. (*Bottom panel*): the maximum angle $\Delta\phi_{\max}$ from which a photon can leave the star and reach an observer at $\phi = 0$ versus p.

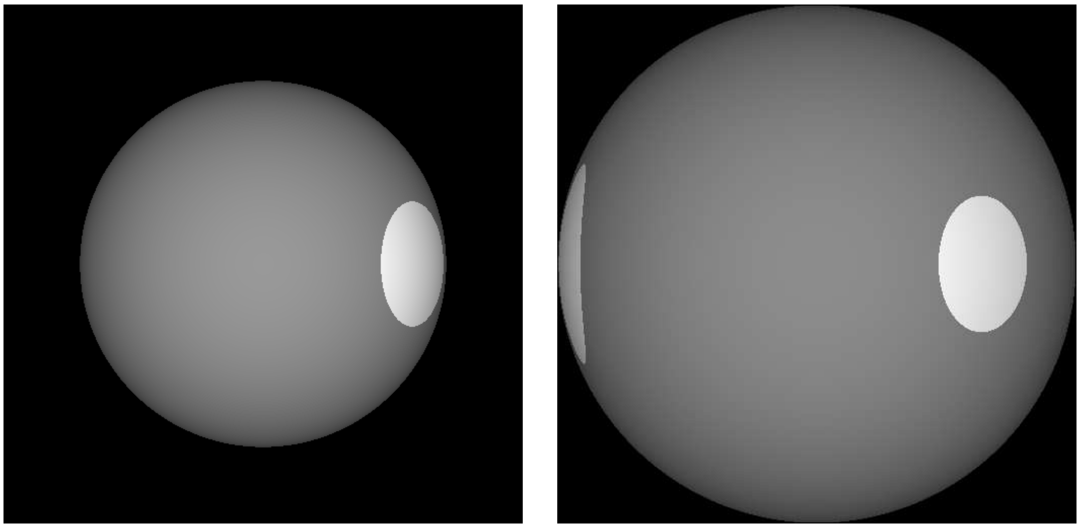

Figure A-4 Two images of a neutron star. *Left Panel*: The intensity distribution in Euclidean space on a neutron star with two hot spots of size $\rho = 20^\circ$, located at $\alpha = \beta = 90^\circ$, and with phases $\phi = 60^\circ$ and 240°. The second spot can not be seen. *Right Panel*: The same intensity distribution observed through a Schwarzschild metric with $p = 2$. Notice that the star looks larger, because photons reach the observer with larger impact parameters. The observer can also see behind the limb of the neutron star, so that the second spot is visible.

In total,

$$dF_\nu = I'_\nu(b,\phi)d\Omega' = \frac{1}{D^2}(1-2M/R)^{3/2} I_\nu[\theta(b),\phi,b/b_{\max}]b\;db\;d\phi, \tag{A.23}$$

which can be integrated over b and ϕ.

The range of ϕ over which I must integrate the flux is found from Equation A.5, where θ is the function of b from Equation A.19. I can simultaneously encode the $\theta(b)$ and ϕ bounds for the integral into a single function:

$$h[\theta;\theta_o] = \begin{cases} \int_{-\phi_{\max}}^{\phi_{\max}} I_\nu(\theta,\phi,\delta)d\phi & \text{if } \theta_o - \rho < \theta < \theta_o + \rho \\ 0 & \text{otherwise} \end{cases}, \tag{A.24}$$

since $\phi_{\max}$ is a function of θ and θ_o. I have written the ϕ integrand this way, because when I take into account Doppler effects below, the velocity, and therefore I_ν, is a function of ϕ. This is a departure from Pechenick et al. (1983). The integral over θ is now straightforward:

$$F_\nu = \left(\frac{R}{D}\right)^2 \left(1-\frac{2M}{R}\right)^{3/2} \int_0^{b_{\max}} h[\theta(b);\theta_o]\frac{1}{R^2}bdb \tag{A.25}$$

Note that this has one fewer $(1-2M/R)^{1/2}$ term than in Pechenick et al. (1983), because I have computed the flux per unit energy rather than the bolometric flux.

In Figure A-2, the dotted line illustrates the light curve from two hot spots after the photons have been propagated through the Schwarzschild metric with $p = 2.0$. Since more of the neutron star is visible at any given phase, the amplitude of the oscillation is reduced significantly.

A.0.3 Doppler Effects

For an anisotropy on a rapidly rotating neutron star, Doppler effects are also important — a 10 km neutron star spinning at 500 Hz has a surface velocity of 0.1c. However, the spherical symmetry that I used to compute the photon trajectory (Equation A.19) is not present in the velocity field of the neutron star surface, which has the form

$$\vec{v} = v_o \sin\theta \; \hat{\phi}. \tag{A.26}$$

Here, the $\theta = 0$ direction is aligned with the spin axis ($\hat{\Omega}$). The velocity of the spot relative to a stationary observer above the neutron star equator is given by

$$v_o = \left(1 - \frac{2M}{R}\right)^{-1/2} R\,\Omega, \tag{A.27}$$

since the observer has a non-zero four-velocity (Price, 1982, Equation 6.28). As a result, to compute the Doppler modifications of the emission from the surface, I must know where the photon lands, the four-momentum of the photon, and the surface velocity.

I know the position and four-momentum of the photon in the frame in which the observer is along $\hat{z}$ (Equation A.22 and the left panel of Figure A-1), but I know the surface velocity in the frame where $\hat{z} = \hat{\Omega}$ (Equation A.26 and the right panel of Figure A-1). Thus, I must find the coordinate transformation (and its inverse) from the frame in which the anisotropy is centered at

$$\vec{A} = (1, \alpha, \Omega t) = [\sin\alpha\cos\Omega t, \sin\alpha\sin\Omega t, \cos\alpha] \tag{A.28}$$

into the frame at which the anisotropy is centered at

$$\vec{B} = (1, \theta_o, 0) = [\sin\theta_o, 0, \cos\theta_o], \tag{A.29}$$

where θ_o is given by Equation A.8. To find this transformation, I first rotate $\vec{A}$ about the $\hat{y}$ direction to place the anisotropy in the plane where $\theta = \theta_o$ ($z = \cos\theta_o$), and then by rotating about the $\hat{z}$ direction so that the anisotropy is located at $\phi = 0$. The two rotations turn out to be

$$R_y = \begin{pmatrix} \cos\beta & 0 & -\sin\beta \\ 0 & 1 & 0 \\ \sin\beta & 0 & \cos\beta \end{pmatrix}, \tag{A.30}$$

which centers the spot on $z = \cos\theta_o$, and

$$R_z = \begin{pmatrix} \cos\chi & \sin\chi & 0 \\ -\sin\chi & \cos\chi & 0 \\ 0 & 0 & 1 \end{pmatrix}. \tag{A.31}$$

in which

$$\sin\chi = \frac{v\sin\theta_o}{u^2 + v^2} \tag{A.32}$$

$$\cos\chi = \frac{u\sin\theta_o}{u^2 + v^2}, \tag{A.33}$$

where u and v are given by $R_y\vec{A} = [u, v, \cos\theta_o]$.

The rotation $R_z R_y$ above allows me to choose coordinates in which I can compute the

Lorentz transformation from the observer's rest frame into the spot's instantaneous rest frame. Then, I can find the energy of the photon and the angle with which the photon left the surface in the rest frame of the spot, in order to compute the specific intensity in the frame of the spot where my emission model is defined. The energy of the photon in the rest frame of the anisotropy (p_o^{rest}), is related to the four-momentum in the observer's frame ($\vec{p}$) by

$$p_o^{\text{rest}} = \gamma(p_o - \vec{\beta} \cdot \vec{p}). \tag{A.34}$$

The angle with respect to the normal at which the photon leaves the anisotropy in its rest frame (δ^{rest}) is found by computing the vector momentum

$$\vec{p}^{\text{ rest}} = \vec{p} + \frac{\gamma - 1}{\beta^2}(\vec{\beta} \cdot \vec{p})\vec{\beta} - \gamma\vec{\beta}p_o, \tag{A.35}$$

from which I can get

$$\cos\delta^{\text{rest}} = \frac{\vec{p}^{\text{ rest}} \cdot \hat{r}}{p_o^{\text{rest}}}. \tag{A.36}$$

This last computation in particular leads us to transform the velocity field into the observer's frame, since that is where I know the angle that the photon momentum makes with respect to the normal.

Finally, I can compute the factor by which the intensity is boosted from the hot spot frame into the observer's frame

$$I_\nu(\theta, \phi, \delta) = \left(\frac{\nu}{\nu^{\text{rest}}}\right)^3 I_{\nu^{\text{rest}}}(\theta, \phi, \delta^{\text{rest}}). \tag{A.37}$$

The three factors of ν/ν^{rest} account for Doppler beaming, time dilation, and Doppler shift of the energy interval. This gives us the specific intensity at the neutron star's surface in a non-rotating frame for Equation A.24.

A.0.4 Time Delays

Finally, with a surface velocity of 0.1c, the anisotropy essentially keeps up with the photons it has just emitted if it is moving toward the observer, compressing the observed pulse. Likewise, the trailing edge of the pulse is extended as the spot moves away from the photons just emitted. I can compute this effect by considering the time difference δt for the photon paths to $\Delta\phi = 0$ and $\Delta\phi \neq 0$.

$$dt = \int_{R_{\text{NS}}}^{50R_{\text{NS}}} \left(1 - \frac{2M}{r}\right)^{-1} \left\{1 - \frac{b^2}{r^2}\left(1 - \frac{2M}{r}\right)\right\}^{-1/2} dr \tag{A.38}$$

For two photons which reach the observer simultaneously, the anisotropy will be centered at an angle $\phi = \phi_o$ when a photon leaves from $\Delta\phi = 0$, but the anisotropy will be at $\phi = \phi_0 + \Omega\delta t$ when the photon leaves from $\Delta\phi \neq 0$. I have used a retarded time $t' = t - \delta t$ to compute θ_o for each t and b in Equations A.8 and A.25 to account for the time delay.

In Figure A-2, the dashed line illustrates the light curve from two hot spots including the cumulative effects of light bending, Doppler effects, and time delays for a neutron star with mass $M = 1.4\ M_\odot$, compactness $p = 2.0$, and spin $\Omega = 600$ Hz. The Doppler and time delay effects increase the maxima of the oscillation, by (*i*) boosting the intensity as the spot is moving toward the observer, and (*ii*) causing the photons to be received in a shorter, more intense pulse because the spot keeps pace with the photons it has emitted. The minima are deepened as the spot rotates away from the observer, because the emission is de-boosted. This results in an oscillation with a higher amplitude and a narrower profile.

Bibliography

Alpar, M. A., Cheng, A. F., Ruderman, M. A., & Shaham, J. (1982). A new class of radio pulsars. *Nature*, **300**, 728.

Ayasli, S. & Joss, P. C. (1982). Thermonuclear processes on accreting neutron stars - A systematic study. *The Astrophysical Journal*, **256**, 637.

Balbus, S. A. & Hawley, J. F. (1992). A Powerful Local Shear Instability in Weakly Magnetized Disks. IV. Nonaxisymmetric Perturbations. *The Astrophysical Journal*, **400**, 610.

Barret, D., Olive, J. F., Boirin, L., Done, C., Skinner, G. K., & Grindlay, J. E. (2000). Hard X-Ray Emission from Low-Mass X-Ray Binaries. *The Astrophysical Journal*, **533**, 329.

Basinska, E. M., Lewin, W. H. G., Sztajno, M., Cominsky, L. R., & Marshall, F. J. (1984). X-ray observations of the burst source MXB 1728–34. *The Astrophysical Journal*, **281**, 337.

Bevington, P. R. (1969). *Data Reduction and Error Analysis for the Physical Sciences*. McGraw-Hill, New York.

Bhattacharya, D. (1995). Millisecond pulsars. In *X-ray Binaries*, Lewin, W. H. G. and van Paradijs, J. and van den Heuvel, E. P. J., editors, Cambridge University Press, 233.

Bildsten, L. (1995). Propagation of nuclear burning fronts on accreting neutron stars: X-ray bursts and sub-hertz noise. *The Astrophysical Journal*, **438**, 852.

Bildsten, L. (1997). Thermonuclear burning on rapidly accreting neutron stars. In *The Many Faces of Neutron Stars*, R. Buccheri, J. van Paradijs, and M. A. Alpar, editors, number 515 in NATO ASI Series C, Kluwer Academic Publishers, 337.

Bildsten, L. (1998). Gravitational Radiation and Rotation of Accreting Neutron Stars. *The Astrophysical Journal*, **501**, L89.

Bildsten, L. (2000). Theory and observations of type i x-ray bursts from neutron stars. In *Cosmic Explosions*, S. S. Holt and W. W. Zhang, editors, AIP.

Bradt, H. V., Rothschild, R. E., & Swank, J. H. (1993). X-ray timing explorer mission. *Astronomy and Astrophysics Supplement*, **97**, 355.

Braje, T. M., Romani, R. W., & Rauch, K. P. (2000). Light Curves of Rapidly Rotating Neutron Stars. *The Astrophysical Journal*, **531**, 447.

Chakrabarti, S. & Titarchuk, L. G. (1995). Spectral Properties of Accretion Disks around Galactic and Extragalactic Black Holes. *The Astrophysical Journal*, **455**, 623.

Chandrasekhar, S. (1960). *Radiative Transfer*, Dover, 76.

Chevalier, C. & Ilovaisky, S. A. (1991). Discovery of a 19-hour period in Aquila X-1. *Astronomy and Astrophysics*, **251**, L11.

Christian, D. J. & Swank, J. H. (1997). The Survey of Low-Mass X-Ray Binaries with the Einstein Observatory Solid-State Spectrometer and Monitor Proportional Counter. *The Astrophysical Journal Supplement*, **109**, 177.

Clark, G. W., Li, F. K., Canizares, C., Hayakawa, S., Jernigan, G., & Lewin, W. H. G. (1977). Further observations of recurrent X-ray bursts from the globular cluster NGC 6624. *Monthly Notices of the Royal Astronomical Society*, **179**, 651.

Cominsky, L. R. & Wood, K. S. (1984). Discovery of a 7.1 hour period and eclipses from MXB 1659–29. *The Astrophysical Journal*, **283**, 765.

Cumming, A. & Bildsten, L. (2000). Rotational Evolution during Type I X-Ray Bursts. *The Astrophysical Journal*, **544**, 453.

Cumming, A., Morsink, S. M., Bildsten, L., Friedman, J. L., & Holz, D. E. (2002). Hydrostatic Expansion and Spin Changes during Type I X-Ray Bursts. *The Astrophysical Journal*, **564**, 343.

Deeter, J. E., Pravdo, S. H., & Boynton, P. E. (1981). Pulse-timing observations of Hercules X-1. *The Astrophysical Journal*, **247**, 1003.

di Matteo, T., Celotti, A., & Fabian, A. C. (1999). Magnetic flares in accretion disc coronae and the spectral states of black hole candidates: the case of GX 339–4. *Monthly Notices of the Royal Astronomical Society*, **304**, 809.

Ford, E. C., van der Klis, M., Méndez, M., Wijnands, R., Homan, J., Jonker, P. G., & van Paradijs, J. (2000). Simultaneous Measurements of X-Ray Luminosity and Kilohertz Quasi-Periodic Oscillations in Low-Mass X-Ray Binaries. *The Astrophysical Journal*, **537**, 368.

Fox, D. W. (2000). *X-ray Observations of Globular Clusters, Low-Mass X-ray Binaries, and a Supernova.* Ph.D. thesis, Massachusetts Institute of Technology.

Franco, L. M. (2001). The Effect of the Mass Accretion Rate on the Burst Oscillations in 4U 1728–34. *The Astrophysical Journal*, **554**, 340.

Frank, J., King, A., & Raine, D. (1995). *Accretion Power in Astrophysics.* Cambridge University Press.

Fryxell, B. A. & Woosley, S. E. (1982). Finite propagation time in multidimensional thermonuclear runaways. *The Astrophysical Journal*, **261**, 332.

Fujimoto, M. Y., Hanawa, T., & Miyaji, S. (1981). Shell flashes on accreting neutron stars and X-ray bursts. *The Astrophysical Journal*, **247**, 267.

Fujimoto, M. Y., Sztajno, M., Lewin, W. H. G., & van Paradijs, J. (1987). On the theory of type I X-ray bursts - The energetics of bursts and the nuclear fuel reservoir in the envelope. *The Astrophysical Journal*, **319**, 902.

Fushiki, I. & Lamb, D. Q. (1987). New insights from a global view of X-ray bursts. *The Astrophysical Journal*, **323**, L55.

Galloway, D. K., Chakrabarty, D., Muno, M. P., & Savov, P. (2001). Discovery of a 270 Hertz X-Ray Burst Oscillation in the X-Ray Dipper 4U 1916-053. *The Astrophysical Journal*, **549**, L85.

Garcia, M. R., McClintock, J. E., Narayan, R., Callanan, P., Barret, D., & Murray, S. S. (2001). New Evidence for Black Hole Event Horizons from Chandra. *The Astrophysical Journal*, **553**, L47.

Giles, A. B., Hill, K. M., Strohmayer, T. E., & Cummings, N. (2002). Burst Oscillation Periods from 4U 1636–53: A Constraint on the Binary Doppler Modulation. *The Astrophysical Journal*, **568**, 279.

Gottwald, M., Haberl, F., Parmar, A. N., & White, N. E. (1986). The bursting behavior of the transient X-ray burst source EXO 0748–676 - A dependence between the X-ray burst properties and the strength of the persistent emission. *The Astrophysical Journal*, **308**, 213.

Groth, E. J. (1975). Probability distributions related to power spectra. *The Astrophysical Journal Supplement*, **29**, 285.

Grove, J. E., Johnson, W. N., Kroeger, R. A., McNaron-Brown, K., Skibo, J. G., & Phlips, B. F. (1998). Gamma-Ray Spectral States of Galactic Black Hole Candidates. *The Astrophysical Journal*, **500**, 899.

Hanawa, T. & Fujimoto, M. Y. (1982). Irreducible Representation of Shell Flashes on Accreting Neutron Stars. *Publications of the Astronomical Society of Japan*, **34**, 495.

Hanawa, T. & Fujimoto, M. Y. (1984). Thermal response of neutron stars to shell flashes. *Publications of the Astronomical Society of Japan*, **36**, 199.

Heyl, J. S. (2002). Do Type-I Bursts Excite Modes in the Neutron-Star Ocean? *The Astrophysical Journal*, **submitted**, astro-ph/0108450.

in't Zand, J. J. M., Cornelisse, R., Kuulkers, E., Heise, J., Kuiper, L., Bazzano, A., Cocchi, M., Muller, J. M., Natalucci, L., Smith, M. J. S., & Ubertini, P. (2001). The first outburst of SAX J1808.4–3658 revisited. *Astronomy and Astrophysics*, **372**, 916.

Jahoda, K., Swank, J. H., Giles, A. B., Stark, M. J., Strohmayer, T., Zhang, W., & Morgan, E. H. (1996). In-orbit performance and calibration of the Rossi X-ray Timing Explorer (RXTE) Proportional Counter Array (PCA). In *Proc. SPIE Vol. 2808, p. 59-70, EUV, X-Ray, and Gamma-Ray Instrumentation for Astronomy VII. Oswald H. Siegmund & Mark A. Gummin, editors*, volume 2808, 59.

Joss, P. C. & Li, F. K. (1980). Helium-burning flashes on accreting neutron stars - Effects of stellar mass, radius, and magnetic field. *The Astrophysical Journal*, **238**, 287.

Kaaret, P., in 't Zand, J. M. M., Heise, J., & Tomsick, J. A. (2002). Discovery of Millisecond Variability in the Neutron Star X-ray Binary Transient SAX J1750.8−2900. *The Astrophysical Journal*, **accepted**, astro-ph/0204409.

Kuulkers, E., van der Klis, M., & van Paradijs, J. (1995). Burstlike Events in the Z Source Cygnus X-2. *The Astrophysical Journal*, **450**, 748.

Lampton, M., Margon, B., & Bowyer, S. (1976). Parameter estimation in X-ray astronomy. *The Astrophysical Journal*, **208**, 177.

Langmeier, A., Sztajno, M., Hasinger, G., Truemper, J., & Gottwald, M. (1987). EXOSAT observations of 4U 1705–44 - Type I bursts and persistent emission. *The Astrophysical Journal*, **323**, 288.

Lattimer, J. M. & Prakash, M. (2001). Neutron Star Structure and the Equation of State. *The Astrophysical Journal*, **550**, 426.

Leahy, D. A., Darbro, W., Elsner, R. F., Weisskopf, M. C., Kahn, S., Sutherland, P. G., & Grindlay, J. E. (1983). On searches for pulsed emission with application to four globular cluster X-ray sources - NGC 1851, 6441, 6624, and 6712. *The Astrophysical Journal*, **266**, 160.

Levine, A. M., Bradt, H., Cui, W., Jernigan, J. G., Morgan, E. H., Remillard, R., Shirey, R. E., & Smith, D. A. (1996). First Results from the All-Sky Monitor on the Rossi X-Ray Timing Explorer. *The Astrophysical Journal*, **469**, L33.

Lewin, W. H. G., van Paradijs, J., Cominsky, L., & Holzner, S. (1980). X-ray observations of 4U/MXB 1735–44. *Monthly Notices of the Royal Astronomical Society*, **193**, 15.

Lewin, W. H. G., Penninx, W., van Paradijs, J., Damen, E., Sztajno, M., Truemper, J., & van der Klis, M. (1987). EXOSAT observations of 4U/MXB 1636–53 - On the relation between the amount of accreted fuel and the strength of an X-ray burst. *The Astrophysical Journal*, **319**, 893.

Lewin, W. H. G., van Paradijs, J., & Taam, R. E. (1993). X-Ray Bursts. *Space Science Reviews*, **62**, 223.

Liu, Q. Z., van Paradijs, J., & van den Heuvel, E. P. J. (2001). A catalogue of low-mass X-ray binaries. *Astronomy and Astrophysics*, **368**, 1021.

London, R. A., Howard, W. M., & Taam, R. E. (1984). The spectra of X-ray bursting neutron stars. *The Astrophysical Journal*, **287**, L27.

London, R. A., Howard, W. M., & Taam, R. E. (1986). Model atmospheres for X-ray bursting neutron stars. *The Astrophysical Journal*, **306**, 170.

Madej, J. (1991). Model atmospheres and X-ray spectra of bursting neutron stars. *The Astrophysical Journal*, **376**, 161.

Makishima, K., Mitsuda, K., Inoue, H., Koyama, K., Matsuoka, M., Murakami, T., Oda, M., Ogawara, Y., Ohashi, T., Shibazaki, N., Tanaka, Y., Marshall, F., Hayakawa, S., Kunieda, H., Makino, F., Nagase, F., Tawara, Y., Miyamoto, S., Tsunemi, H., Tsuno, K., Yamashita, K., & Kondo, I. (1983). Discovery of X-ray bursts from GX 3+1 (4U 1744–26). *The Astrophysical Journal*, **267**, 310.

Makishima, K., Maejima, Y., Mitsuda, K., Bradt, H. V., Remillard, R. A., Tuohy, I. R., Hoshi, R., & Nakagawa, M. (1986). Simultaneous X-ray and optical observations of GX 339–4 in an X-ray high state. *The Astrophysical Journal*, **308**, 635.

Makishina, K., Inoue, H., Koyama, K., Matsuoka, M., Murakami, T., Oda, M., Ogawara, Y., Ohashi, T., Shibazaki, N., Tanaka, Y., Hayakawa, S., Kunieda, H., Makino, F., Masai, K., Nagase, F., Tawara, Y., Miyamoto, S., Tsunemi, H., Yamashita, K., & Kondo, I. (1982). Hakucho observations of X-ray bursts from 4U 1702–42. *The Astrophysical Journal*, **255**, L49.

Manchester, R. N. & Taylor, J. H. (1977). *Pulsars*. W. H. Freeman and Co., San Fransico, California.

Markoff, S., Falcke, H., & Fender, R. (2001). A jet model for the broadband spectrum of XTE J1118+480. Synchrotron emission from radio to X-rays in the Low/Hard spectral state. *Astronomy and Astrophysics*, **372**, L25.

Markwardt, C. B. & Swank, J. H. (2002). XTE J1751–305. *IAU Circular*, No. **7867**.

Markwardt, C. B., Strohmayer, T. E., & Swank, J. H. (1999). Observation of Kilohertz Quasi-periodic Oscillations from the Atoll Source 4U 1702–429 by the Rossi X-Ray Timing Explorer. *The Astrophysical Journal*, **512**, L125.

Miller, J. M., Fabian, A. C., Wijnands, R., Reynolds, C. S., Ehle, M., Freyberg, M. J., van der Klis, M., Lewin, W. H. G., Sanchez-Fernandez, C., & Castro-Tirado, A. J. (2002). Evidence for Spin and Energy Extraction in a Galactic Black Hole Candidate: The XMM-Newton/EPIC-PN Sprectum of XTE J1650–500. *The Astrophysical Journal*, **submitted**, astro-ph/0202375.

Miller, M. C. (1999). Evidence for Antipodal Hot Spots During X-Ray Bursts from 4U 1636–536. *The Astrophysical Journal*, **515**, L77.

Miller, M. C. (2000). A Characterization of the Brightness Oscillations during Thermonuclear Bursts from 4U 1636–536. *The Astrophysical Journal*, **531**, 458.

Miller, M. C. & Lamb, F. K. (1998). Bounds on the Compactness of Neutron Stars from Brightness Oscillations during X-Ray Bursts. *The Astrophysical Journal*, **499**, L37.

Miller, M. C., Lamb, F. K., & Psaltis, D. (1998). Sonic-Point Model of Kilohertz Quasi-periodic Brightness Oscillations in Low-Mass X-Ray Binaries. *The Astrophysical Journal*, **508**, 791.

Mirabel, I. F. & Rodríguez, L. F. (1999). Sources of Relativistic Jets in the Galaxy. *Annual Reviews of Astronomy and Astrophysics*, **37**, 409.

Muno, M. P., Fox, D. W., Morgan, E. H., & Bildsten, L. (2000). Nearly Coherent Oscillations in Type I X-Ray Bursts from KS 1731–260. *The Astrophysical Journal*, **542**, 1016.

Muno, M. P., Remillard, R. A., & Chakrabarty, D. (2002). How Do Z and Atoll X-Ray Binaries Differ? *The Astrophysical Journal*, **568**, L35.

Murakami, T., Inoue, H., Koyama, K., Makishima, K., Matsuoka, M., Oda, M., Ogawara, Y., Ohashi, T., Shibazaki, N., Tanaka, Y., Tawara, Y., Hayakawa, S., Kunieda, H., Makino, F., Masai, K., Nagase, F., Miyamoto, S., Tsunemi, H., Yamashita, K., & Kondo, I. (1980). Properties of X-ray bursts from the X-ray transient 1608–522. *The Astrophysical Journal*, **240**, L143.

Nath, N. R., Strohmayer, T. E., & Swank, J. H. (2002). Bounds on Compactness for Low-Mass X-Ray Binary Neutron Stars from X-Ray Burst Oscillations. *The Astrophysical Journal*, **564**, 353.

Orosz, J. A., Bailyn, C. D., Remillard, R. A., McClintock, J. E., & Foltz, C. B. (1994). Quiescent accretion disks in black hole X-ray novae. *The Astrophysical Journal*, **436**, 848.

Orosz, J. A., Groot, P. J., van der Klis, M., McClintock, J. E., Garcia, M. R., Zhao, P., Jain, R. K., Bailyn, C. D., & Remillard, R. A. (2002). Dynamical Evidence for a Black Hole in the Microquasar XTE J1550–564. *The Astrophysical Journal*, **568**, 845.

Osherovich, V. & Titarchuk, L. (1999). Kilohertz Quasi-periodic Oscillations in Neutron Star Binaries Modeled as Keplerian Oscillations in a Rotating Frame of Reference. *The Astrophysical Journal*, **522**, L113.

Özel, F. (2002). Timing Properties of Magnetars. *The Astrophysical Journal*, **submitted**, astro-ph/0201158.

Pechenick, K. R., Ftaclas, C., & Cohen, J. M. (1983). Hot spots on neutron stars — The near-field gravitational lens. *The Astrophysical Journal*, **274**, 846.

Predehl, P. & Schmitt, J. H. M. M. (1995). X-raying the interstellar medium: ROSAT observations of dust scattering halos. *Astronomy and Astrophysics*, **293**, 889.

Press, W. H., Teukolsky, S. A., Vetterling, W. T., & Flannery, B. P. (1992). *Numerical Recipes in C*. Cambridge University Press.

Price, R. H. (1982). General Relativity Primer. *American Journal of Physics*, **50**, 300.

Psaltis, D. (2001). Models of quasi-periodic variability in neutron stars and black holes. *Advances in Space Research*, **28**, 481.

Rothschild, R. E., Blanco, P. R., Gruber, D. E., Heindl, W. A., MacDonald, D. R., Marsden, D. C., Pelling, M. R., Wayne, L. R., & Hink, P. L. (1998). In-Flight Performance of the High-Energy X-Ray Timing Experiment on the Rossi X-Ray Timing Explorer. *The Astrophysical Journal*, **496**, 538.

Schoelkopf, R. J. & Kelley, R. L. (1991). Detection of coherent 7.6 HZ oscillations during a burst from Aquila X-1. *The Astrophysical Journal*, **375**, 696.

Shapiro, S. L., Lightman, A. P., & Eardley, D. M. (1976). A two-temperature accretion disk model for Cygnus X-1 — Structure and spectrum. *The Astrophysical Journal*, **204**, 187.

Smale, A. P. & Mukai, K. (1988). The orbital variability of XB1636-536. *Monthly Notices of the Royal Astronomical Society*, **231**, 663–671.

Smith, D. A., Morgan, E. H., & Bradt, H. (1997). Rossi X-Ray Timing Explorer Discovery of Coherent Millisecond Pulsations during an X-Ray Burst from KS 1731–260. *The Astrophysical Journal*, **479**, L137.

Spitkovsky, A., Levin, Y., & Ushomirsky, G. (2002). Propagation of Thermonuclear Flames on Rapidly Rotating Neutron Stars: Extreme Weather during Type I X-Ray Bursts. *The Astrophysical Journal*, **566**, 1018.

Standish, E. M., Newhall, X. X., Williams, J. G., & Yeomans, D. K. (1992). The jet propulsion laboratory de-200 solar system ephemeris. In *Explanatory Supplement to the Astronomical Almanac*, Seidelmann, P. K., editor, Mill Valley: University Science, 279.

Stella, L. & Vietri, M. (1999). kHz Quasiperiodic Oscillations in Low-Mass X-Ray Binaries as Probes of General Relativity in the Strong-Field Regime. *Physical Review Letters*, **82**, 17.

Strohmayer, T. E. (1999). Spin-down of Pulsations in the Cooling Tail of an X-Ray Burst from 4U 1636–53. *The Astrophysical Journal*, **523**, L51.

Strohmayer, T. E. (2001). Oscillations during thermonuclear x-ray bursts. *Advances in Space Research*, **28**, 511.

Strohmayer, T. E. & Markwardt, C. B. (1999). On the Frequency Evolution of X-Ray Brightness Oscillations during Thermonuclear X-Ray Bursts: Evidence of Coherent Oscillations. *The Astrophysical Journal*, **516**, L81.

Strohmayer, T. E. & Markwardt, C. B. (2002). Evidence for a Millisecond Pulsar in 4U 1636–53 During a Superburst. *The Astrophysical Journal*, **submitted**.

Strohmayer, T. E., Zhang, W., Swank, J. H., Smale, A., Titarchuk, L., Day, C., & Lee, U. (1996). Millisecond X-Ray Variability from an Accreting Neutron Star System. *The Astrophysical Journal*, **469**, L9.

Strohmayer, T. E., Zhang, W., & Swank, J. H. (1997a). 363 Hz Oscillations during the Rising Phase of Bursts from 4U 1728–34: Evidence for Rotational Modulation. *The Astrophysical Journal*, **487**, L77.

Strohmayer, T. E., Jahoda, K., Giles, A. B., & Lee, U. (1997b). Millisecond Pulsations from a Low-Mass X-Ray Binary in the Galactic Center Region. *The Astrophysical Journal*, **486**, 355.

Strohmayer, T. E., Zhang, W., Swank, J. H., & Lapidus, I. (1998). The Long-Term Stability of Oscillations during Thermonuclear X-Ray Bursts: Constraining the Binary X-Ray Mass Function. *The Astrophysical Journal*, **503**, L147.

Sztajno, M., Basinska, E. M., Cominsky, L. R., Marshall, F. J., & Lewin, W. H. G. (1983). X-ray burst observations of Serpens X-1. *The Astrophysical Journal*, **267**, 713.

Sztajno, M., van Paradijs, J., Lewin, W. H. G., Trumper, J., Stollman, G., Pietsch, W., & van der Klis, M. (1985). Unusual X-ray burst profiles from 4U/MXB 1636–53. *The Astrophysical Journal*, **299**, 487.

Sztajno, M., van Paradijs, J., Lewin, W. H. G., Langmeier, A., Trumper, J., & Pietsch, W. (1986). X-ray bursts from GX 17+2 — A new approach. *Monthly Notices of the Royal Astronomical Society*, **222**, 499.

van der Klis, M. (1995). Rapid aperiodic variability in x-ray binaries. In *X-ray Binaries*, Lewin, W. H. G. and van Paradijs, J. and van den Heuvel, E. P. J., editors. Cambridge University Press, 252.

van der Klis, M. (2000). Millisecond Oscillations in X-ray Binaries. *Annual Reviews of Astronomy and Astrophysics*, **38**, 717.

van der Klis, M., Hasinger, G., Damen, E., Penninx, W., van Paradijs, J., & Lewin, W. H. G. (1990). Correlation of X-ray burst properties with source state in the 'atoll' source 4U/MXB 1636–53. *The Astrophysical Journal*, **360**, L19.

van der Klis, M., Wijnands, R. A. D., Horne, K., & Chen, W. (1997). Kilohertz Quasi-Periodic Oscillation Peak Separation Is Not Constant in Scorpius X-1. *The Astrophysical Journal*, **481**, L97.

van Paradijs, J., Penninx, W., & Lewin, W. H. G. (1988a). On the relation between X-ray burst properties and the persistent X-ray luminosity. *Monthly Notices of the Royal Astronomical Society*, **233**, 437.

van Paradijs, J., Penninx, W., Lewin, W. H. G., Sztajno, M., & Truemper, J. (1988b). The recurrence behaviour of X-ray bursts from 4U/MXB 1735–44. *Astronomy and Astrophysics*, **192**, 147.

van Straaten, S., van der Klis, M., Kuulkers, E., & Méndez, M. (2001). An Atlas of Burst Oscillations and Spectral Properties in 4U 1728–34. *The Astrophysical Journal*, **551**, 907.

Vaughan, B. A., van der Klis, M., Wood, K. S., Norris, J. P., Hertz, P., Michelson, P. F., van Paradijs, J., Lewin, W. H. G., Mitsuda, K., & Penninx, W. (1994). Searches for millisecond pulsations in low-mass X-ray binaries, 2. *The Astrophysical Journal*, **435**, 362.

Wachter, S., Smale, A. P., & Bailyn, C. (2000). The Reappearance of the Transient Low-Mass X-Ray Binary X1658–298. *The Astrophysical Journal*, **534**, 367.

Walter, F. M., Mason, K. O., Clarke, J. T., Halpern, J., Grindlay, J. E., Bowyer, S., & Henry, J. P. (1982). Discovery of a 50 minute binary period and a likely 22 magnitude optical counterpart for the X-ray burster 4U 1915–05. *The Astrophysical Journal*, **253**, L67.

Weinberg, N., Miller, M. C., & Lamb, D. Q. (2001). Oscillation Waveforms and Amplitudes from Hot Spots on Neutron Stars. *The Astrophysical Journal*, **546**, 1098.

Welsh, W. F., Robinson, E. L., & Young, P. (2000). The Orbital Light Curve of Aquila X-1. *The Astronomical Journal*, **120**, 943.

White, N. E. & Zhang, W. (1997). Millisecond X-Ray Pulsars in Low-mass X-Ray Binaries. *The Astrophysical Journal*, **490**, L87.

White, N. E., Nagase, F., & Parmar, A. N. (1995). The properties of x-ray binaries. In *X-ray Binaries*, Lewin, W. H. G. and van Paradijs, J. and van den Heuvel, E. P. J., editors. Cambridge University Press, 1.

Wijnands, R. & van der Klis, M. (1998). A millisecond pulsar in an X-ray binary system. *Nature*, **394**, 344.

Wijnands, R., Strohmayer, T., & Franco, L. . (2001). Discovery of Nearly Coherent Oscillations with a Frequency of 567 Hz during Type I X-Ray Bursts of the X-Ray Transient and Eclipsing Binary X1658–298. *The Astrophysical Journal*, **549**, L71.

Wijnands, R. A. D. & van der Klis, M. (1997). Discovery of Two Simultaneous Kilohertz Quasi-periodic Oscillations in KS 1731–260. *The Astrophysical Journal*, **482**, L65.

Zhang, W., Lapidus, I., Swank, J. H., White, N. E., & Titarchuk, L. (1997). U 1636-53. *IAU Circular*, No. **6541**.

Zhang, W., Jahoda, K., Kelley, R. L., Strohmayer, T. E., Swank, J. H., & Zhang, S. N. (1998). Millisecond Oscillations in the Persistent and Bursting Flux of Aquila X-1 during an Outburst. *The Astrophysical Journal*, **495**, L9.